RADC-TR-85-166
Final Technical Report
September 1985

ASCOT (ADVANCED STRUCTURAL CONTROL TECHNIQUES)

Control Dynamics Company

Sponsored by
Defense Advanced Research Projects Agency (DOD)
ARPA Order No. 4828

APPROVED FOR PUBLIC RELEASE; DISTRIBUTION UNLIMITED

ROME AIR DEVELOPMENT CENTER
Air Force Systems Command
Griffiss Air Force Base, NY 13441-5700

This report has been reviewed by the RADC Public Affairs Office (PA) and is releasable to the National Technical Information Service (NTIS). At NTIS it will be releasable to the general public, including foreign nations.

RADC-TR-85-166 has been reviewed and is approved for publication.

APPROVED: Richard W. Carman

RICHARD W. CARMAN
Project Engineer

APPROVED: Frank J. Rehm

FRANK J. REHM
Technical Director
Surveillance Division

FOR THE COMMANDER: John A. Ritz

JOHN A. RITZ
Plans Office

If your address has changed or if you wish to be removed from the RADC mailing list, or if the addressee is no longer employed by your organization, please notify RADC (OCSP) Griffiss AFB NY 13441-5700. This will assist us in maintaining a current mailing list.

Do not return copies of this report unless contractual obligations or notices on a specific document requires that it be returned.

ASCOT (ADVANCED STRUCTURAL CONTROL TECHNIQUES)

Sherman M. Seltzer
D.K. Tollison
T.G. Hansman
R.D. Irwin
W.P. Maggard

Contractor: General Dynamics Company
Contract Number: F30602-84-C-0012
Effective Date of Contract: 23 November 1983
Contract Expiration Date: 23 November 1984
Short Title of Work: Advanced Structural Control Techniques (ASCOT)
Program Code Number: 3E20, 4E20
Period of Work Covered: Nov 83 - Jan 85

Principal Investigator: Dr. Sherman Seltzer
Phone: (205) 837-8510

Project Engineer: Richard W. Carman
Phone: (315) 330-4481

This research was supported by the Defense Advanced Research Projects Agency of the Department of Defense and was monitored by Richard W. Carman (OCSP) Griffiss AFB NY 13441-5700, under Contract F30602-84-C-0012.

ADA 165917

UNCLASSIFIED
SECURITY CLASSIFICATION OF THIS PAGE

REPORT DOCUMENTATION PAGE

1a. REPORT SECURITY CLASSIFICATION UNCLASSIFIED	1b. RESTRICTIVE MARKINGS N/A
2a. SECURITY CLASSIFICATION AUTHORITY N/A	3. DISTRIBUTION / AVAILABILITY OF REPORT Approved for public release; distribution unlimited
2b. DECLASSIFICATION / DOWNGRADING SCHEDULE N/A	
4. PERFORMING ORGANIZATION REPORT NUMBER(S) 223-1284-FR-ASC	5. MONITORING ORGANIZATION REPORT NUMBER(S) RADC-TR-85-166
6a. NAME OF PERFORMING ORGANIZATION Control Dynamics Company 6b. OFFICE SYMBOL (If applicable)	7a. NAME OF MONITORING ORGANIZATION Rome Air Development Center (OCSP)
6c. ADDRESS (City, State, and ZIP Code) 555 Sparkman Drive, Suite 1414 Huntsville AL 35805	7b. ADDRESS (City, State, and ZIP Code) Griffiss AFB NY 13441-5700
8a. NAME OF FUNDING / SPONSORING ORGANIZATION Defense Advanced Research Projects Agency 8b. OFFICE SYMBOL (If applicable) STO	9. PROCUREMENT INSTRUMENT IDENTIFICATION NUMBER F30602-84-C-0012
8c. ADDRESS (City, State, and ZIP Code) 1400 Wilson Blvd Arlington VA 22209	10. SOURCE OF FUNDING NUMBERS PROGRAM ELEMENT NO. 62301E; PROJECT NO. D828; TASK NO. 01; WORK UNIT ACCESSION NO. 01
11. TITLE (Include Security Classification) ASCOT (ADVANCED STRUCTURAL CONTROL TECHNIQUES)	
12. PERSONAL AUTHOR(S) Sherman M. Seltzer, D.K. Tollison, T.G. Hovsman, R.D. Irwin, W.P Maggard	
13a. TYPE OF REPORT Final 13b. TIME COVERED FROM Nov 83 TO Jan 85	14. DATE OF REPORT (Year, Month, Day) September 1985 15. PAGE COUNT
16. SUPPLEMENTARY NOTATION N/A	

17 COSATI CODES			18. SUBJECT TERMS (Continue on reverse if necessary and identify by block number)	
FIELD	GROUP	SUB-GROUP		
17	08	05	Multivariable Control	Sampled Data
22	02	05	Digital Control	Prefilter
			Large Space Structure	Random Sampling

19. ABSTRACT (Continue on reverse if necessary and identify by block number)

This is the Control Dynamics Company final technical report on Advanced Structural Control Techniques (ASCOT). Included is the description and application of a novel technique for the design of low order digital controllers for very high order system models. Also included is an investigation of a digital prefiltering technique which incorporates non-uniform rate sampling.

20. DISTRIBUTION / AVAILABILITY OF ABSTRACT ☒ UNCLASSIFIED/UNLIMITED ☐ SAME AS RPT ☐ DTIC USERS	21. ABSTRACT SECURITY CLASSIFICATION UNCLASSIFIED
22a. NAME OF RESPONSIBLE INDIVIDUAL Richard W. Carman	22b. TELEPHONE (Include Area Code) (315) 330-4481 22c. OFFICE SYMBOL RADC (OCSP)

DD FORM 1473, 84 MAR 83 APR edition may be used until exhausted
All other editions are obsolete

SECURITY CLASSIFICATION OF THIS PAGE
UNCLASSIFIED

ACKNOWLEDGEMENT

The work reported upon in this report was performed by the Control Dynamics Company in Huntsville, Alabama under Contract No. F30602-84-C-0012. It was supported by the Defense Advanced Research Projects Agency (DARPA) and monitored by Rome Air Development Center (RADC). The RADC Project Engineer was Mr. Richard Carman.

The Principal Investigator was Dr. Sherman M. Seltzer, and the Co-Investigator was Dr. H. Eugene Worley. Primary contributors to the accomplishment of the work and the preparation of this report were:

Mr. Danny K. Tollison
Mr. Thomas G. Howsman
Mr. Richard D. Irwin
Mr. William P. Maggard
Ms. Anna E. Banks
Mr. John R. Piner.

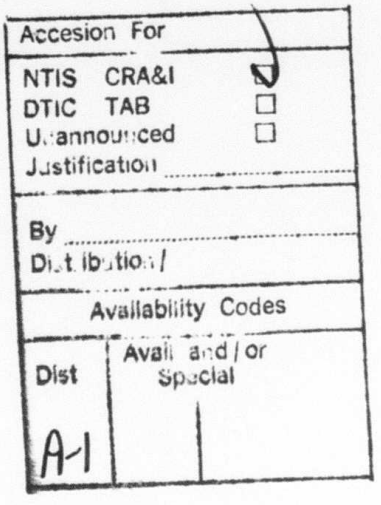

TABLE OF CONTENTS

LIST OF FIGURES

LIST OF TABLES

1. INTRODUCTION

The following paragraphs provide background information and objectives for the ASCOT effort as delineated in the Statement of Work (SOW). Also included is a brief description of the contents of the body of the report.

1.1 BACKGROUND

Several spaceborne optical surveillance and weapon system concepts of interest to USAF and DARPA require precision Line-of-Sight (LOS) and figure control in order to achieve their missions. To date, three major system concepts have been identified: High Altitude Large Optics (HALO), Multi Mission Beam Control System (MMBCS), and Large Optics Demon stration (LODE). Each of these system has common features in terms of large size, extreme complexity, low mass, low stiffness and precision structural tolerances. Each concept is also required to maintain stringent LOS and figure stability despite strong environmental and onboard disturbances. The vibration disturbance isolation, damping, and control technology required to achieve the desired performance is beyond the state-of-the-art practiced today.

This motivates the development and demonstration of new control techniques which have broad application to future large flexible military space structures. Control system design techniques to date have assumed comprehensive and complex computer implementations. Recognizing the ultimate implementation of these techniques in onboard space-qualified digital computers provides important practical reasons for their simplification.

The development and demonstration of such broadly applicable, yet simplified and practical, techniques is the goal of Advanced Structural Control Techniques (ASCOT).

1.2 OBJECTIVES

The objective of this effort is, in general, the development, evaluation, and preparation for testing and implementation of Advanced Structural Control Techniques (ASCOT) that are applicable to future large flexible military spacecraft. The two particular objectives are: (1) the development and integration of a Simplified Systematic Digital Design (S2D2) which meets anticipated structural and attitude control system performance requirements, and (2) the development of an ASCOT Technical/Management Program Development Plan and selection, evaluation, and comparison of candidate control system design techniques including S2D2.

1.3 DESCRIPTION OF REPORT BODY

Pursuant to the first objective stated above, Task 1 includes those activities related to digital design technique development and is reported on in Section 2.1. Section 2.2 concerns Task 2 - test planning and coordination, test support and control technique selection - and answers the objective set forth in Section 1.2.2. Because the tasks and subtasks were conceived based upon these objectives rather than the input/output relationship between tasks, at certain points in the text the reader will be referred to later report sections for additional information.

Section 2.1.1 specifies a set of intrinsic performance goals for the S2D2 controller and design technique in the form of a list of desired qualities. Section 2.1.2 then specifies three typical disturbances to be applied in evaluating the performance of S2D2.

Synthesis of the candidate S2D2 controller is delineated in Section 2.1.3 and is followed by application of the candidate technique to the ASCOT-I structural model described in Section 2.2.2.

Attention is then turned to the design of prefilters (both analog and digital) in Section 2.1.5. Aliasing and the use of prefilters are discussed in general, and the non-uniform sampling period digital prefilter is pursued particularly. Both theoretical background and simulation results for the digital and analog prefilters are provided.

Section 2.1.6 provides post analysis studies of the system designed under Section 2.1.4 in both the frequency and time domains. Performance is evaluated with respect to the evaluation criteria discussed in Section 2.2.3.

A study of which spacecraft parameters are likely to affect the controller performance is given in 2.1.7 with the result being a "perturbed" version of the "RTOP" model procured under 2.2.5 which is used in the robustness studies of Section 2.1.8. These studies are conducted using the digital controller described in Section 2.2.5 along with the perturbed model.

Description of the Task 2 effort gets underway with a brief account of the development of the Technical/Management Program Development Plan which was delivered midway of the contract period as a stand-alone document.

The content of Sections 2.2.2 and 2.2.3 has been discussed in the preceding paragraphs. Section 2.2.4 includes a discussion of three LSS control system design technique candidates other than S2D2.

Finally, Section 2.2.5 covers the application of the S2D2 candidate to the RTOP model which is a more advanced structure than the ASCOT-I model.

2. TECHNICAL ACTIVITIES

2.1 TASK 1 - DIGITAL DESIGN TECHNIQUE DEVELOPMENT

2.1.1 Specification of Performance Goals

The following areas of importance have been identified for practical design techniques applicable to large flexible military spacecraft. These are the goals of the S2D2 technique.

- Simplicity of Controller

A digital controller design technique for LSS must lead to controllers of reasonable order despite the large order system models which are likely to be used in the design of controllers for flexible spacecraft. This is to minimize the computational burden of the onboard computer when the controller is implemented. This also facilitates simpler checkout procedures for flight qualification of control software.

- Straightforward and Traceable Design Procedure

The S2D2 design technique should be readily understandable and the design process should trace effects of closed loop control upon the system behavior throughout the design process. In this way a designer can see how the system is evolving during the design process, and therefore have insight into problems and/or causes of problems should they arise.

- Stability of Closed Loop System

The S2D2 technique should inherently provide stability of the closed loop system resulting from the combination of the digital controller and the LSS model. In fact, a reasonable amount of relative stability should be inherent.

- Inherent Robustness Checks

Robustness is of particular concern to the LSS control system designer because accurate models are not anticipated. Hence, the S2D2 technique should produce designs with reasonable robustness with respect to model inaccuracies and plant variation. In addition, the design technique should provide built-in checks for robustness at stages in the design process. This is also a part of an easily traceable design procedure.

- Disturbance Rejection

Disturbance rejection is a major concern in control system design for LSS and should inherently be achieved through the design process.

- Digital Design Accomplished in Digital Domain

Design of digital control systems should be accomplished in the digital domain so that the effects of sampling and computational transport lags can be accounted for during the design phase. This is in lieu of designing a continuous controller and then attempting to implement a digital equivalent which, at best, is an approximation to the desired controller.

- Efficiency of Design

The design technique should be reasonably efficient with respect to computer processing and storage requirements and should be algorithmic in nature so that the design process can be easily repeated as model updates are obtained.

2.1.2 Specification of Disturbances

In order to evaluate the noise rejection performance of the S2D2 candidate as applied to the ASCOT-I and RTOP structural models, suitable disturbance signals must be identified. Of the three distrubance input signals

applied in these studies, one is a broadband random disturbance and two are deterministic in nature.

The broadband random disturbance is represented by its Power Spectral Density (PSD) as shown in Fig. 1, and is similar to that developed by Riverside Research Institute under the ACOSS program. The random disturbance represents equipment noise that would be expected on a "free-flyer" satellite, i.e., vibrations of rotating machinery and fluid flow. It is, of course, scaled down in magnitude somewhat from that of the ACOSS application because of the considerably less massive spacecraft model to which it is applied.

The two deterministic disturbance inputs shown in Figs. 2 and 3 are representative of shuttle orbiter type disturbances. Fig. 2 represents astronaut push-off within the shuttle orbiter and Fig. 3 represents Reaction Control System (RCS) thruster firing.

2.1.3 Synthesis of Candidate Primary Digital Controller

The candidate S2D2 technique presented herein is that of "1CAT," (One Controller At a Time). The following sections delineate the theoretical background of 1CAT and a particular numerical implementation of 1CAT.

Theoretical Background of 1CAT. 1CAT is a multi-input/multioutput (MIMO) digital controller design technique which finds its basis in the fundamental principles of classical analysis and design control theory. It springs from the fact that the combination of a MIMO system, such as a LSS, and its controller can be viewed as a coupled multiloop system. The controllers for the loops cannot be designed independently, but they can be designed one at a time. This is the thesis of 1CAT: "One Controller At a Time."

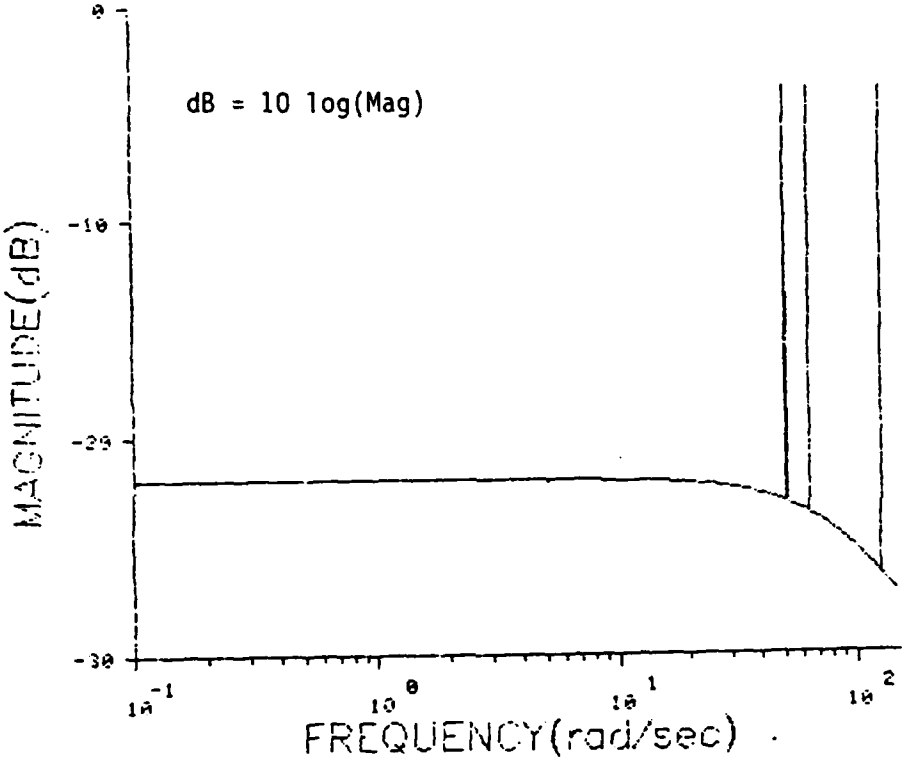

Figure 1. PSD of Broadband Random Disturbance Input.

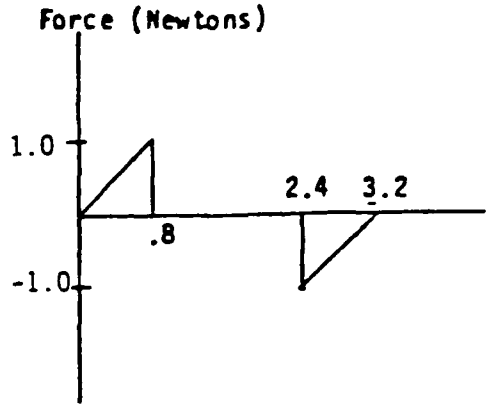

Figure 2. Astronaut Push-off Disturbance Input.

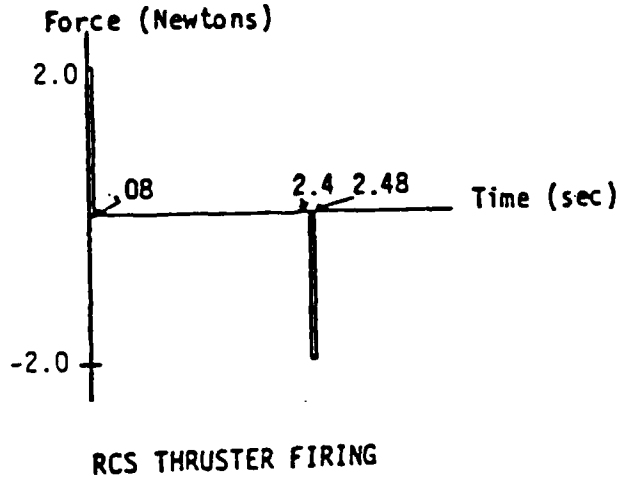

Figure 3. RCS Thruster Firing Disturbance Input.

To delineate the process, consider a system having three inputs and three outputs. With all possible feedback paths open, the transfer characteristic between a particular input-output pair may be examined and a controller designed to stabilize the loop to satisfactory specifications. With this loop closed, another input-output pair may be examined and a controller likewise designed. The second controller is not designed independently, because the effects of the first controller are taken into account when the first loop is closed. A third controller may then be designed with the first two loops closed, and so on until all desired feedback paths are closed through their appropriate controllers. A designer would probably not choose to close all nine possible feedback paths of this system; however, the ICAT technique does not preclude this possibility.

Three pertinent facts regarding the ICAT technique and its applicability bear mention at this point.

- *If the plant is stabilizable, the resulting closed loop system will* be stable.

Stabilizability simply implies that if there are uncontrollable and/or unobservable modes, i.e., modes whose eigenvalues cannot be changed by feedback, their eigenvalues must have negative real parts. In this case the uncontrollable modes cannot result in instability, but the controllable modes can. However, the ICAT approach can be applied so that no controllable mode can cause a stability problem and, in fact, can produce a design that will ensure a specified amount of relative stability.

For example, suppose that the ICAT approach is applied to a three-loop example. With all loops open, assume that a controller is designed for the first loop so that all controllable modes have closed loop eigenvalues with

real parts less than $-\alpha$. Now with the first loop closed, a controller is designed for the second loop so that all controllable modes have closed loop eigenvalues with real parts less than $-\alpha$. Then with the first two loops closed, a controller is designed for the third loop so that all controllable modes have closed loop eigenvalues with real parts less than $-\alpha$. Now suppose a root locus study is performed on the first loop with the second and third loops closed and with the controllers designed for each loop included. The controllable modes in this loop can be separated into two categories: (1) those modes controllable only from loop one and (2) those modes controllable from loops two and/or three. Using the gain factor for which loop one was designed, those modes controllable only from loop one must have eigenvalues with real parts less than $-\alpha$., since these modes are not affected by the designs in loop two and/or three, and loop one was designed to achieve this specification. The other controllable modes in loop one must have eigenvalues with real parts less than $-\alpha$ since these eigenvalues are controllable from loop two and/or three, which were also designed to meet this specification.

The bottom line is that, as subsequent loop closures are made, eigenvalues of preceding loops cannot have real parts greater than $-\alpha$. However, note that if a subsequent loop is designed with a more relaxed specification, the relative stability of the preceding loops can relax as well.

Although the above arguments have been made for the first loop of a three-loop example, they obviously can be extended to the design of a system with many loops and to loops other than the first. In addition, other measurements of relative stability can be used, e.g., gain margins and phase margins. In order to ensure no degradation in the relative stability of

loops previously closed, subsequent loops should be designed so that relative stability is improved or, as a minimum, not allowed to degrade.

- Each controller in each loop can be designed by classical techniques.

Because of the "one at a time" nature of 1CAT, classical design techniques, such as frequency response, root locus, or parameter space techniques, can be used to design individual control loops. This also makes possible the use of many tried and tested stability criteria, e.g., gain margins, phase margins, maximum damping of any mode, etc. In addition, analysis and design tools already well developed are not made obsolete by 1CAT but, to the contrary, are given a new arena in which to work.

- The effects of closure of other loops upon a particular loop are obvious by comparing the design criteria before and after the closures.

This intermediate analysis of the partially designed system gives the designer insight into the controller design problem at steps throughout the design process. Particular problem areas may be detected before the design is complete and, therefore, attacked at their source. More importantly, the designer is in a better position to discover what characteristics of his design (or the plant to be controlled) are causing stability and/or performance problems than if he uses a one-step design algorithm.

Numerical Implementation of 1CAT for Digital Controller Design Using Frequency Domain Techniques. As previously mentioned, various design techniques are available for accomplishing a 1CAT design of MIMO systems. In this section the numerical implementation of 1CAT for performing digital controller designs using frequency domain techniques is delineated. The choice

of digital control is made based on the needed flexibility and expected hardware on systems for which S2D2 is targeted.

The choice of frequency response techniques is based primarily on obtaining numerical efficiency and avoiding numerical problems. In particular the MIMO systems for which the ICAT approach is applicable are very high order; thus, if root locus or parameter space techniques are selected, it will be necessary to determine z-transforms of high order systems and, consequently, be posed with numerically determining poles and zeros of z-transfer functions. With sample rates as expected for such applications, most of these poles and zeros will lie in close proximity to z = 1 in the z-plane. This poses a significant problem in the numerical determination of these poles and zeros, since their locations will be very sensitive to coefficient roundoff in their respective z-transfer functions. However, by selection of a frequency domain approach the tedious and numerically troublesome z-transform process can be completely avoided as shown later.

Another need in the numerical implementation of the ICAT approach for designing MIMO systems is a straightforward technique for the opening and closing of loops and the inclusion of controllers as the design process proceeds. This is accomplished by modeling the MIMO system with vector - matrix block diagrams. In particular signals are concatenated to form vectors of signals and transfer functions are concatenated to form transfer function matrices.

The vector matrix model eases the notational problems associated with the handling of MIMO systems in the frequency domain. A transfer function matrix, [T(s)], is defined to have elements, $T_{ij}(s)$, such that $T_{ij}(s)$ is

the transfer function or frequency response from the jth input to the ith output of the MIMO system described by

$$C(s) = [T(s)]\, R(s) \qquad (2.1.3\text{-}1)$$

where R(s) and C(s) are, respectively, the Laplace Transforms or frequency spectrums of the input and output signal vectors.

Using this notation, a block diagram of a MIMO system utilizing feedback and digital control is shown in Fig. 4 where the following definitions apply:

n		number of modes used in the design analysis
m		number of inputs and outputs of the MIMO system under study
R(z)	m x 1	digital input vector
C(s)	m x 1	continuous output vector
C*(s)	m x 1	sampled-data output vector
$[D_1(z)]$	m x m	digital feedback controller transfer function matrix
$[D_2(z)]$	m x m	digital forward path controller transfer function matrix
I_m	m x m	identity matrix
$G_{h0}(s)$	scalar	zero order hold device $(1 - e^{-sT})/s$
T	scalar	sampling period
[K]	n x m	actuator modal gain matrix
$[G_m(s)]$	n x n	diagonal modal transfer function matrix
[L]	n x m	sensor modal gain matrix.

This block diagram has been customized to the LSS design problem by the use of the matrices, [L], [K], and $[G_m(s)]$ to describe the plant, rather than a single m x m matrix, [T(s)]. Use of the factored form allows the modal gains to be changed easily and efficiently without recomputation of the modal frequency responses in $[G_m(s)]$ (exercise of (2.1.3-3) below). Another assumption of this implementation is that of an equal number of inputs and outputs. This is not required by the ICAT technique, and neither does it restrict the implementation, because "dummy" inputs and outputs may be specified as required at little cost with regard to efficiency. In addition,

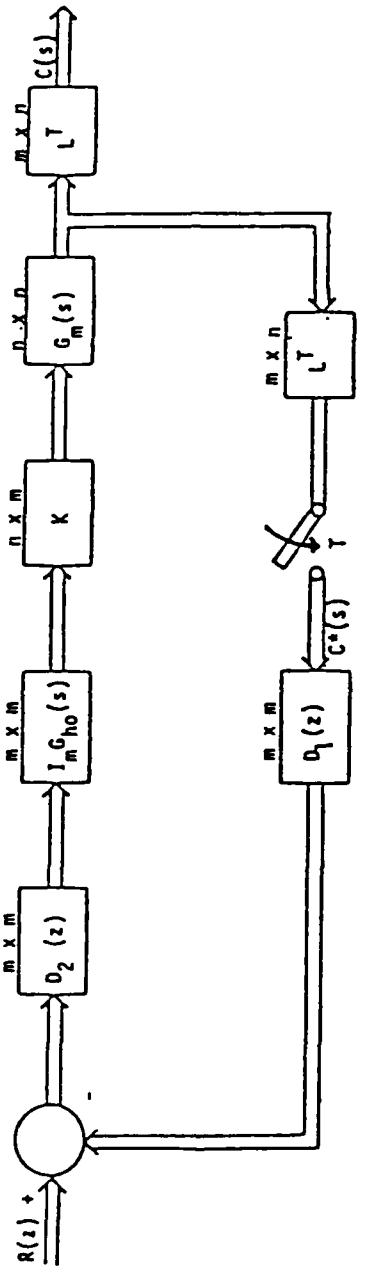

Figure 4. 1 CAT Implementation Block Diagram.

this implementation is geared toward digital control; however, a continuous control version may be generated in a similar manner.

The first step in the ICAT design process is the casting of the control system into the form represented by the diagram of Fig. 4. Virtually any MIMO control system can readily be cast into this form by determining what the system inputs and outputs will be and defining the transfer characteristics between them. For the LSS problem, using a modal analysis model and ideal sensors and actuators, $[G_m(s)]$ is diagonal, and the modal actuator and sensor gains are placed in [K] and [L], respectively. In the case of sensor and actuator dynamics, the actuator and sensor transfer functions may be placed in [K] and [L] so that no generality is lost. It is easily seen that in the case where [K] and [L] are mth order identity matrices and $[G_m(s)]$ is m x m and not necessarily diagonal, this implementation becomes the general one where $[G_m(s)] = [T(s)]$.

The sampled-data output vector of the vector-matrix block diagram of Fig. 4 is

$$\underline{C}^*(s) = [I_m + (L^T G_m(s) K G_{ho}(s))^* D_2(z) D_1(z)]^{-1} [(L^T G_M(s) K G_{ho}(s))^* D_2(z) \underline{R}(z)] \qquad (2.1.3\text{-}2)$$

where the symbol, "*", indicates a sampled-data quantity, often called a starred quantity. It should be noted that a "*" of a matrix is a matrix in which each element is "*"'ed. Equation (1-2) is computed at discrete frequency points over the range of interest of the analysis, with each of the transfer functions represented by its frequency response data (real and imaginary parts vs. frequency).

In evaluating the frequency responses of Equation (2.1.3-2), two types of frequency responses must be generated - those of starred transfer functions

and those of z-transfer functions. The starred frequency responses can be obtained by taking the z-transform of the quantities operated upon by the starring operation and evaluating at $z = e^{j\omega T}$ or more easily from the following infinite series:

$$G^*(j\omega) = \frac{1}{T}\sum_{n=-\infty}^{+\infty} G(j\omega + jn\omega_s) + g(o^+)/2 \qquad (2.1.3\text{-}3)$$

where

$G(s)$ is the quantity being starred
T is the sample period in seconds
ω_s is the sample rate in rad/s

and

$g(o^+)$ is the impulse response of $G(s)$ evaluated at $t = o^+$, i.e.,

$\lim_{s\to\infty} [s\, G(s)]$.

Provided that $G(s)$ has more poles than zeros, the series in Equation (2.1.3-2) converges. Pragmatic use of (2.1.3-3) is accomplished by truncating the series so that the frequency response is accurate to within a specified tolerance. Past experience has shown that no more than the first 20 positive and negative terms are needed, in general, for a significant five-digit accuracy. The importance of Equation (2.1.3-3) is that it makes the sampled-data frequency responses of the continuous portion of the system obtainable without performing the z-transform operations (a significant savings in computational effort).

The other frequency responses needed to complete the evaluation of (2.1.3-2) at specified frequencies are of the digital controller transfer function matrices, $D_1(Z)$ and $D_2(Z)$. Since the elements of these matrices are

assumed to be z-transfer functions, their frequency responses can be evaluated directly by letting $z = e^{j\omega T}$, i.e.,

$$D(e^{j\omega T}) = D(z)\Big|_{z = e^{j\omega T}} \qquad (2.1.3\text{-}4)$$

where

ω is frequency in rad/s
T is sample period in seconds

and

e is the natural log base.

Fig. 4 implies that both forward and feedback path digital controllers are to be used; however, in general only one or the other is needed. In the ICAT design process the specification of $[D_1(z)]$, $[D_2(z)]$ and R(z) provide efficient means of opening and closing loops and determining specific open loop frequency responses.

For example, if $[D_1(z)] = [0]$ then all loops are open. Specification of a controller for the row i, column j element of $[D_1(z)]$ with the remainder of the elements of $[D_1(z)]$ set to zero results in the closure of a loop from the jth output to the ith input through the digital controller represented by the specified element. Simultaneous or independent closure of as many loops as desired may be accomplished in this manner.

In the computation of open loop frequency responses, the input from which responses are being computed is acknowledged by specification of a value of 1+j0 over all frequency for the element of R(z) corresponding to that particular input, with the remaining elements of R(z) set equal to zero. The elements of the sampled-data output vector, C*(s), are then the frequency responses from the specified input to each of the outputs represented by the elements of C*(s). This is to say that each time C*(s) is computed,

a set of m frequency responses is generated, any or all of which may be of interest.

2.1.4 Application of Candidate Controller to ASCOT-I Structural Model.

Introduction

This section describes the application of the S2D2 candidate, 1CAT, to the ASCOT-I structural model as a test case. A full description of the ASCOT-I structure is given in Section 2.2.2 along with development of the dynamic model. The following paragraphs provide a description of the design model and the chosen control system architecture. A step by step examination of the loop closures and resulting stability margins is then given along with a summary of the compensation used. Finally, conclusions are presented.

ASCOT-I Design Model. The ASCOT-I design model is derived from the full order structural model of the LSS Ground Test Verification (LSS/GTV) facility structure housed at Marshall Space Flight Center (MSFC), Huntsville, Alabama. Use of this model was motivated by the desire to apply S2D2 to a real, existing LSS type structure. A complete description of the structure and accompanying facility appears in Section 2.2.2.

Modal truncation on the full order dynamic model is accomplished by simply including several modes with frequency less than the half sample frequency of the digital controller (25 Hz.). The simplicity of this structure and the resulting model alleviates the need for a more sophisticated truncation technique. The resulting design model includes three zero frequency rigid body modes, two "pendulum" modes, and seven flexible body modes. The zero frequency modes represent translation of the system at the Base Excitation System (BET) (two degrees of freedom), and rotation about the z-axis gimbal. The pendulum modes are actually rigid body in shape (rotation

about x and y) but have non-zero vibrational frequencies because of the effects of gravity upon the system. The remaining seven modes involve beam bending. Because of the symmetry of the structure, this model has no cross axis coupling. The 1CAT technique can handle systems which are coupled between axes. An example of application of 1CAT to such a system is given in Section 2.2.5.

The effector inputs for this design are torques applied to the structure by the three axis gimbal system. The measurements are the angular rates of the Advanced Gimbal System (AGS) faceplate about the x, y, and z axes.

Fig. 5 presents a block diagram of the ASCOT-I control system in the x-axis. The y-axis diagram is identical to Fig. 5 except that each "x" is replaced by "y" and vice versa. The z-axis model is similar also, except that the disturbance force input and line of sight (LOS) output are not defined for the z-axis. The LOS measurement is computed as described in Section 2.2.3. In each axis, feedback of the angular rate of the faceplate ($\dot{\theta}^*$) is used to add damping to the structural vibrations. The "outer" loop in each axis uses derived faceplate position ($\hat{\theta}^*$) to effect a position command loop. This type loop is considered necessary for pointing applications; however, note that faceplate angle is the controlled quantity rather than LOS directly. It is assumed in this analysis that LOS cannot be measured directly. The numerical integration used to derive faceplate position is accomplished in the strapdown algorithm (See Section 2.2.2) using quaternions such that all measurements used for control are with respect to the laboratory reference frame. For the purposes of control system design, the numerical integration can be represented by its z-transform and the coordinate transformations can be ignored.

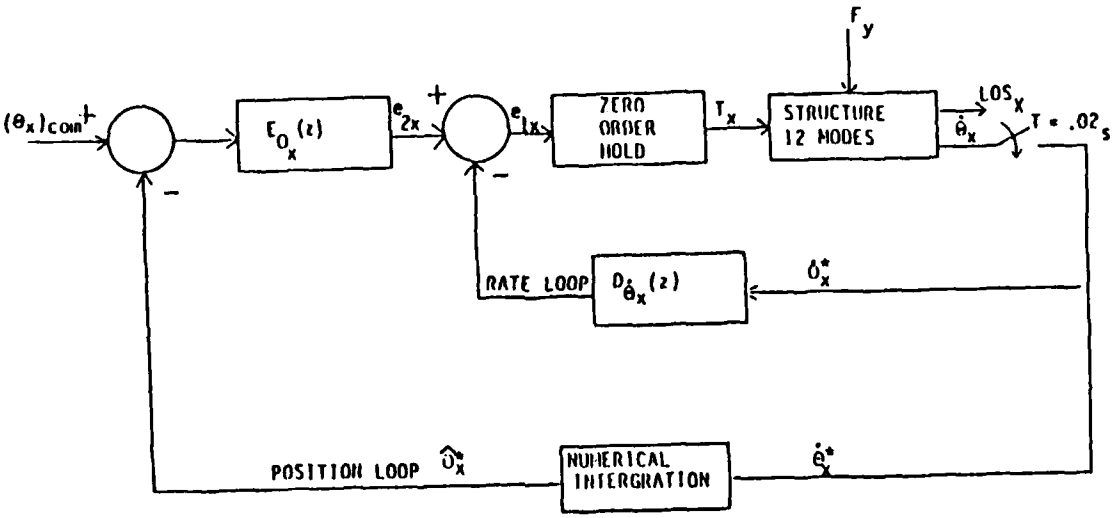

$(\theta_X)_{COM}$	- COMMANDED ANGLE ABOUT X	LOS_X	- LINE OF SIGHT
E_X	- DISCRETE CONTRL LAW OUTPUT	$\dot{\theta}_X$	- FACEPLATE ANGULAR RATE
T_X	- COMMANDED TORQUE ABOUT X	$\dot{\theta}^*_X$	- SAMPLED FACEPLATE ANGULAR RATE
F_Y	- DISTURBANCE FORCE INPUT	$\hat{\theta}^*_X$	- DERIVED FACEPLATE POSITION

Figure 5. ASCOT-I Control System X-Axis Block Diagram.

Design of the ASCOT-I Controller. The design of the compensation designated by $D_{\dot{\theta}_X}(z)$ and $E_{\theta_X}(z)$ is begun by examination of the transfer characteristic of $\dot{\theta}^*_X/e_{1X}$ which is shown in the Bode plot of Fig. 6. In exercising the 1CAT technique, loops are typically closed in order of decreasing control bandwidth. Examination of Fig. 6 indicates a phase response which lies between ±90° over much of the range of interest, which is expected for a loop using a rate measurement and a collocated actuator. This gives the rate loop promise of being the widest bandwidth of the two, which it is indeed. Also, this response lacks classical "rigid body" behavior even though the sensor and actuator can sense and effect this type of behavior. This is because the "rigid body" mode acts with a "pendulum" behavior, as described earlier, and reveals itself as what appears to be a flexible body mode at about one rad/sec. The pendulum behavior caused by gravity is the thing which must actually be controlled in the position loop, and this plays heavily in the design and resulting performance. It is considered by the author to be a worse case than that in zero g.

In choosing compensation for the rate loop, it is desired that as many magnitude peaks of the compensated loop frequency response as possible peak above OdB. This will introduce Modal Suppression by Phase Stabilization (MSPS) [1]. The higher a modal peak is above OdB, the more will be the damping for that mode in the transfer characteristic of the position loop with the rate loop closed. Obtaining MSPS for the flexible body modes is easily accomplished with a simple feedback gain in $D_{\dot{\theta}_X}(z)$; however, MSPS for the pendulum mode requires a loop gain of sufficient magnitude that dynamic compensation is required in $D_{\dot{\theta}_X}(z)$. Damping of the pendulum mode is important

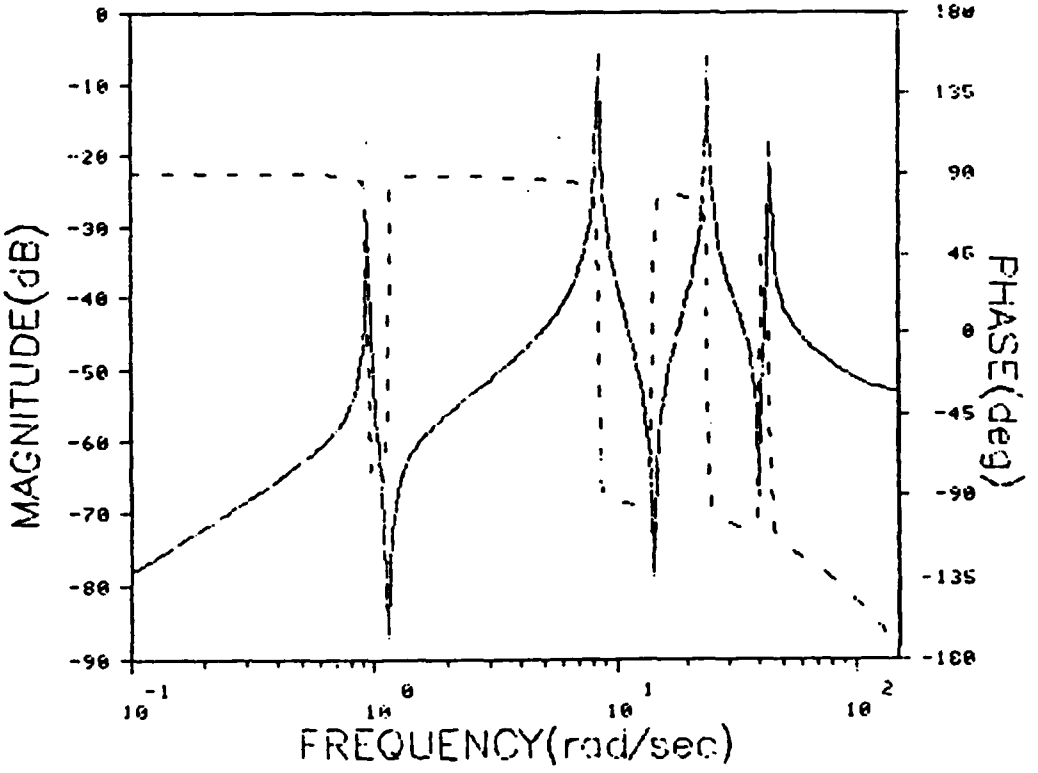

Figure 6. Sampled Data Frequency Response of Open X-Axis Faceplate Angular Rate Loop.

because, as mentioned before, this is the motion to be controlled by the position loop.

Using techniques described in [2], the rate loop compensation ($D_{\dot{\theta}_X}(z)$) is designed and is the cascade combination of a first order dominant pole, a lead compensator, a lag compensator, and a 55dB gain factor. The frequency response of $D_{\dot{\theta}_X}(z)$ is shown in Fig. 7, and its mathematical form is summarized along with that of the remainder of the compensation in TABLE 1.

The compensated rate loop frequency response ($\dot{\theta}_X^*/e_{1X} \cdot D_{\dot{\theta}_X}(z)$) is shown in the Bode plot of Fig. 8 and in the polar plot of Fig. 9. Application of the Nyquist stability criterion to Fig. 9 reveals a stable closed loop system with about 15dB of gain margin and 24° of phase margin.

The position loop design begins with examination of $\hat{\theta}_X^*/e_{2X}$ as shown in Fig 10. Note the reduced height of the modal peaks in this plot. An integration is immediately specified as part of the position loop compensation ($E_{\theta_X}(z)$) so that the system will be Type I and therefore have no steady state error due to a constant command input. Inclusion of the integrator characteristic in the position loop frequency response results in the Bode plot of Fig. 11. The loop could be stabilized at this point using a gain factor in addition to the integrator already chosen; however, the bandwidth would be very limited and/or the stability margins small. For this reason, a second order lead compensator having an underdamped zero pair and an underdamped pole pair is designed to phase stabilize the pendulum mode and, as a result, enhance the bandwidth of the position loop without sacrificing stability margins. The frequency response of the resulting compensation is shown in Fig. 12. The frequency range over which the compensation exhibits the large phase lead required to phase stabilize the pendulum mode is narrow, and use

TABLE 1. SUMMARY OF ASCOT-I COMPENSATION AND STABILITY MARGINS

	COMPENSATION ORDER		GAIN MARGIN, PHASE MARGIN	
	RATE LOOP	POSITION LOOP	RATE LOOP	POSITION LOOP
x-AXIS	3	3	15dB, 24°	10dB, 64°
y-AXIS	3	3	15dB, 30°	10dB, 61°
z-AXIS	0	0	4dB, 54°	36dB, 89°

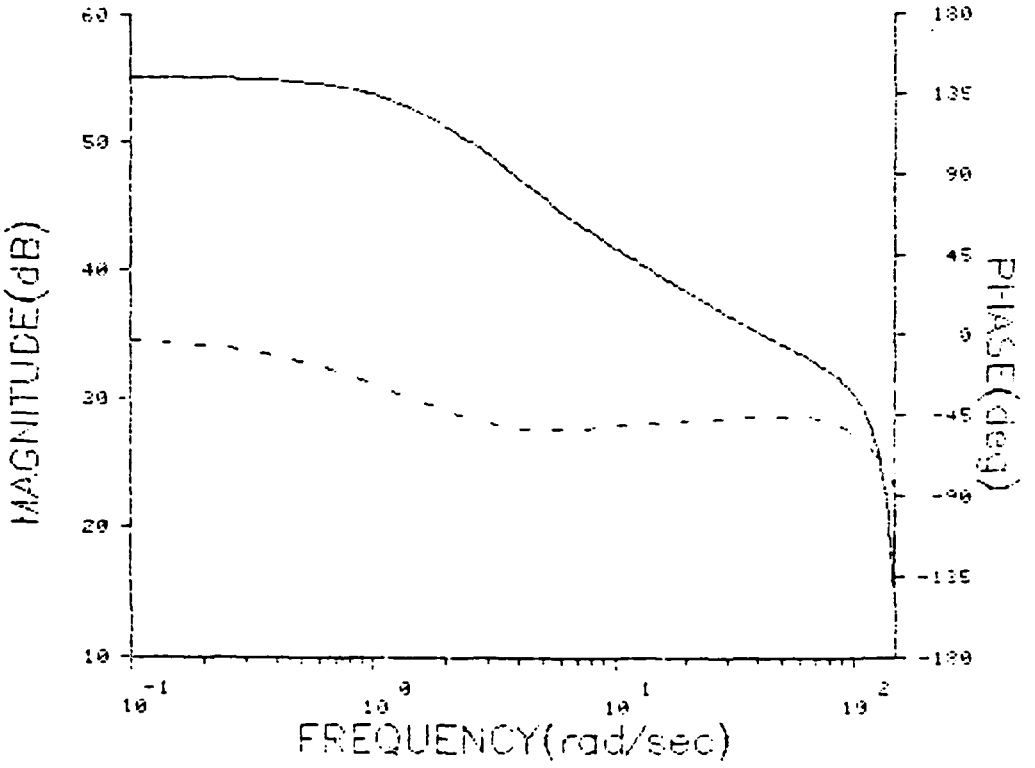

Figure 7. Frequency Response of X-Axis Rate Loop Compensation.

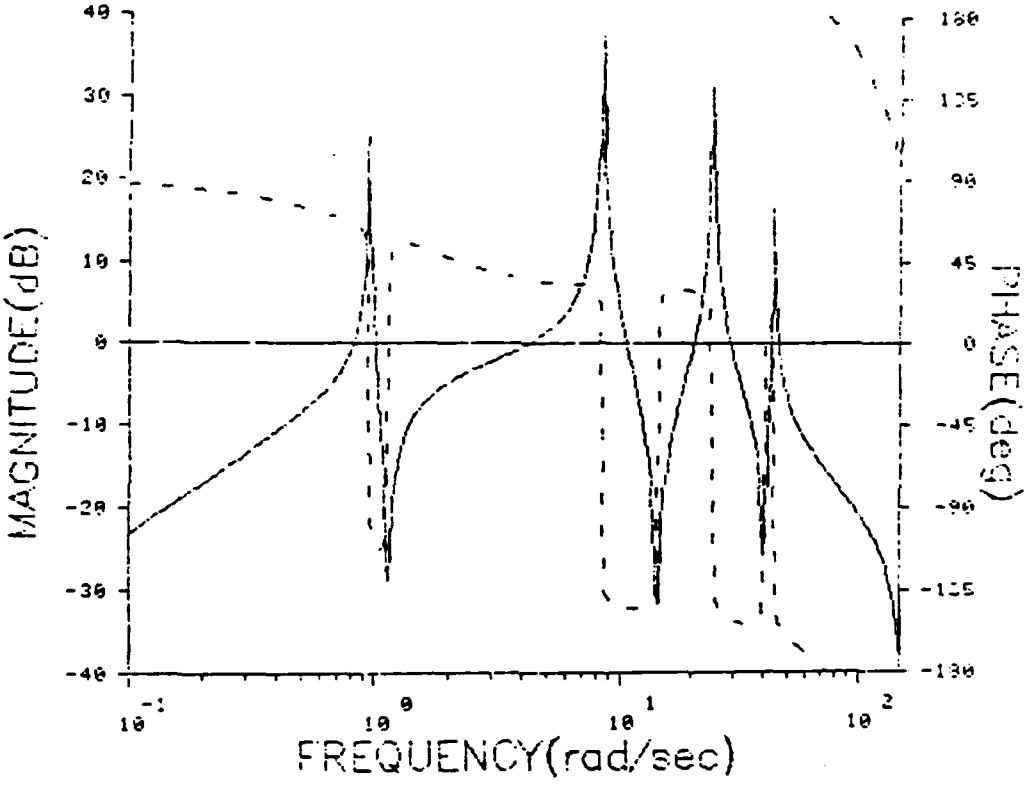

Figure 8. Frequency Response of Compensated X-Axis Rate Loop (Bode Plot).

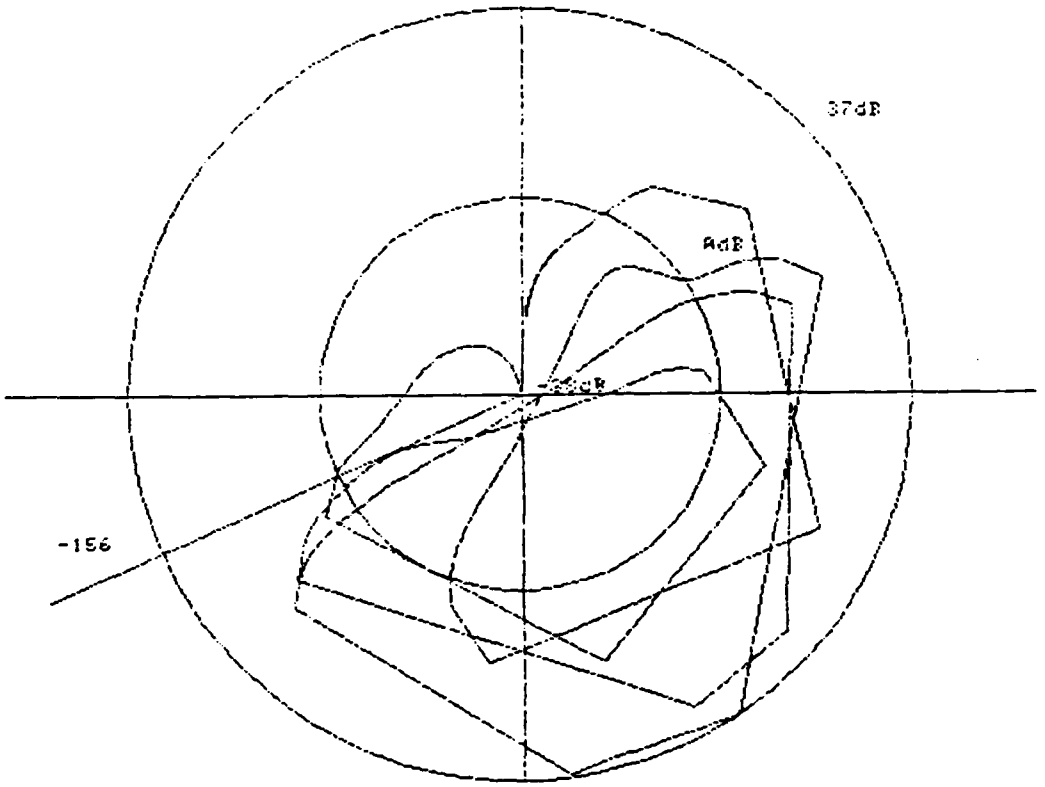

Figure 9. Frequency Response of Compensated X-Axis Rate Loop (Polar Plot).

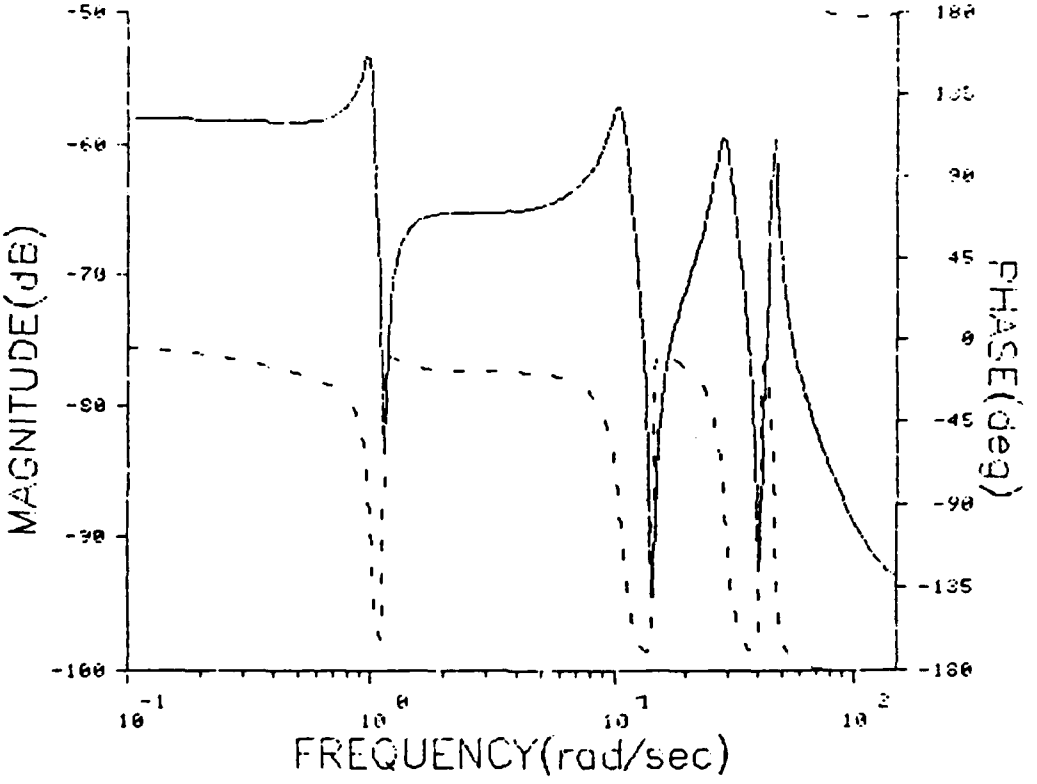

Figure 10. Frequency Response of Open X-Axis Position Loop with X-Axis Rate Loop Closed.

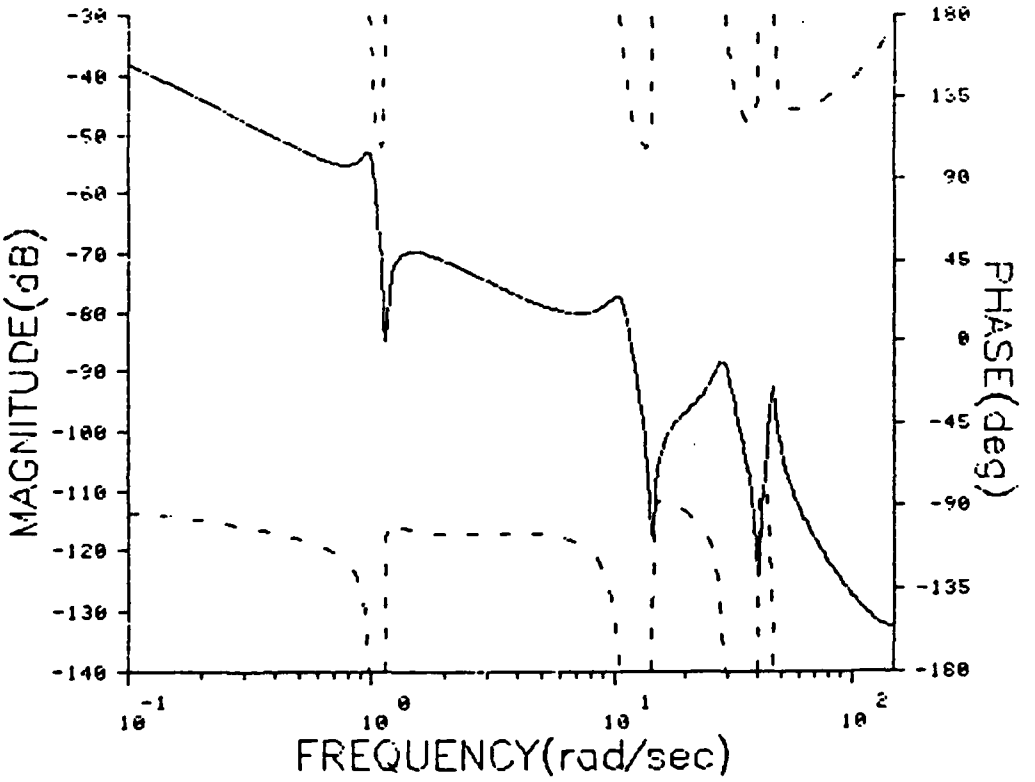

Figure 11. Frequency Response of Open X-Axis Position Loop Cascaded with an Integrator.

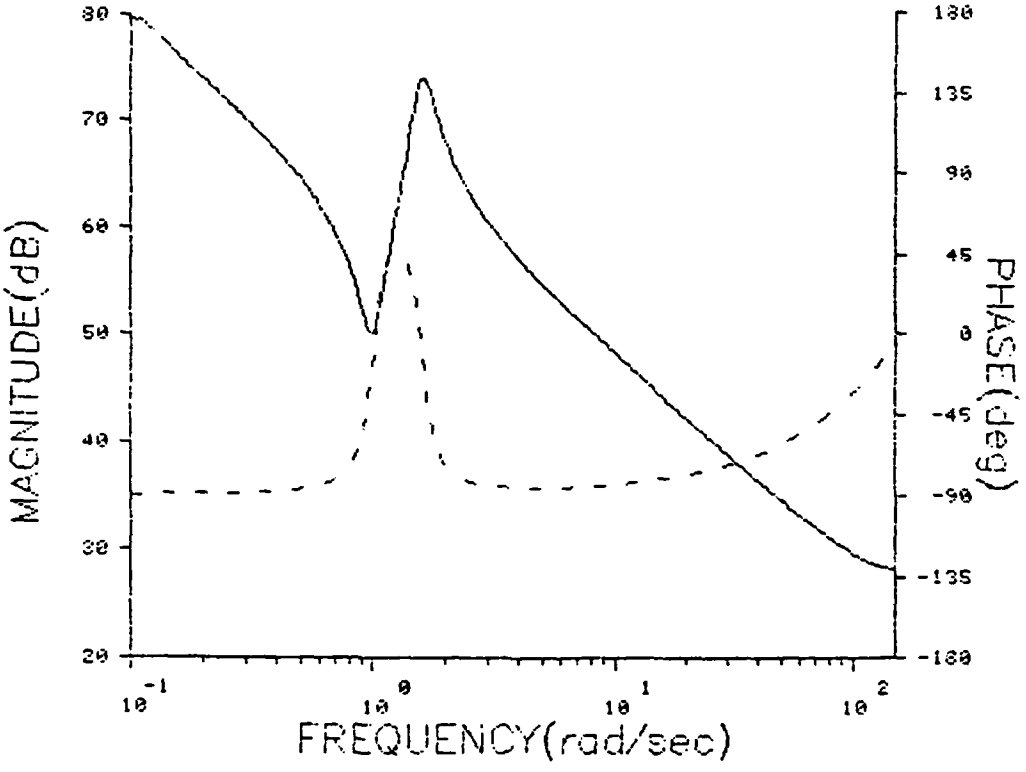

Figure 12. Frequency Response of X-Axis Position Loop Compensation.

of such compensation would typically be avoided because of robustness problems resulting from uncertainty of the modal frequency. However, the pendulum frequency is quite predictable and very consistent; therefore, compensation such as this is acceptable in this situation.

The position loop frequency response with the rate loop closed and all compensation included (both rate loop and position loop) is shown in the Bode plot of Fig. 13 and the polar plot of Fig. 14. Examination of Fig. 14 indicates a gain margin of 10dB and a phase margin of 64°.

Design of compensation for the y-axis control system is similar to that of the x-axis, and, in fact, the compensation differs only by the gain factors used. The y-axis compensation along with the resulting stability margins is summarized in TABLE 1.

The z-axis control system has an architecture similar to that of the x and y-axes and is designed in much the same manner. However, it is of much less interest here for three reasons: (1) it is not a pointing axis, (2) it in no way affects the LOS pointing because of the decoupled nature of the dynamic model, and (3) only one flexible body mode appears in the frequency range of interest, and therefore the design is relatively simple. For these reasons, the z-axis design is not discussed in detail; however, the compensation and resulting stability margins are included in TABLE 1.

Conclusions regarding the ASCOT-I design. Design of a three axis control system for the ASCOT-I model using the candidate S2D2, 1CAT, has been demonstrated. The resulting design produces a stable closed loop system with a reasonable amount of robustness as indicated by the stability margins of TABLE 1. The ASCOT-I model does not provide a very challenging problem for 1CAT because of the decoupled nature of the model. It does, however, provide

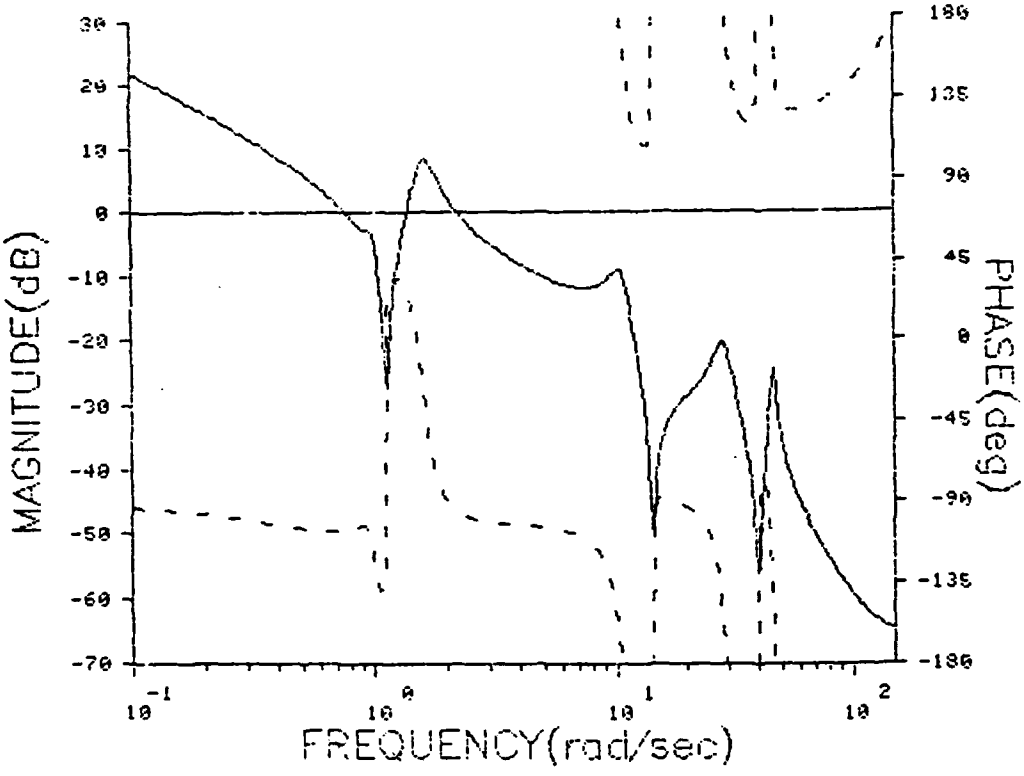

Figure 13. Frequency Response of Compensated X-Axis Position Loop with X-Axis Rate Loop Closed (Bode Plot).

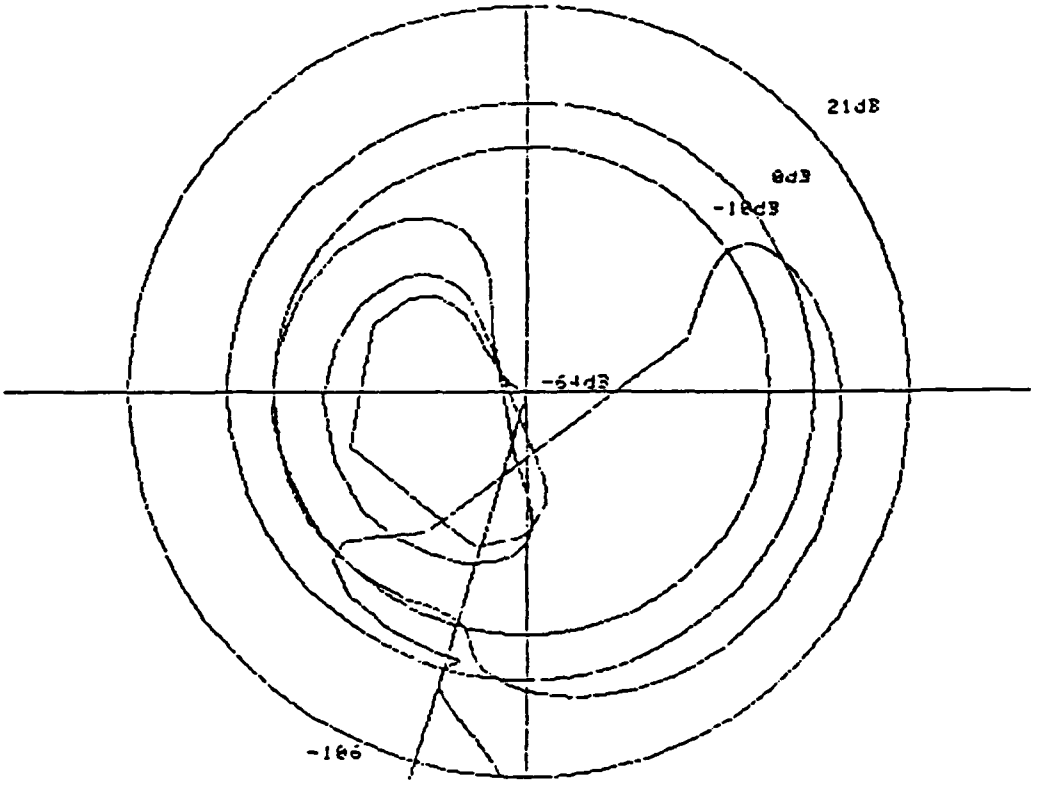

Figure 14. Frequency Response of Compensated X-Axis Position Loop with X-Axis Rate Loop Closed (Polar Plot).

the reader with an introduction to the step by step nature of ICAT and the accompanying stability checks. A more thorough application of ICAT is provided in Section 2.2.5. Section 2.1.6 discusses the performance and time domain stability of the ASCOT-I design.

2.1.5 Design of Prefilters.

Introduction. The effect of unmodeled high frequency system components is often neglected in the design of sampled-data control systems. The rationale for leaving these components unmodeled is that they will either not be excited or will contribute very little to the low frequency characteristics.

The advent of Large Space Structures (LSS) with significant high frequency flexible modes introduces almost a worst case of unmodeled high frequency components. A legitimate concern for control systems designers for such structures is whether neglecting the high frequency modes contributes to system performance degradation.

Since control systems for LSS are envisioned to be sampled-data in nature, the main problem expected to occur is that of aliasing. The phenomenon of aliasing is most easily understood by considering the Laplace Transform of the output of an ideal sampler with an input signal whose Laplace Transform is X(s) (See Fig. 15.).

It can be shown that

$$X^*(s) = \frac{1}{T} \sum_{n=-\infty}^{\infty} X(s + jn\omega_s) \qquad (2.1.5\text{-}1)$$

where ω_s is the sampling frequency in rad/sec. Figure 16 is a representation of the s-plane with the poles of X(s) shown schematically.

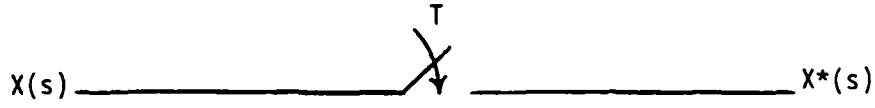

Figure 15. Representation of an Ideal Uniform Rate Sampler with Sampling Period T Seconds.

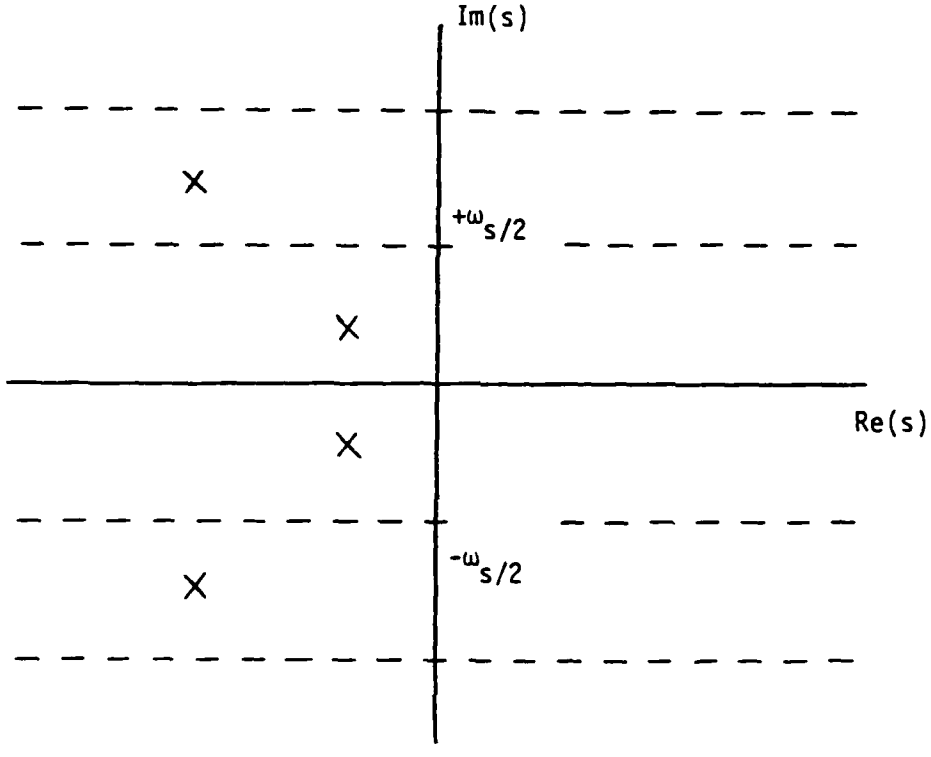

Figure 16. S-Plane Plot of the Poles of X(s) Used for Illustrating the Aliasing Phenomenon.

Examination of Equation (2.1.5-1) results in the conclusion that, if X(s) has poles at $\sigma_1 \pm j\omega_s/4$ and $\sigma_2 \pm j\omega_s 3/4$ then X*(s) has poles at $\sigma_1 \pm j\omega_s/4 \pm jn\omega_s$ and $\sigma_2 \pm j\omega_s 3/4 \pm jn\omega_s$. In particular X*(s) has poles at $\sigma_2 \pm j\,\omega_s/4$ and $\sigma_1 \pm j\,\omega_s/4$, the significance being that two poles are now within the primary strip ($-\omega_s/2 < \omega < \omega_s/2$) that do not appear there for the unsampled X(s). These two poles are said to have aliased back into the primary strip and can cause serious stability problems since a control system containing an ideal sampler may introduce low-frequency poles that the designer has not considered.

The problem of aliasing is usually solved in two ways. First the designer may know that his system is effectively bandlimited and choose the sampling period so that $\omega_s/2$ is greater than the highest significant frequency. Alternatively the designer may decide that the additional hardware required to implement a very fast sampled-data control system is not justified. In this case analog prefiltering is used to bandlimit the system to a reasonable frequency range by inserting a low pass filter with a cutoff frequency chosen so that the undesirable high frequency components are significantly attenuated at frequencies higher than $\omega_s/2$.

Two alternatives to the approach of analog prefiltering are presented here. The first method involves using a digital prefilter with a faster uniform sampling rate. The second method involves a non-uniform sampling rate with an average rate slower than that used by a corresponding fast uniform rate prefilter.

Different justifications exist for each of the two approaches. In the case of the fast uniform rate prefilter, the additional hardware cost can be kept comparitively low by the use of dedicated hardware.

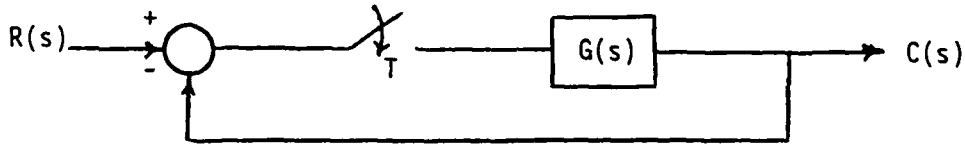

Figure 17. Basic Sampled-Data Feedback System Used to Illustrate Aliasing.

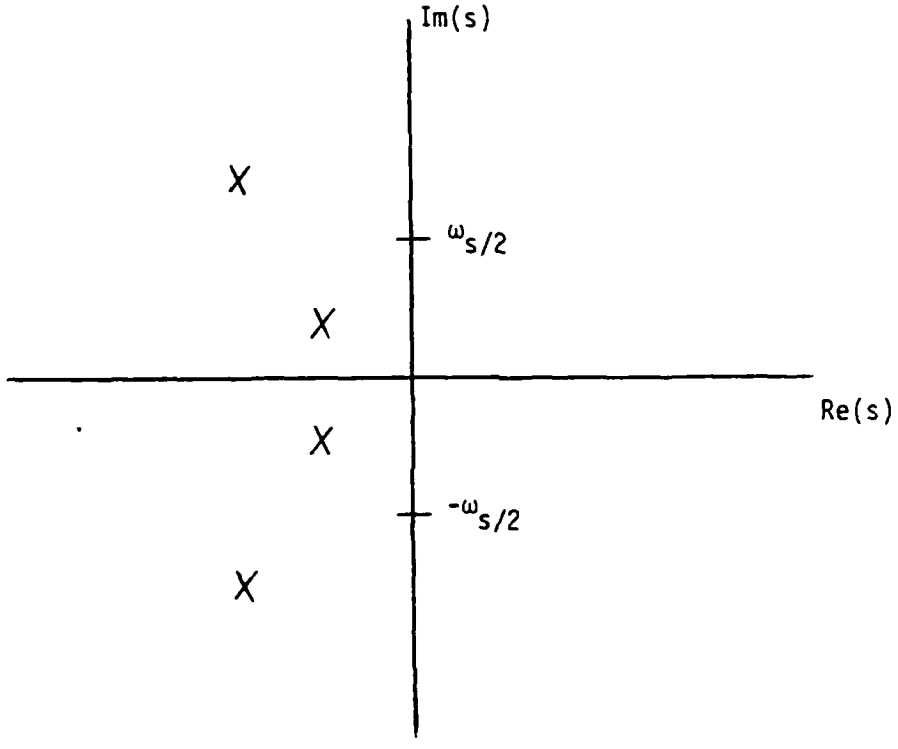

Figure 18. S-Plane Plot of the Poles of G(s) Used for Illustrating the Aliasing Phenomenon.

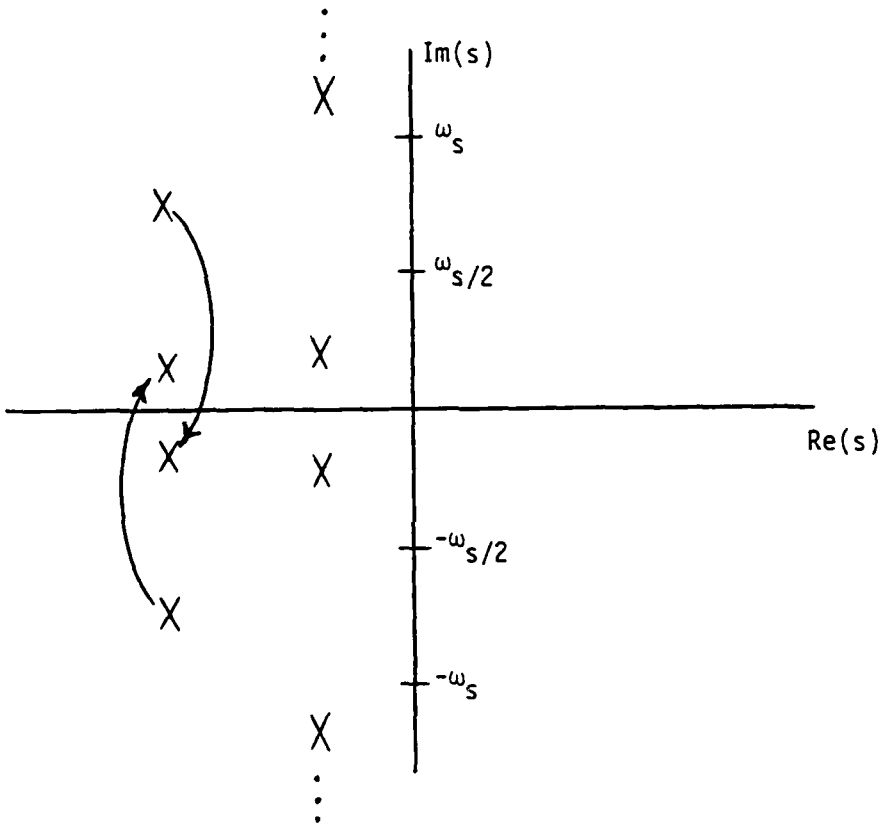

Figure 19. S-Plane Plot of the Poles of G*(s) with Aliased Poles.

The non-uniform rate prefilter, if proven practicable, has the advantage that extremely fast sampling is not required.

Before examining the two prefilter schemes in detail, it is worthwhile to consider the circumstances in which aliasing may lead to stability and/or performance degradation. The most efficient method of examining this problem is by considering the s-plane representation of pole locations.

Consider the basic sampled-data feedback system of Figure 17. Suppose G(s) has 2 poles inside the primary strip and 2 poles outside the primary strip. The poles of G(s) are shown on the s-plane in Figure 18. Compensator design is generally effected in a sampled data system through use of the sampled data loop frequency response. In this case the loop response is G*(s), whose poles are represented in Figure 19. Two poles have now "aliased back" into the primary strip where none had previously appeared. Now the system stability is determined by the sampled-data characteristic equation:

$$\Delta(s) = 1 + G^*(s) = 0 \qquad (2.1.5\text{-}2)$$

Clearly, G*(s) is periodic with period $j\omega_s$. Hence G*($j\omega$) is completely described by the portion of the $j\omega$ axis between $-\omega_s/2$ and $+\omega_s/2$. Normally, the periodicity of the poles of G*($j\omega$) contribute very little to its value in this range, as G($j\omega$) is assumed to have no significant values for frequencies above ω_s. However, if this is not true, which is the case when aliasing occurs, G*($j\omega$) can be affected so as to cause a degradation in stability. It should be pointed out that an actual aliasing of poles is not required for a stability degradation. In fact, whenever G($j\omega$) has significant components at frequencies higher than $\omega_s/2$ stability can be affected. It is for this

reason that the effect of decreasing stability margins in a sampled-data system is termed "frequency folding."

A topic of particular interest to designers of Large Space Structures is that of lightly damped modes which may unavoidably occur at frequencies higher than $\omega_s/2$. While the existence of such modes has been the subject of great concern, it should be noted that when these modes are aliased below $\omega_s/2$, there exists a bound on the damping ratio, based on the fact that the real part of the resulting aliased poles cannot change whereas the imaginary part of the poles may be much reduced.

Fast Uniform Rate Prefilters. The effect of prefilters on aliasing phenomenon can be considered from either a signal or loop gain point of view. In the signal point of view, the designer inserts a prefilter in order to eliminate the excitation of undesirable high frequency system characteristics. For the loop gain, or feedback, point of view the designer considers the function of the prefilter as reducing the loop bandwidth of the system, hence eliminating the high frequency system components of concern. Both of the above mentioned ways of visualizing the function of an anti-aliasing prefilter are equally valid and both concepts can be used interchangeably.

The concept of digital prefiltering arises naturally in the scenario of on-orbit control system redesign. For example, earth bound designers may desire, after in-flight testing, to incorporate in the control system design previously unmodeled modes. These modes, if they occur at frequencies above the cut-off frequency of the prefilters, can be uncontrollable. An analog prefilter with its fixed cutoff frequency would not allow the designers to take advantage of the in-flight data. On the other hand, designers can easily change the cutoff frequency of a digital prefilter from the ground.

However, from the previous discussion of the effect of sampling it should be clear that a digital prefilter cannot filter at frequencies above $\omega_s/2$, a direct consequence of the periodicity of the sampled data frequency response.

The unfortunate fact that the cutoff frequency of uniform rate digital prefilters is limited by $\omega_s/2$ leads swiftly to the conclusion that the sampling rate associated with the prefilter must be very high to ensure that all significant high frequency components are attenuated. The practicality of such a filter is determined by whether it is feasible to implement such a high rate filter with available hardware and whether it can be assumed that the system can be considered effectively bandlimited to a reasonable frequency range.

If the sampling rate is limited only by the speed at which digital filter calculations can be made then the possibility exists that a dedicated hardware digital prefilter is practical. On the other hand, if the sampling rate is limited by the availability of data, the probability is that a fast uniform rate digital prefilter will be impractical.

The design of a fast uniform rate digital prefilter is straightforward. First, the fast sampling rate associated with the digital prefilter should, if possible, be at least ten times the sampling rate associated with the slower digital controller in order to minimize the fast rate sampler's effect on the overall system design.* Second, the cut-off frequency of the prefilter should be selected to be at or below the half sample rate of the controller. Commonly a simple second order low pass characteristic is chosen, with its

*If the fast rate sampler is too slow, then multirate design techniques may be required [3].

pair of complex conjugate poles critically damped at a frequency of $\omega_{s/2}$ (slow rate). Such a filter offers an acceptable tradeoff between gain and phase contribution, translating to a tradeoff between system stability and system response time.

Non-Uniform Rate Sampling. The ideal marriage of the fast rate digital prefilter and the analog prefilter is a prefilter which is digital in nature while at the same time not requiring a very fast sampling scheme. Such a filter, while not possible with standard uniform rate sampling schemes, may be possible if unconventional sampling schemes are used. In order to see that aliasing is closely related to the sampling scheme, the sampling process is modeled as an impulse modulator, as in Figure 20, with p(t) a periodic train of impulses, i.e.,

$$p(t) = \sum_{n=0}^{\infty} \delta(t - nT). \tag{2.1.5-3}$$

It is well known that

$$\mathcal{L}\{x(t)p(t)\} = X(s)*P(s) \tag{2.1.5-4}$$

where $\mathcal{L}\{\ \}$ denotes the Laplace Transform operator, * denotes the operation of complex convolution, and X(s) and P(s) are the Laplace transforms of x(t) and p(t), respectively. The Laplace transform of p(t) can easily be evaluated as

$$P(s) = \sum_{n=0}^{\infty} e^{-nsT} = \frac{1}{1 - e^{-sT}}. \tag{2.1.5-5}$$

From Equation 4

$$X^*(s) = \frac{1}{2\pi j} \int_{c-j\infty}^{c+j\infty} X(u) \cdot \frac{1}{1 - e^{-T(s-u)}}\, du$$

$$= - \sum \text{ residues of } \frac{X(u)}{1 - e^{-T(s-u)}} \tag{2.1.5-6}$$

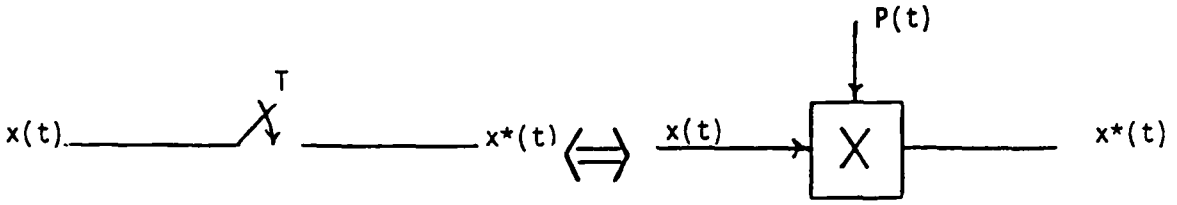

Figure 20. Impulse Modulator Representation of the Ideal Uniform Rate Sampler.

at the poles of $\dfrac{1}{1 - e^{-T(s-u)}}$.

Now there are poles of $\dfrac{1}{1 - e^{-T(u-s)}}$ at $u = s \pm jn\omega_s$, $n = 0, 1, \ldots$ and the corresponding residues are $X(s \pm jn\omega_s)/T$. Hence $\underline{X}^*(s)$ can be written

$$X^*(s) = \frac{1}{T} \sum_{n=-\infty}^{\infty} X(s + jn\omega_s), \tag{2.1.5-7}$$

and, as discussed previously, the aliased poles and frequency folding occur because of the sidebands generated by Equation (2.1.5-7). It should be clear from the development of Equation (2.1.5-7) that these effects are immediate consequences of the periodicity of the poles of P(s), which in turn results from the periodicity of the sampling impulse train p(t).

Because the sidebands which cause aliasing and frequency folding are results of the periodicity of the sampling process, an alternate non-periodic sampling scheme is proposed which, at least theoretically, does not cause aliasing. This alternate sampling scheme has the desirable feature of having a minimum time between samples, thus allowing implementation without the unrealistic requirement of obtaining samples arbitrarily close together in time. A digital prefilter is included to investigate the possibility of filtering above the "average" half sample rate associated with the sampling process.

The *non-uniform* rate sampling process is defined by the following steps.

1. A sample is assumed to be obtained at $t = 0$.
2. The next sample time is determined from a random number generator uniformly distributed on the interval $[T_{min}, T_{max}]$.

The resulting sample of the random number generator is added to the previous sample time to determine the time of the next sample. Mathematically the sampling process is again modeled as an impulse modulator with impulse train p(t) defined by

$$p(t) = \delta[t - (T + \ldots + T_n)] \qquad (2.1.5.8)$$

where the T_i's are independent random variables uniformly distributed on the interval $[T_{min}, T_{max}]$.

In order to prove that the sampling process does not introduce sidebands, an expression for the output power spectral density (PSD) in terms of the input PSD must be derived. Since the output of the sampler is the product of the input x(t) and the modulating impulse train p(t) the autocorrelation function of the output y(t) can be written as follows:

$$R_{yy}(\tau) = E[y(t + \tau)y(t)] = E[x(t + \tau)p(t + \tau)x(t)p(t)] \qquad (2.1.5\text{-}9)$$

Since x(t) and p(t) are statistically independent,

$$R_{yy}(\tau) = E[x(t + \tau)x(t)]\ E\ [p(t + \tau)p(t)] = R_{xx}(\tau)\ R_{pp}(y) \qquad (2.1.5\text{-}10)$$

Then the PSD of the output is

$$S_y(\omega) = S_x(\omega) * S_p(\omega) \qquad (2.1.5\text{-}11)$$

since the PSD is simply the Fourier transform of the autocorrelation function. An important fact to note is that if $S_p(\omega) = \delta(\omega)$, then $S_y(\omega) = S_x(\omega)$; a very desirable result since there are no sidebands in this case.

Equation 11 implies that if $S_p(\omega)$ is a good approximation of $\delta(\omega)$, then aliasing should not be a significant problem. The PSD of p(t) can be found by observing that [4]

$$S_x(\omega) = \lim_{T \to \infty} E\left[\frac{1}{T} | P_T(j\omega) |^2\right] \qquad (2.1.5\text{-}12)$$

where T is the time interval of p(t) used to obtain the Fourier transform $P_T(j\omega)$. For a given T, there is always a k such that

$$P_T(t) = \delta(t) + \delta(t - T_1) + \ldots + \delta(t - T_1 - T_2 \ldots - T_k) \qquad (2.1.5.13)$$

so that the Fourier transform of $P_T(t)$ is

$$P_T(j\omega) = 1 + e^{-j\omega T_1} + \ldots + e^{-j\omega(T_1 + \ldots T_{k-1})}. \qquad (2.1.5.14)$$

Hence,

$$\frac{1}{T}\left| P_T(j\omega) \right|^2 = \frac{1}{T_1 + \ldots + T_k} (1 + \ldots + e^{-j\omega(T_1 + \ldots + T_{k-1})}) \cdot (1 + \ldots + e^{j\omega(T_1 + \ldots + T_{k-1})}) \qquad 2.1.5\text{-}15$$

Equation (2.1.5-15) can be written as

$$\begin{aligned}
\frac{1}{T}\left| P_T(j\omega) \right|^2 = {} & \frac{k}{T_1 + \ldots + T_k} \\
& + \frac{1}{T_1 + \ldots + T_k} [e^{j\omega T_1} + \ldots + e^{j\omega(T_1 + \ldots + T_{k-1})}] \\
& + \frac{1}{T_1 + \ldots + T_k} [e^{j\omega T_2} + \ldots + e^{j\omega(T_2 + \ldots T_{k-1})}] \\
& + \quad \vdots \\
& + \frac{1}{T_1 + \ldots + T_k} e^{j\omega T_{k-1}} \\
& + \frac{1}{T_1 + \ldots + T_k} [e^{-j\omega T_1} + \ldots + e^{-j\omega(T_1 + \ldots + T_{k-1})}] \\
& + \quad \vdots \\
& + \frac{1}{T_1 + \ldots + T_k} e^{-j\omega T_{k-1}} .
\end{aligned} \qquad (2.1.5\text{-}16)$$

Now, as T gets large $\frac{1}{T_1 + \ldots + T_k}$ approaches $\frac{1}{kT_a}$, where T_a is the mean value of each of the T_i's. The required expectation can be found term by term from Equation (2.1.5-16). Since the T_i's are identically distributed,

$$E[e^{j\omega T_i}] = E[e^{j\omega T_j}] \text{ for any } i \text{ and } j. \qquad (2.1.5\text{-}17)$$

Also, since the T_i's are independent,

$$E[e^{j\omega(T_1 + \ldots + T_{k-1})}] = E[e^{j\omega T_1}] \ldots E[e^{j\omega T_{k-1}}]$$
$$= E[e^{j\omega T_i}]^{k-1}. \qquad (2.1.5\text{-}18)$$

The probability density function of each T_i is

$$f_{T_i}(T_i) = \begin{cases} 1/(T_{max} - T_{min}) & ; \ T_{min} \leq T_i \leq T_{max} \\ 0 & ; \text{ otherwise.} \end{cases} \qquad (2.1.5\text{-}19)$$

Define

$$X_p = E[e^{j\omega T_i}] = \frac{1}{T_{max} - T_{min}} \int_{T_{min}}^{T_{max}} e^{j\omega T_i} \, dT_i$$
$$= \frac{e^{j\omega T_{max}} - e^{j\omega T_{min}}}{j\omega(T_{max} - T_{min})} \qquad (2.1.5\text{-}20)$$

and

$$X_n = E[e^{-j\omega T_i}] = \frac{e^{-j\omega T_{min}} - e^{-j\omega T_{max}}}{j\omega(T_{max} - T_{min})}. \qquad (2.1.5.21)$$

Substituting into Equation (2.1.5-16) and gathering terms,

$$E\left[\frac{1}{T}|P(j\omega)|^2\right] = \frac{1}{T_a} + \frac{k-1}{kT_a} X_p + \frac{k-1}{kT_a} X_n$$
$$+ \frac{k-2}{kT_a} (X_p)^2 + \frac{k-2}{kT_a} (X_n)^2 + \ldots \qquad (2.1.5\text{-}22)$$

Taking the limit as $k \to \infty$ gives

$$S_p(\omega) = \frac{1}{T_a} + \frac{1}{T_a}\left[\frac{1}{1 - X_p} - 1\right] + \frac{1}{T_a}\left[\frac{1}{1 - X_n} - 1\right] . \qquad (2.1.5\text{-}23)$$

Investigation of Equation (2.1.5-23) yields the desirable result that $S_p(\omega)$ is indeed an approximation of an impulse centered at zero with a constant term $1/T_a$. From the previous discussion of the desirable form of $S_p(\omega)$, it is expected that the non-uniform rate sampler greatly reduces aliasing phenomenon. However, the question of whether a suitable digital prefilter is possible using the sampling scheme is unresolved. A theoretical discussion of the digital prefilter using a non-uniform rate sampling scheme is very difficult, if not impossible, and is not included here except to suggest future study on the matter. However, computer simulations with such a prefilter were carried out in order to assess its practicality. The system simulated along with the simulation results are presented in the following sections.

Non-Uniform Rate Digital Prefilter Simulation Results. Computer simulation results for a typical system subject to aliasing problems are included. The non-uniform rate digital prefilter is observed to improve the system performance only as concerns the effects of aliasing. The overall system response exhibits a degradation in stability margins.

Assume that one is required to control a double integrator system with a transfer function given by

$$G(s) = \frac{k_1}{s^2} \qquad (2.1.5\text{-}24)$$

Also, assume that this particular system exhibits an unknown vibrational mode so that the actual plant transfer function is given by

$$G(s) = \frac{k_1}{s} + \frac{k_2\,\omega_n^2}{s^2 + 2\zeta\omega_{n_s} + \omega_n^2} \quad . \qquad (2.1.5\text{-}25)$$

A block diagram for this system is shown in Fig. 21. In this block diagram $D_1(z)$ is a digital compensator with a uniform rate sampler and $D_2(z)$ is a digital prefilter with a non-uniform rate sampler. Note that the compensator precedes the prefilter in the forward path of this system; however, this need not be the case.

Since the vibrational characteristics of this plant are unknown to the system designer, Equation (2.1.5-24) will be used to choose a suitable uniform sample rate and design the compensator $D_1(z)$. In this example the uniform sample rate is chosen to be 200 rad/sec. The gain k_1 in Equation 24 is chosen to be 177.8 so that the sampled-data frequency response of the plant crosses zero dB at approximately 13 rad/sec. A lag-lead compensator is now designed so that the loop gain crossover frequency remains 13 rad/sec with a phase margin of 40 degrees and a gain margin of about 12 dB. The transfer function for this compensator is given by

$$D_1(z) = \frac{.3019\ z - .2864}{z - .9845} \quad \frac{7.039\ z - 6.21}{z - .1707} \quad . \qquad (2.1.5\text{-}26)$$

Fig. 22 shows a Bode plot of the compensated loop frequency response and Fig. 23 shows a unit step response for the compensated system.

For the purposes of the example it is now necessary to choose the dc gain, damping ratio, and natural frequency for the unmodeled vibrational mode so that an alias occurs in such a way as to adversely effect the stability of the system. Two such cases are chosen for this example. In both cases the alias frequency is 50 rad/sec. For Case 1 the natural frequency is chosen to be 150 rad/sec, the damping ratio is .01, and the gain k_2 is .02. A Bode

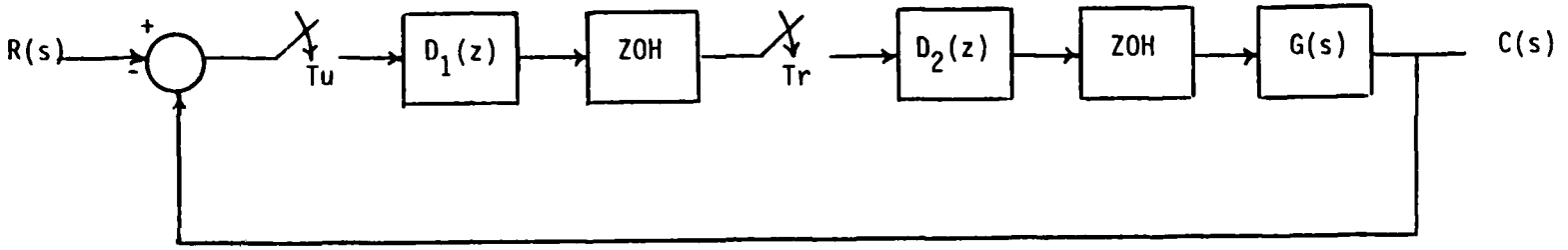

Figure 21. Sampled-Data Feedback System Including Uniform Rate Compensation and Non-Uniform Rate Prefilter.

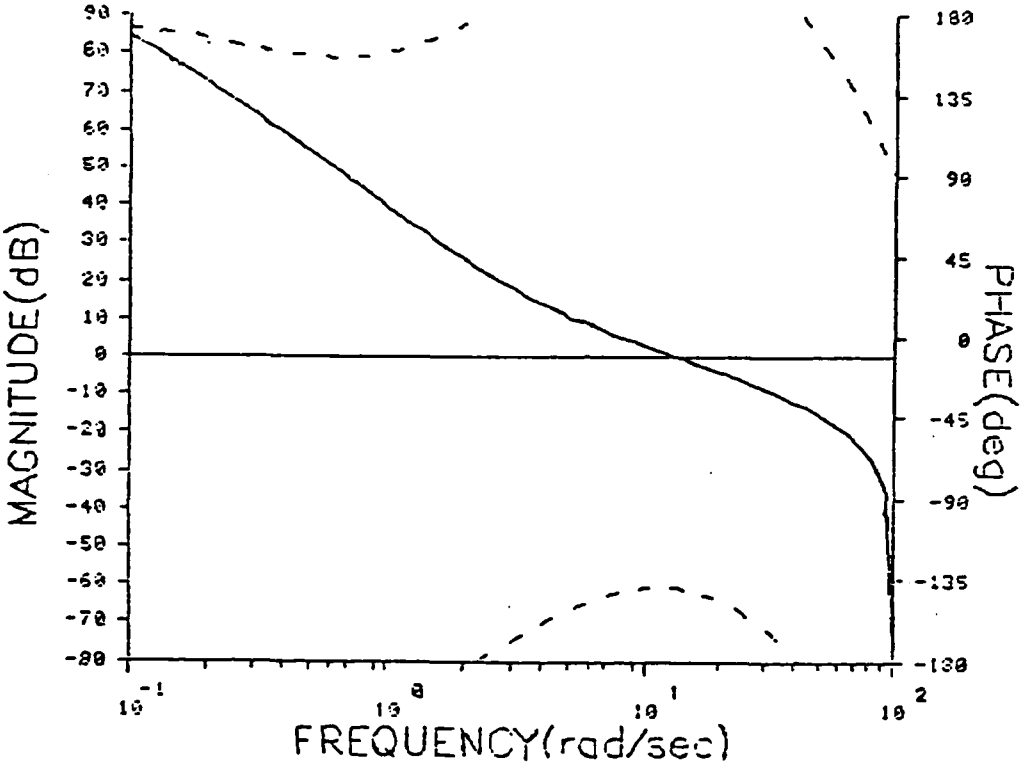

Figure 22. Compensated Loop Frequency Response without Bending Mode.

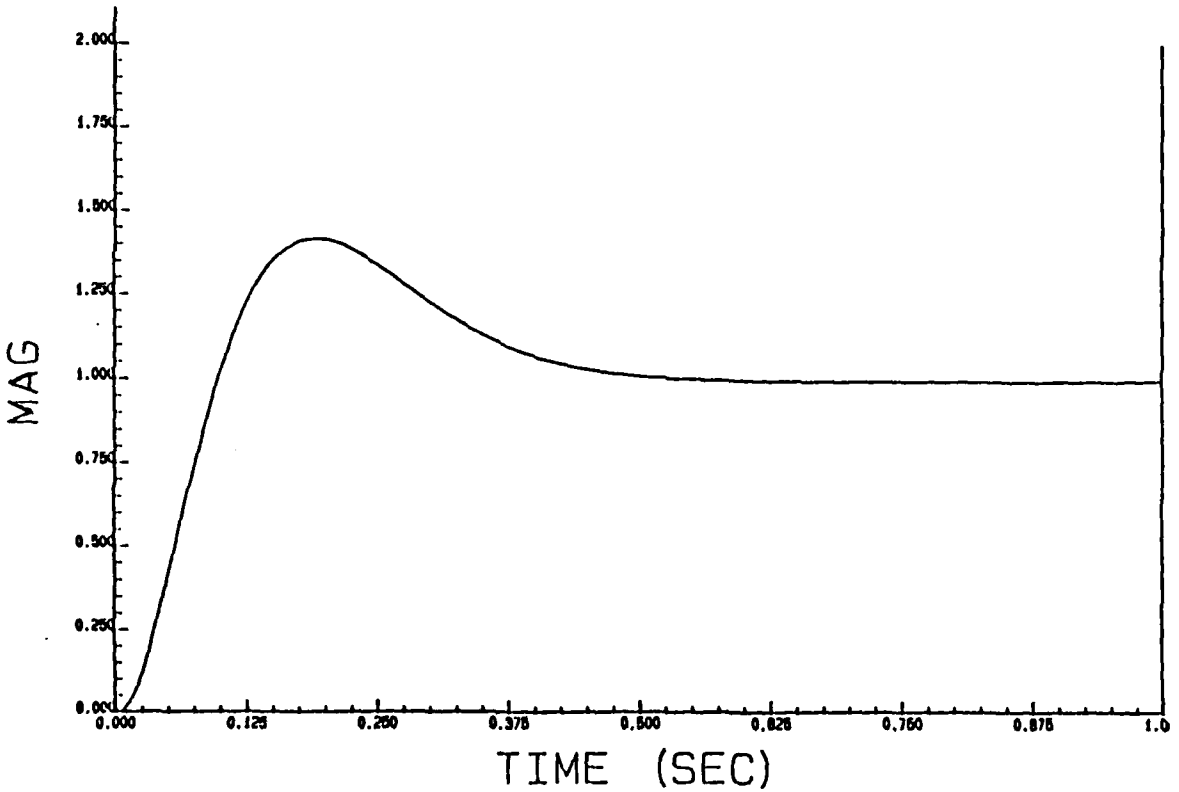

Figure 23. Step Response of Compensated System without Bending Mode.

plot of the sampled-data loop frequency response of the compensated system with this vibrational mode is shown in Fig. 24. The resonant peak due to the alias results in a very low (approximately 3 dB) gain margin so that the closed loop system should exhibit an oscillatory time response.

For Case 2 the vibrational mode natural frequency is chosen to be 350 rad/sec, the damping ratio is .005, and k_2 is .02. A Bode plot of the loop frequency response of the compensated system with this vibrational mode is shown in Fig. 25.

Fig. 26 shows the unit step response of the system with the 150 rad/sec vibrational mode, and Figure 27 shows the response of the system with the 350 rad/sec vibrational mode. The oscillatory behavior of both of these responses illustrates the need for a prefilter to reduce the effects of the alias.

The prefilter should be designed in such a way as to preserve the stability margins obtained with the compensator designed above. For this example a second order low pass filter with a natural frequency of 88 rad/sec and a damping ratio of .3 is chosen. This filter should contribute less than 5 degrees of phase lag at the loop gain crossover frequency (13 rad/sec) and only about 3 dB of gain at the loop phase crossover frequency (40 rad/sec). Therefore, the loop stability margins are not greatly effected by this filter. Also, the filter should provide about 8 dB of attenuation at 150 rad/sec and about 25 dB at 350 rad/sec. This attenuation should greatly reduce the oscillatory effects of the alias. The transfer function for the analog pre-filter is given by

$$G_2(s) = \frac{7767}{s^2 + 52.88s + 7767} . \qquad (2.1.5\text{-}27)$$

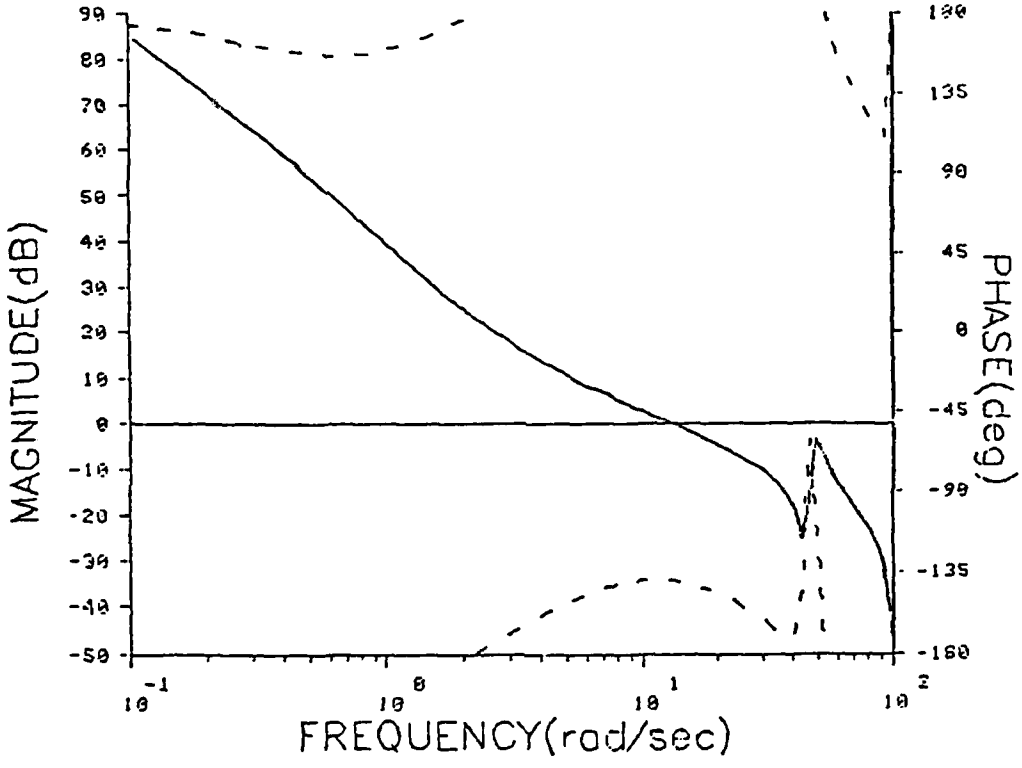

Figure 24. Loop Frequency Response with Bending Mode at 150 rad/sec.

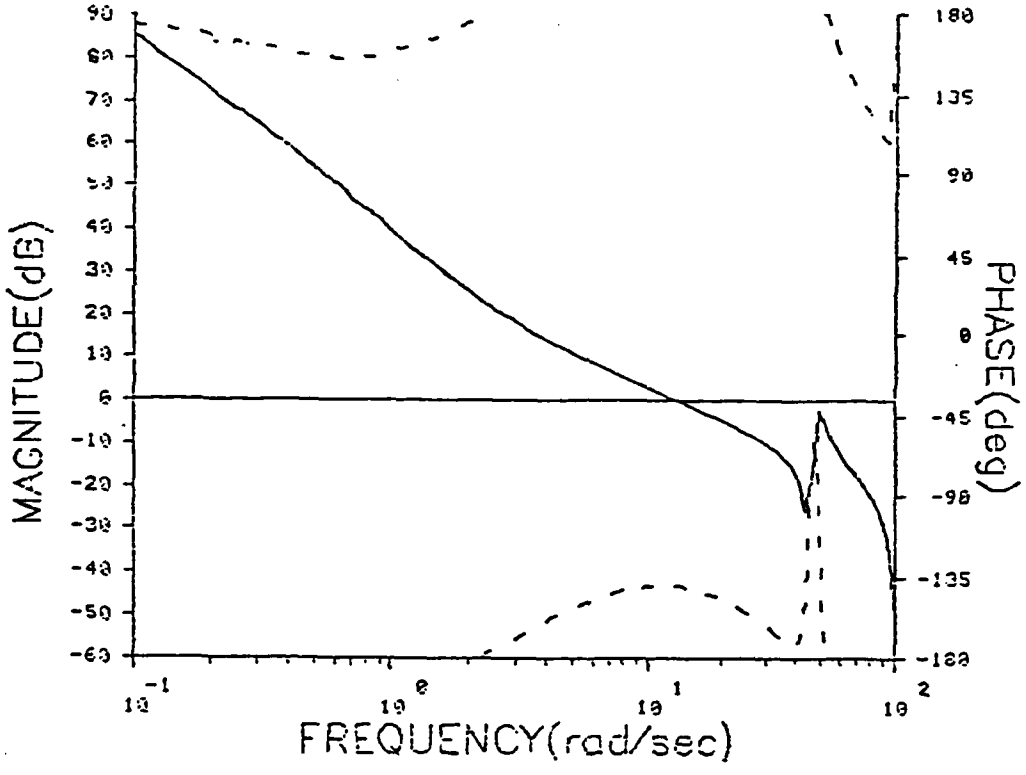

Figure 25. Loop Frequency Response with Bending Mode at 350 rad/sec.

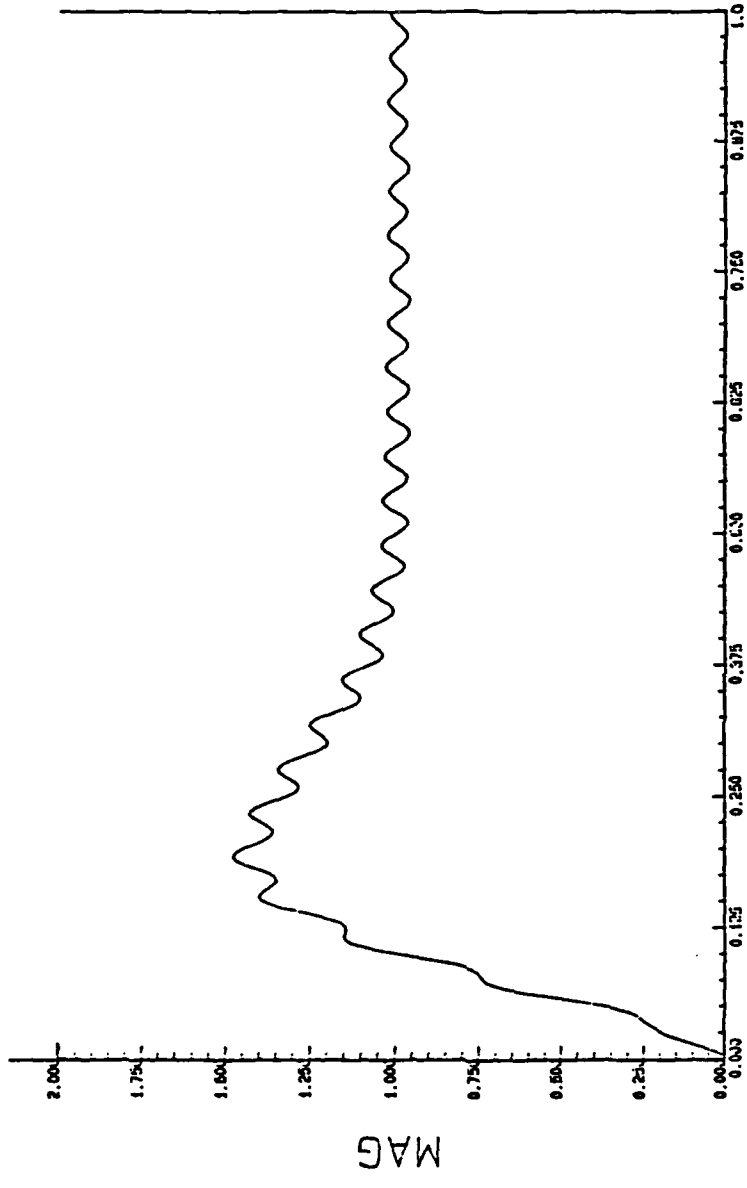

Figure 26. Step Response with Bending Mode at 150 rad/sec.

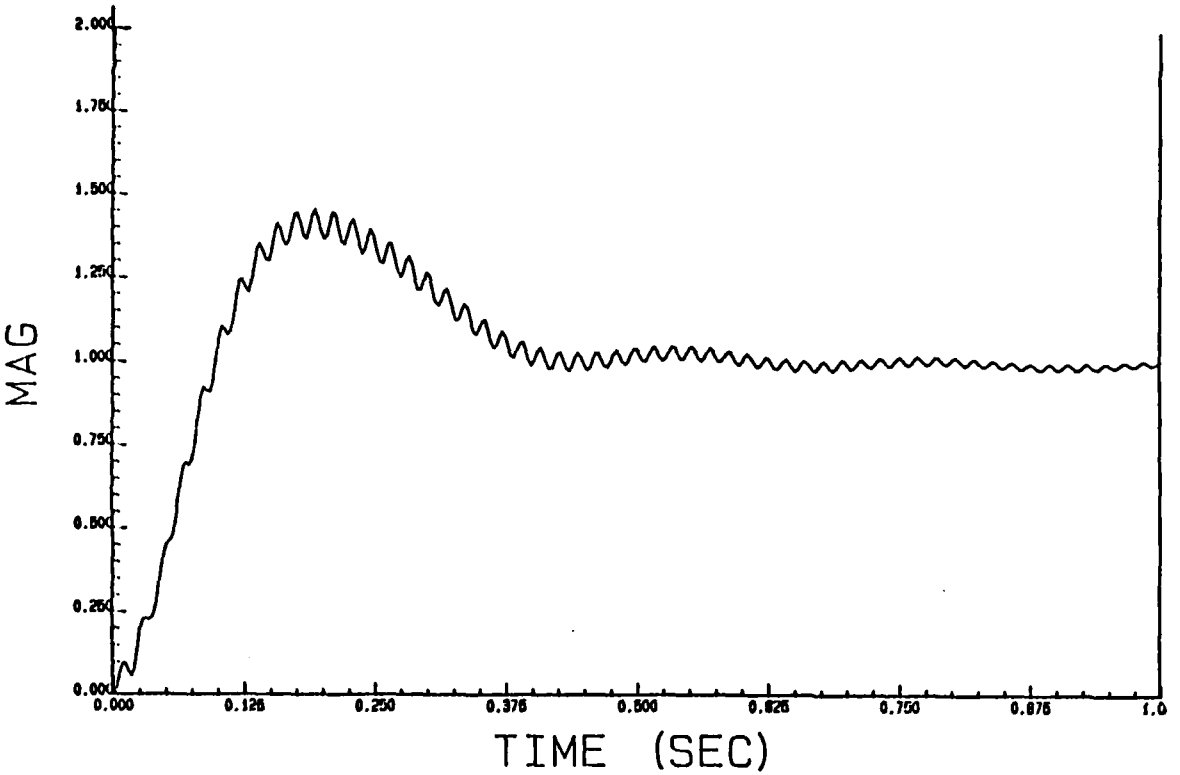

Figure 27. Step Response with Bending Mode at 350 rad/sec.

The digital pre-filter will be designed in the w plane using an average sample period equal to the uniform sample period associated with the digital compensator (.0314 sec). In the w plane the transfer function for the pre-filter is given by

$$D_2(w) = \frac{\omega_n^2}{w^2 + 2\zeta\ \omega_n\ w + \omega_n^2} \qquad (2.1.5\text{-}28)$$

where

$$\omega_n = \text{Tan}\ (\frac{\omega_n z\ T}{2}) \qquad (2.1.5\text{-}29)$$

Using the natural frequency of 88 rad/sec and the damping ratio of .3 as in the analog prefilter and using the transformation

$$w = \frac{z - 1}{z + 1} \qquad (2.1.5\text{-}30)$$

yields the z domain transfer function for the prefilter as shown below.

$$D_2(z) = \frac{27.885\ (z^2 + 2z + 1)}{32.053\ z^2 + 53.77\ z + 25.716} \qquad (2.1.5\text{-}31)$$

The following section contains the unit step responses of the two systems with both the analog and the digital prefilters in the loop separately The simulation was used extensively to experiment with both the random sample interval (T_{max} - T_{min}) and with the placement of the digital prefilter in the loop.

Case 1: 150 rad/sec vibrational mode

Fig. 28 shows the response of the system with the 150 rad/sec vibrational mode with the analog pre-filter in the loop. A comparison of this response to that shown in Fig. 26 illustrates the desirable effect of the analog prefilter with regard to reducing the effect of the alias.

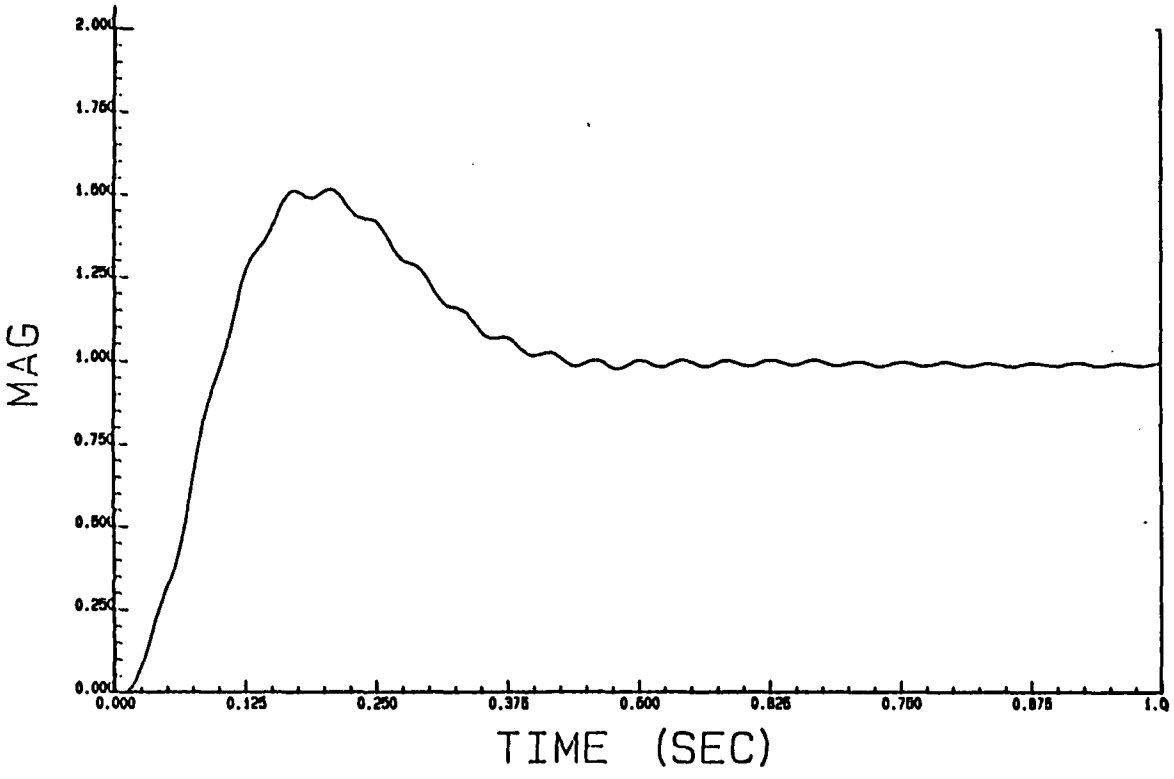

Figure 28. Step Response with Bending Mode at 150 rad/sec Including Analog Prefilter.

Figs. 29, 30 and 31 show the response of the system with the digital prefilter in the loop as shown in Fig. 21. The average sample period for the non-uniform rate sampler is the same for all three responses and is equal to the uniform sample period. For the response shown in Fig. 29 the random sample rate was varied between 190 rad/sec and 210 rad/sec. The random sample rate was varied between 150 rad/sec and 250 rad/sec for the response shown in Fig. 30. For the response shown in Fig. 31 the random sample rate was varied between 100 rad/sec and 300 rad/sec. These responses show a slight improvement in the system response as compared to the response with no prefilter if only the aliasing effects are considered. The 150 rad/sec oscillations are of smaller amplitude and settle faster in Figs. 29 and 30. However, the non-uniform rate sampling tends to degrade the system stability margins. This can be seen in all three responses by the lower frequency (approximately 16 rad/sec) oscillations which weren't present at all with the analog prefilter. These responses also show that the system stability margins get progressively worse as the range of the ramdom sampling intervals is increased.

In the responses shown in Figs. 32, 33, and 34, the sample rate was varied exactly as in Figs. 29, 30, and 31, respectively. The obvious differences in these two sets of responses are a result of changing where the non-uniform sampling rate prefilter is placed in the loop. The latter set of responses was generated with the prefilter placed before the compensator so that the random sampler is sampling the error signal. The responses in Figs. 32, 33, and 34 exhibit basically the same characteristics as their counterparts in Figs. 29, 30, and 31. Both prefilter configurations seem to reduce the alias effects as well as degrade the loop stability margins.

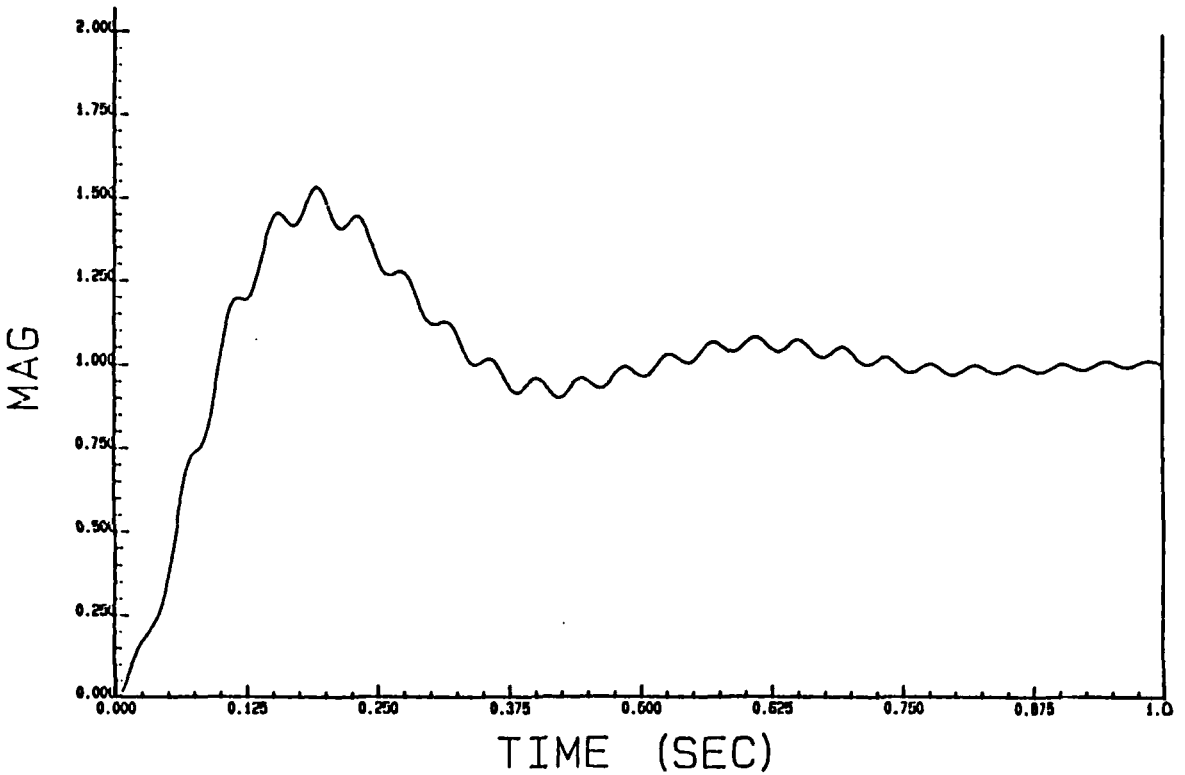

Figure 29. Step Response with Bending Mode at 150 rad/sec and Digital Prefilter (190/210).

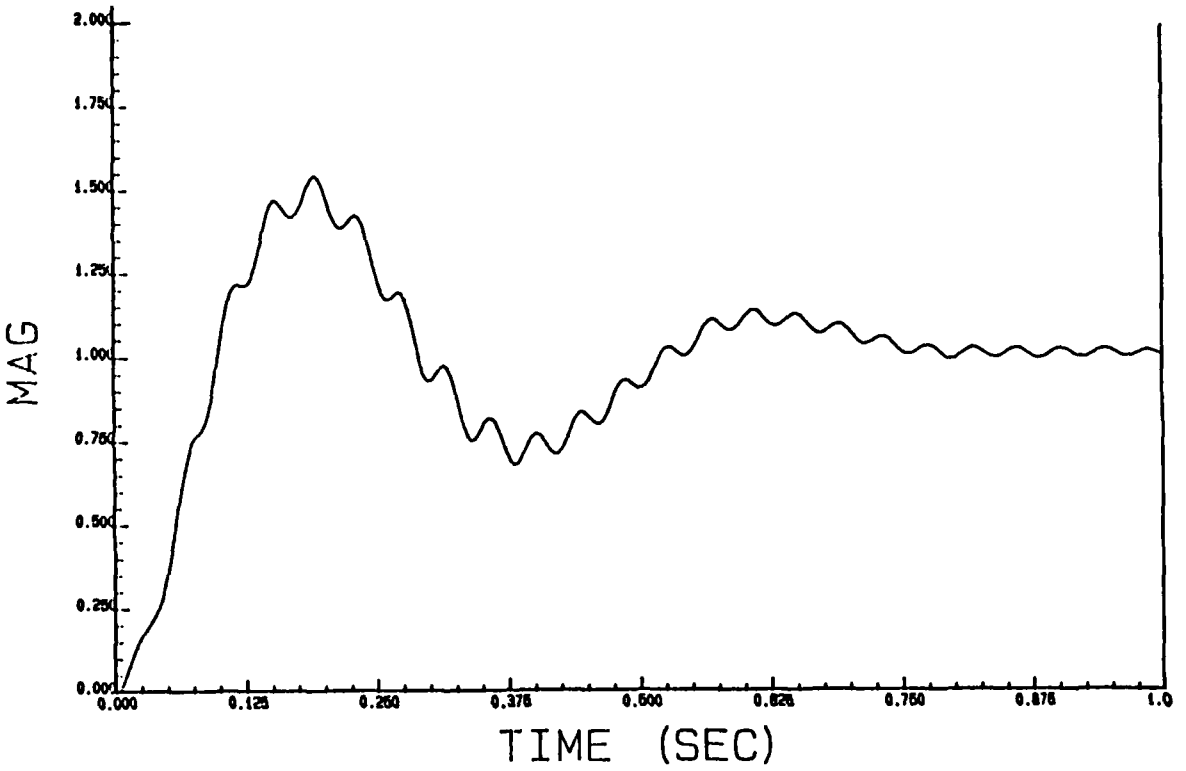

Figure 30. Step Response with Bending Mode at 150 rad/sec and Digital Prefilter (150/250).

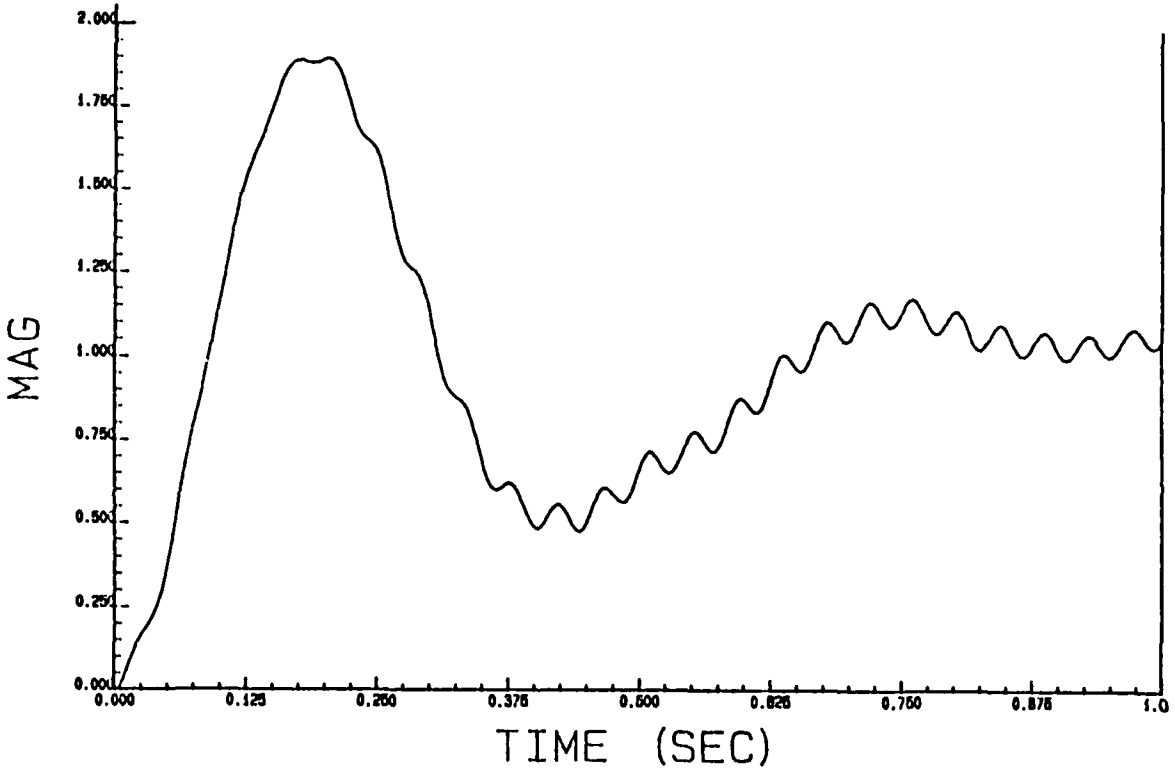

Figure 31. Step Response with Bending Mode at 150 rad/sec and Digital Prefilter (100/300).

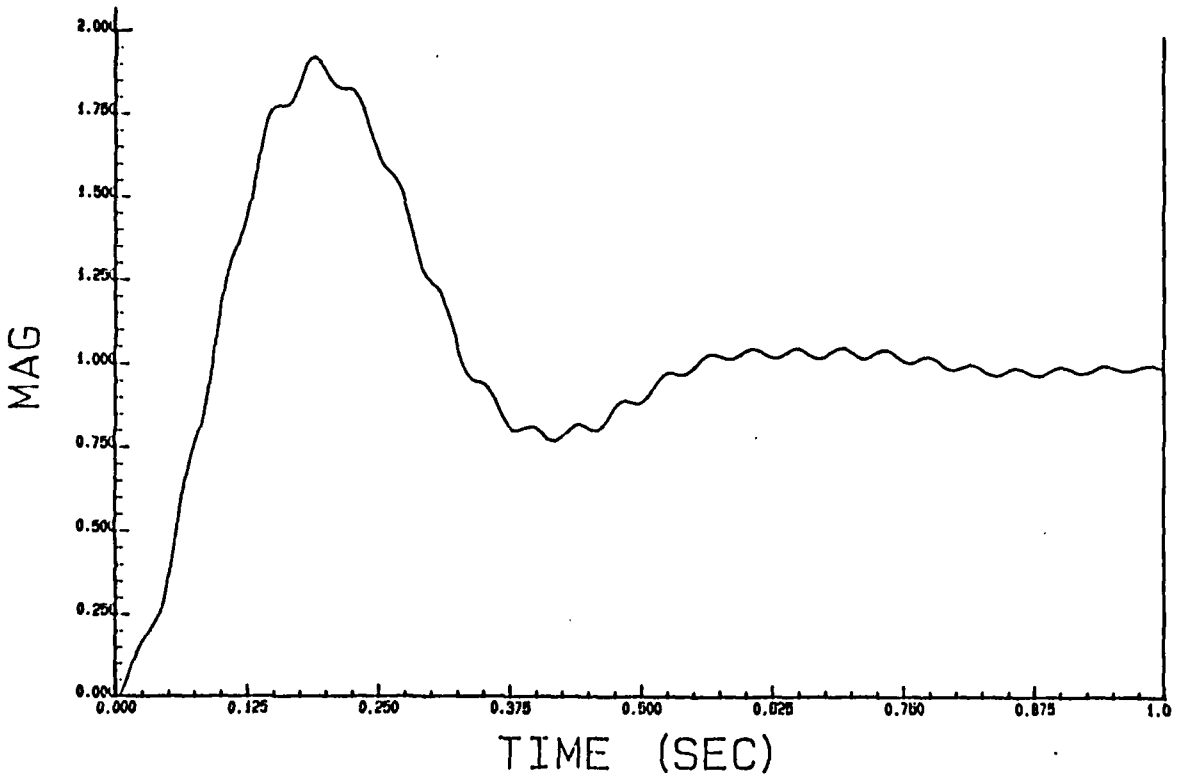

Figure 32. Step Response with Bending Mode at 150 rad/sec and Digital Prefilter in Front of Compensation (190/210).

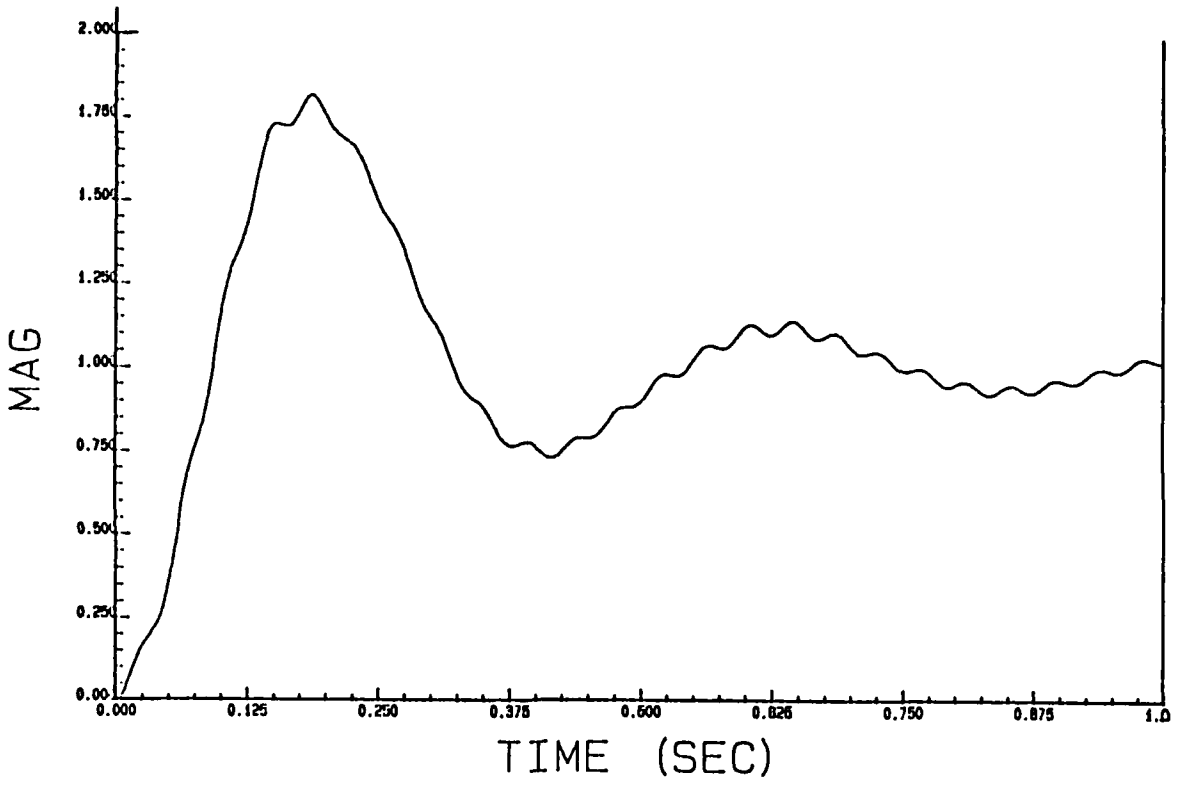

Figure 33. Step Response with Bending Mode at 150 rad/sec and Digital Prefilter in Front of Compensation (150/250).

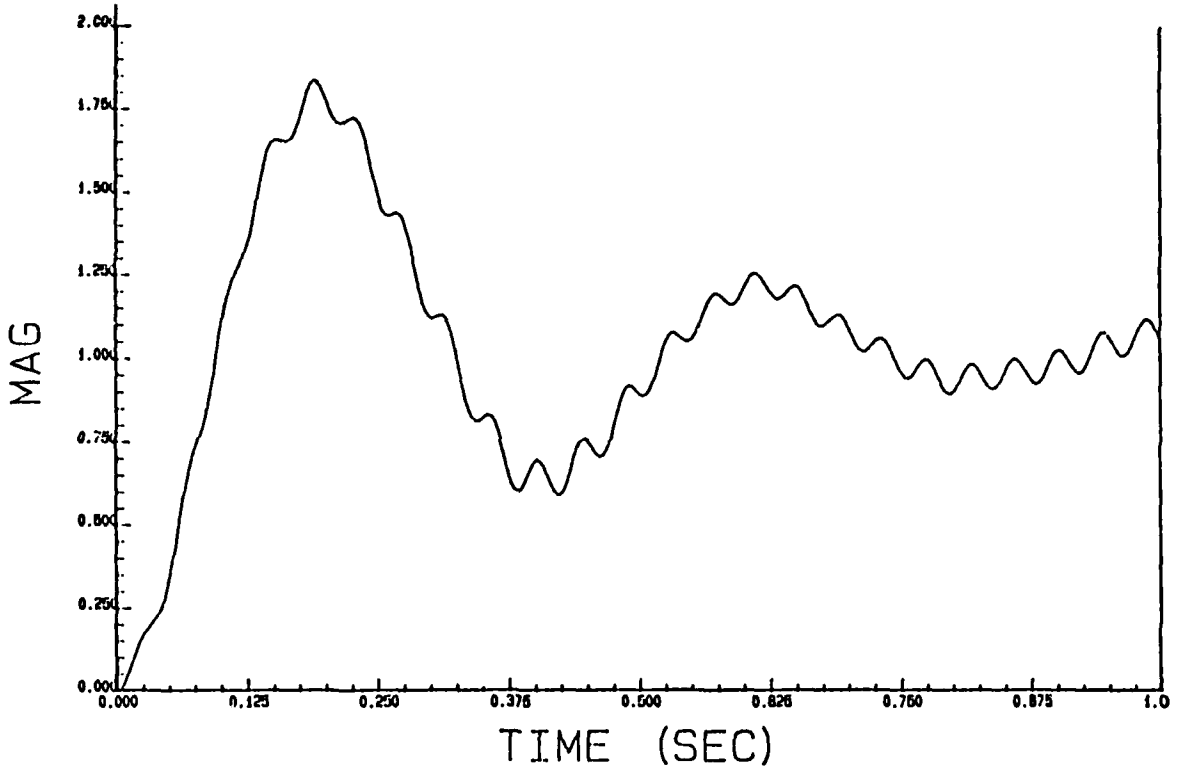

Figure 34. Step Response with Bending Mode at 150 rad/sec and Digital Prefilter in Front of Compensation (100/300).

The latter configuration tends to produce step responses with greater overshoot and faster rise time than their counterparts in the configuration of Fig. 21.

Case 2: 350 rad/sec vibrational mode

Fig. 35 shows the unit step response of the system with the 350 rad/sec vibrational mode with the analog prefilter in the loop. The analog prefilter is seen to be more effective in reducing the aliasing effects for this case because the natural frequency is higher. The stability problems due to the alias practically disappear with the analog prefilter in the loop.

Figs. 36 and 37 show responses of the system with the non-uniform sampling rate prefilter in the loop as shown in Fig. 21. In the response shown in Fig. 36 the sample rate was varied between 190 rad/sec and 210 rad/sec. The sample rate was varied between 150 rad/sec and 250 rad/sec in the response shown in Fig. 21. The average sample rate for the prefilter is, therefore, the same as the uniform sample rate for these responses. These responses exhibit most of the same characteristics that were present in the responses for Case 1. Again, it is evident that the prefilter tends to degrade the system stability margins, an effect that worsens with increasing range of the sampling intervals. The system responses with the prefilter moved ahead of the compensator follow the same basic pattern as for those shown for Case 1 and are, therefore, omitted.

Conclusions. Two alternatives to analog prefiltering were presented in the preceding sections. A comparison of their respective advantages and disadvantages is included in the following discussion. Future research directions are also recommended.

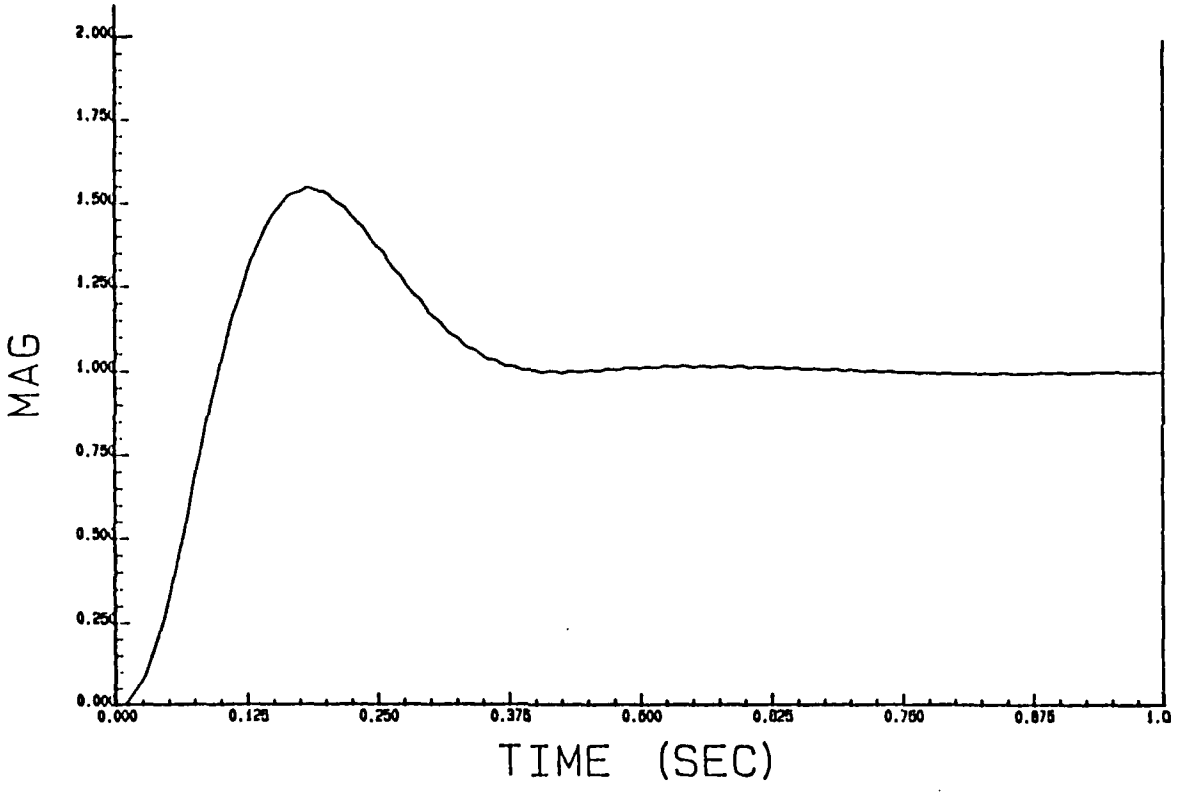

Figure 35. Step Response with Bending Mode at 350 rad/sec Including Analog Prefilter.

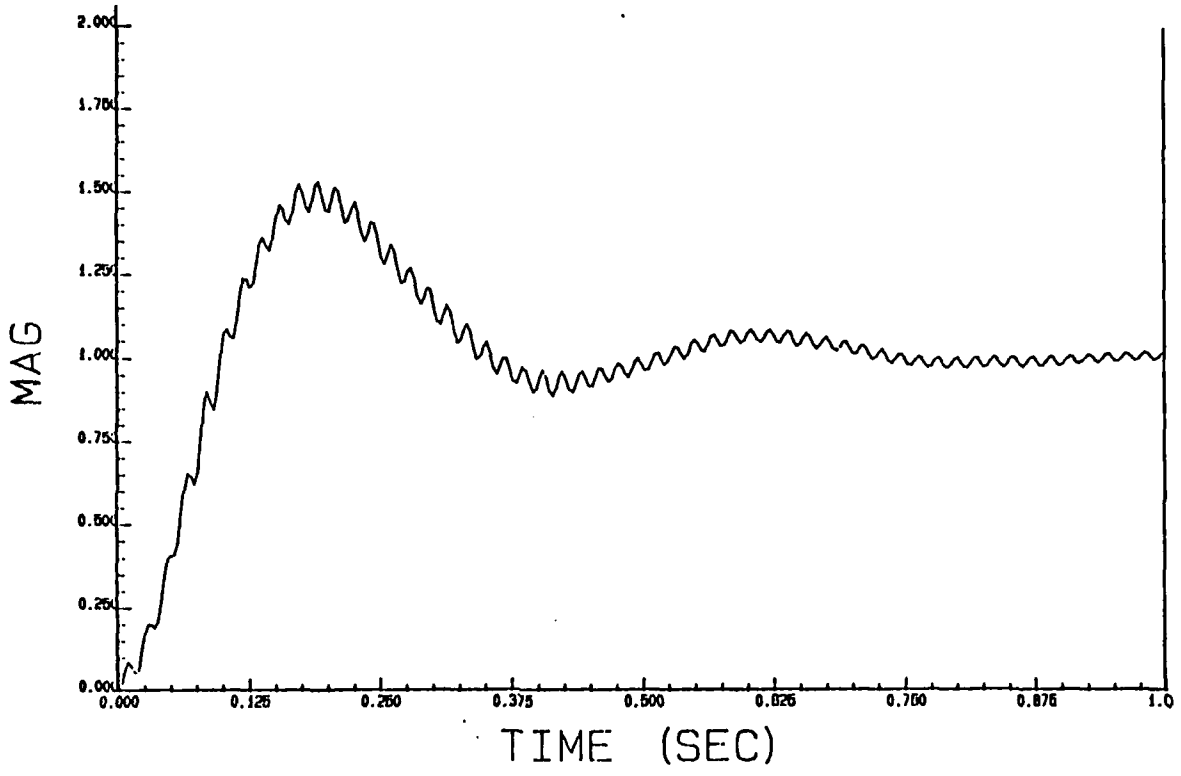

Figure 36. Step Response with Bending Mode at 350 rad/sec and Digital Prefilter (190/210).

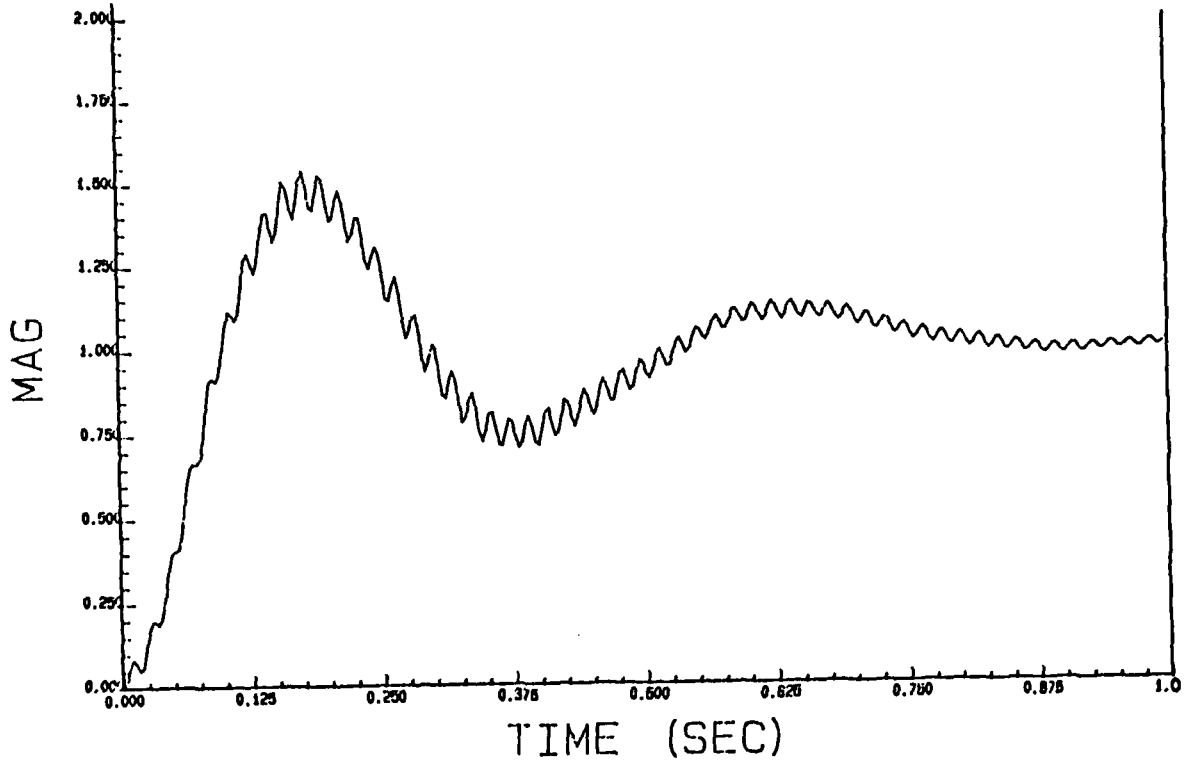

Figure 37. Step Response with Bending Mode at 350 rad/sec and Digital Prefilter (150/250).

The first of the alternatives to analog prefiltering is fast uniform rate digital prefiltering. While no theoretical stumbling blocks to the implementation of such a filter exist, there are two practical considerations with which the system designer must contend. The first consideration is that of whether appropriate fast samples are available. Second, the designer should realize that the implementation of the fast rate prefilter will probably entail the use of dedicated hardware and, hence, a higher cost.

The second alternative to analog prefiltering is the non-uniform rate prefilter. While no exact theory exists to provide for such a filter design, the results of Section III at least show that the non-uniform rate sampling process minimizes the effects of aliasing. However, in Section IV it was shown that the use of a corresponding digital prefilter based on an average sample rate degrades the system stability margins. In spite of these problems, future research into the prefilter design is indicated. Several possibilities for research exist. First, it may be possible to design compensation with the non-uniform rate sampler, precluding the need for a prefilter since aliases are not introduced. Second, a different non-uniform rate sampling scheme might yield better prefilter performance. Indeed, Leneman's work with "jitter rate" sampling [5] appears especially promising.

2.1.6 Investigation of System Stability and Performance

This section includes discussion of the system performance of the ASCOT-I controller coupled with the ASCOT-I model as described in Section 2.1.4. The performance is analyzed with respect to position loop bandwidth, random disturbance rejection, and deterministic disturbance rejection. The disturbance rejection studies use the line of sight (LOS) criteria developed under Section 2.2.3. The disturbance inputs are described in Section 2.1.2.

Position Loop Bandwidth. The position loop bandwidth is of interest as an indication of system performance in terms of response to pointing command inputs (such as a slew command). Figs. 38, 39, and 40 display the closed loop frequency responses from commanded position input to measured faceplate position output for the x, y, and z-axes, respectively. The x-axis bandwidth is about 0.8 rad/sec and the y-axis bandwidth is about 0.9 rad/sec. The y-axis bandwidth is wider because of inherent differences in the gimbal positions; however, it exhibits greater peaking near the bandwidth. The z-axis response of Fig. 40 is the most well behaved of the three; indicative of the benign nature of the torsional behavior. The z-axis bandwidth is roughly 3.0 rad/sec.

Random Noise Disturbance Suppression. The random noise suppression results herein were generated with the frequency domain model of the structure which was used in conducting the design. The Power Spectral Density (PSD) of the random force disturbance applied to the structure is given in Section 2.1.2. With the coordinate system and input/output definitions chosen disturbance force in the y-direction (Fy) generates error in x-axis LOS (LOSx) and vice versa. Cross-axis disturbance is precluded by the decoupled nature of the system.

The PSD of the LOS error in the x-axis with disturbance applied in the y-direction and all control loops open is given in Fig. 41. Fig. 42 displays the same quantity with all control loops closed. Comparison of these plots shows a definite improvement in disturbance rejection with the control system included, especially at the modal peaks. Quantitatively, the RMS error in the open loop case is 1.5×10^{-4} rad.; an improvement of a factor of about 4.

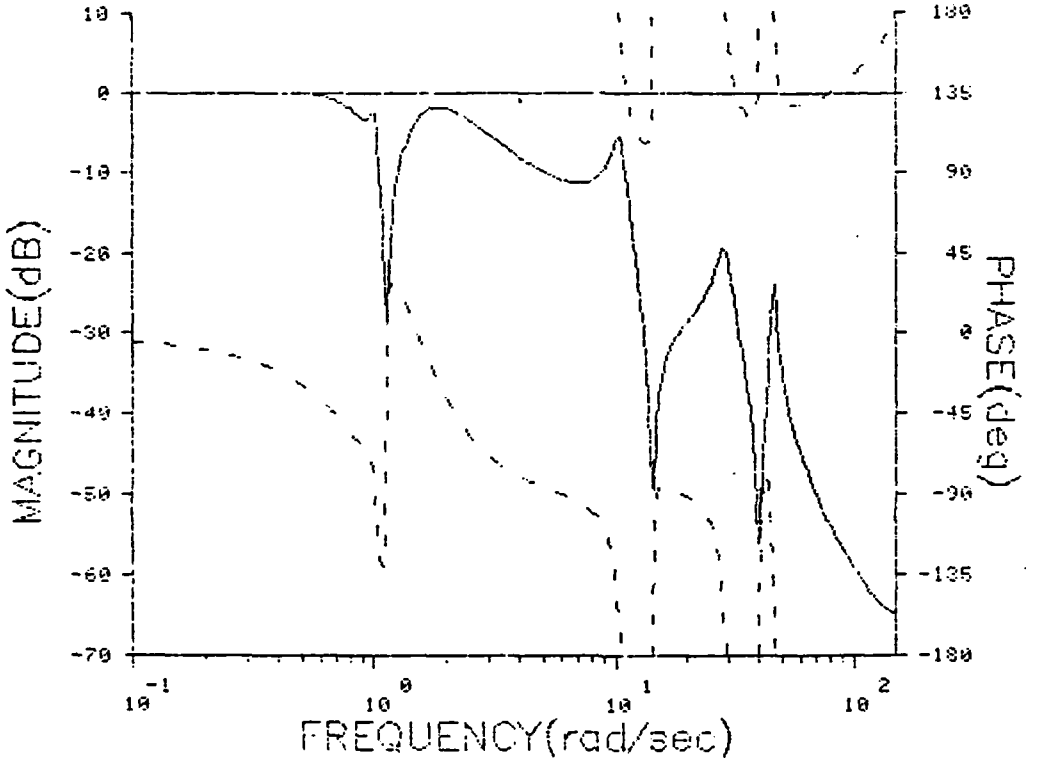

Figure 38. Closed X-Axis Position Loop Frequency Response (ASCOT-I).

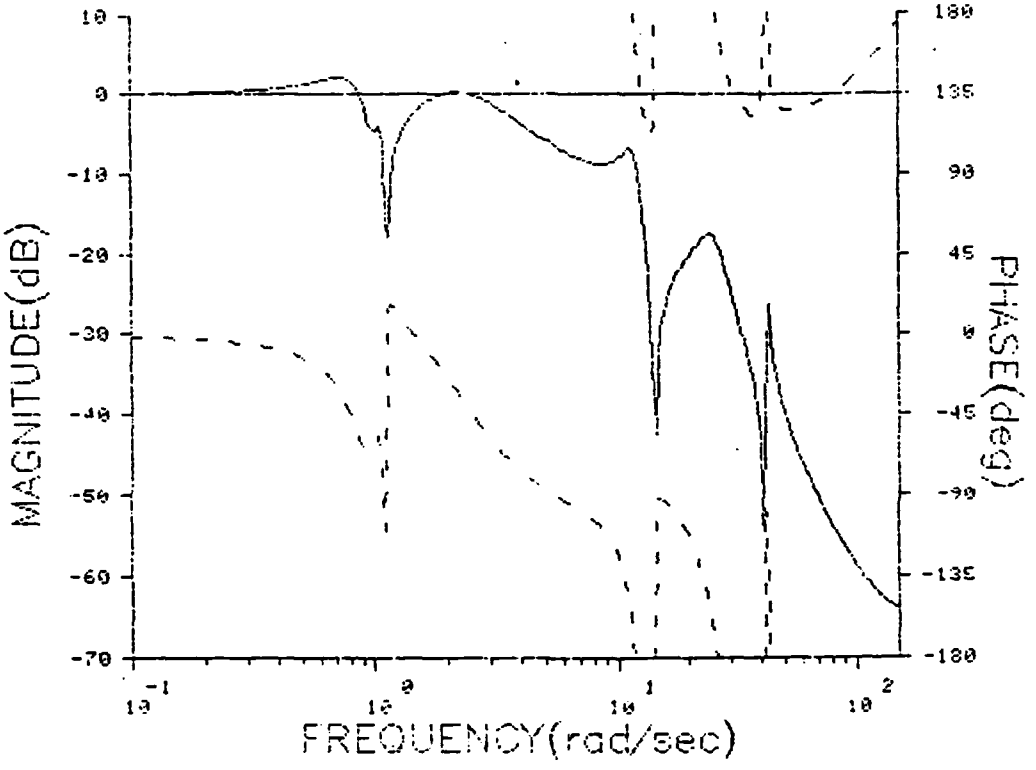

Figure 39. Closed Y-Axis Position Loop Frequency Response (ASCOT-I).

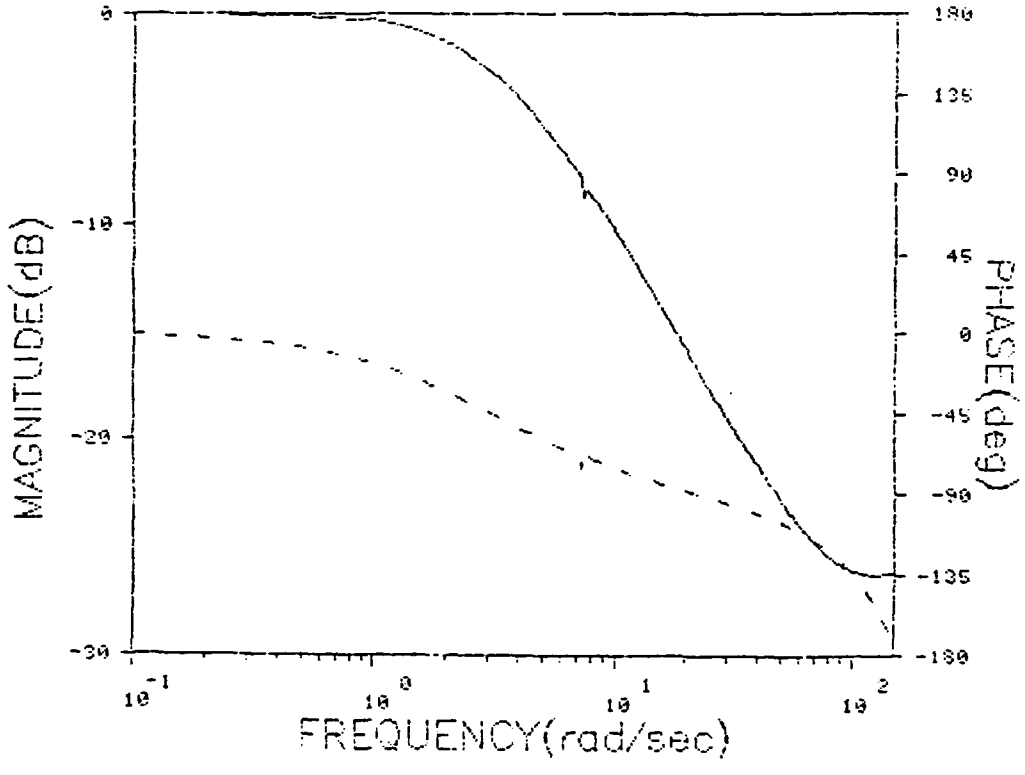

Figure 40. Closed Z-Axis Position Loop Frequency Response (ASCOT-I).

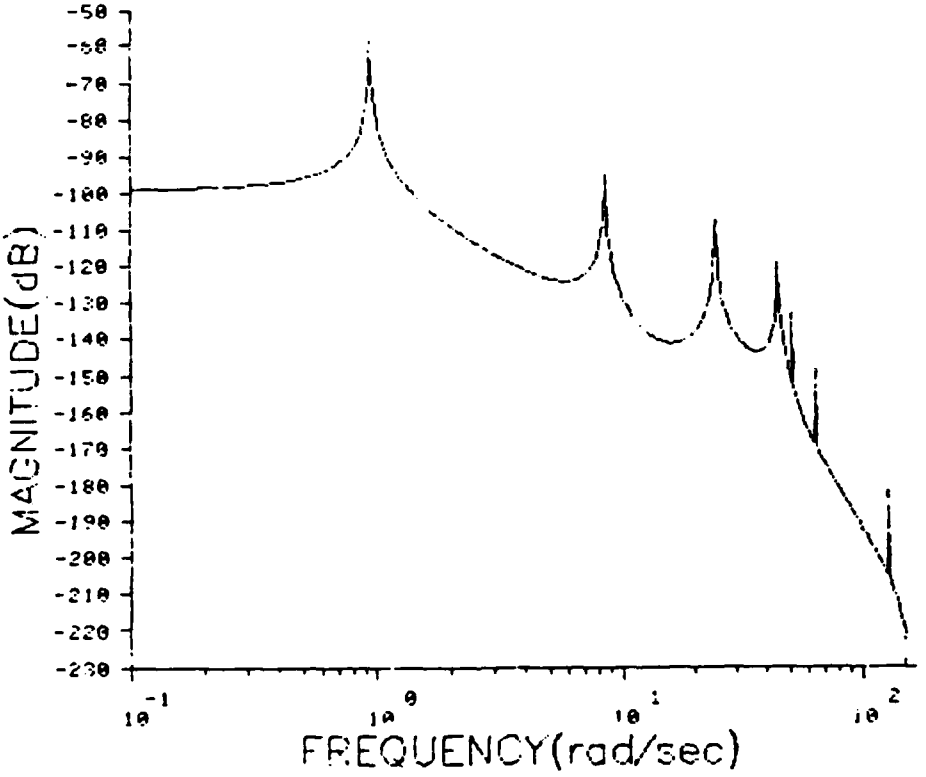

Figure 41. PSD of X-Axis LOS Open Loop Response to a Random Disturbance Y (ASCOT-I).

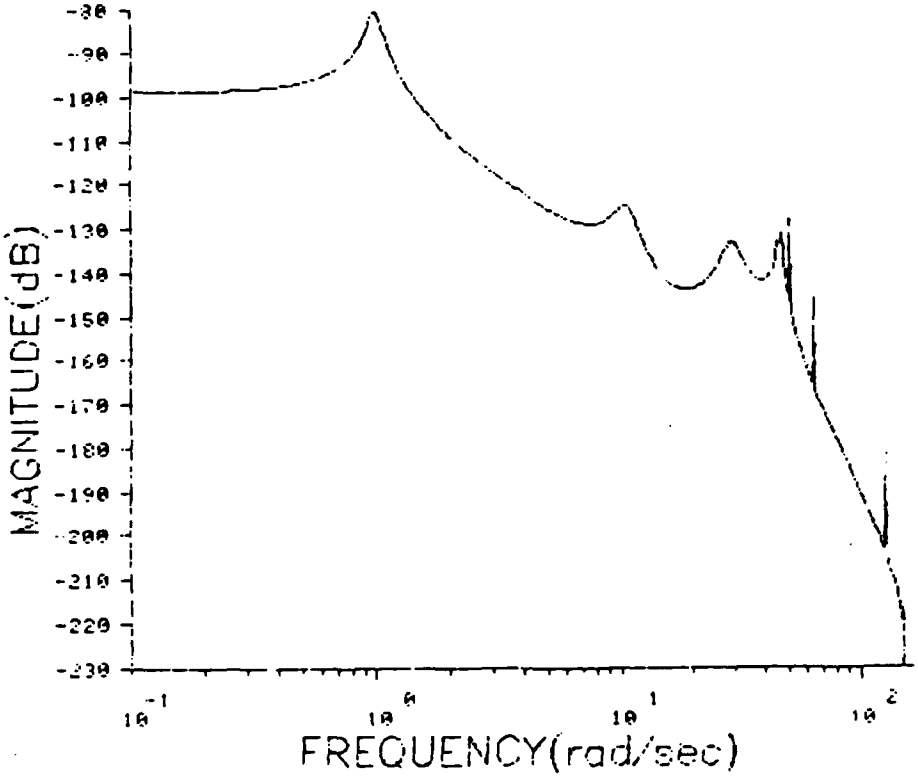

Figure 42. PSD of X-Axis LOS Closed Loop Response to a Random Disturbance in Y (ASCOT-I).

Figures 43 and 44 display the similar quantity for the other axis, i.e., PSD of LOS_y with a disturbance in the x-direction, both open and closed loop. The results are similar also, with an open loop LOS_y RMS error of 2.0×10^{-4} rad. and a closed loop value of $.46 \times 10^{-4}$ rad.; again, a factor of about 4 improvement.

Deterministic Disturbance Suppression. The LOS responses to the deterministic disturbances were computed using a simulation of the LSS/GTV facility test scenario. For this reason the disturbance inputs are applied at some finite "ready" time greater than zero. This simulation models the structure continuously using a forth order runge-kutta integration scheme. It models the digital control law discretely at the sample times using recurrence algorithms derived from the z-transforms of the compensators. The structural model used to produce the following results included 12 modes and gravity effects just as the design model.

Fig. 45 shows LOS_x versus time for a crew motion disturbance input in the y-direction for both open and closed loop cases. The crew motion disturbance excites the bending of the structure very little as is evidenced by the domination of LOS_x by the pendulum behavior. Similarly, Figure 46 shows that LOS_y due to crew motion disturbance in the x-direction is also dominated by the pendulum mode. In both cases, the closed loop LOS curve shows the increased damping and accompanying disturbance rejection facilitated by the closed loop control. Figure 47 presents the overall pointing error of Equation 2-3 for both open and closed loop in the face of crew motion disturbance in both the x and y directions simultaneously. Again, the closed loop response shows improved damping and disturbance rejection.

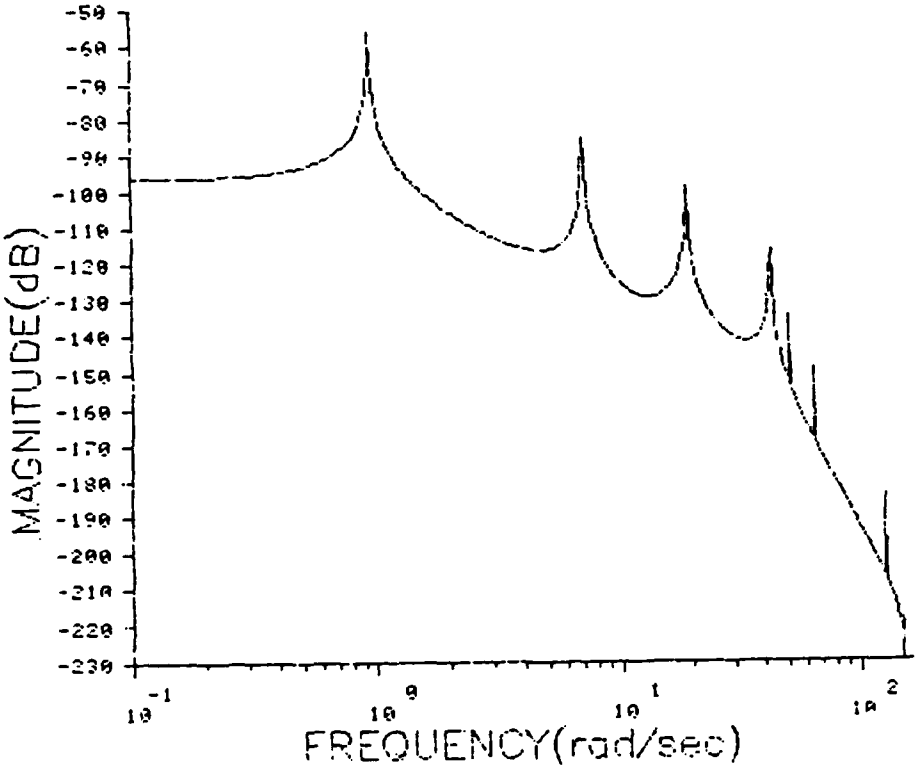

Figure 43. PSD of Y-Axis LOS Open Loop Response to a Random Disturbance in Y (ASCOT-I).

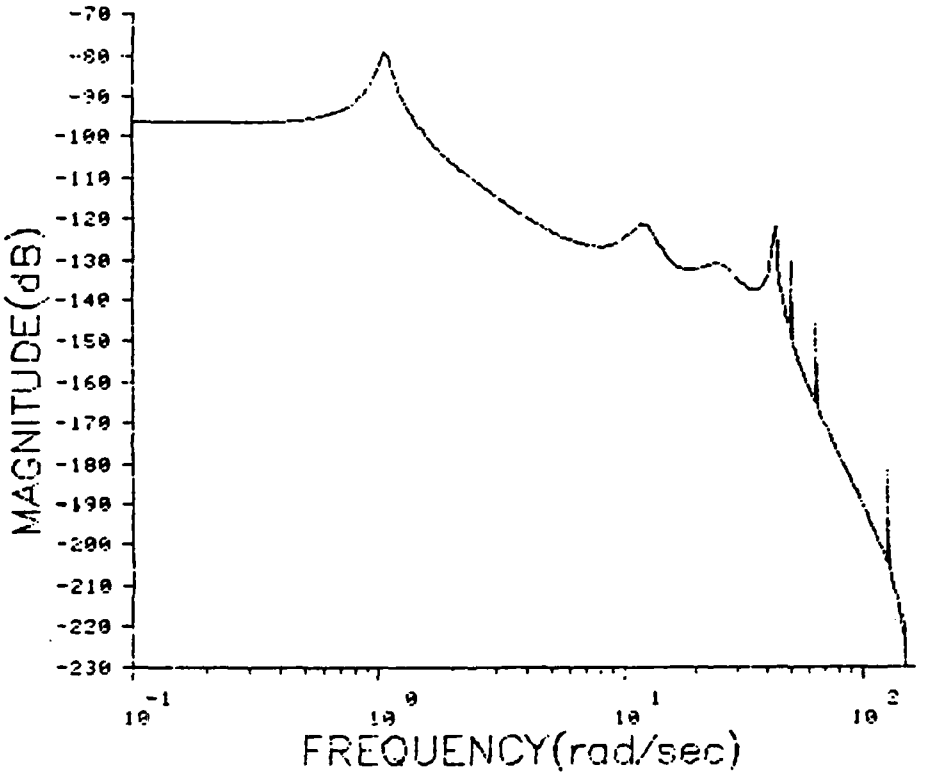

Figure 44. PSD of Y-Axis LOS Closed Loop Response to a Random Disturbance in Y (ASCOT-I).

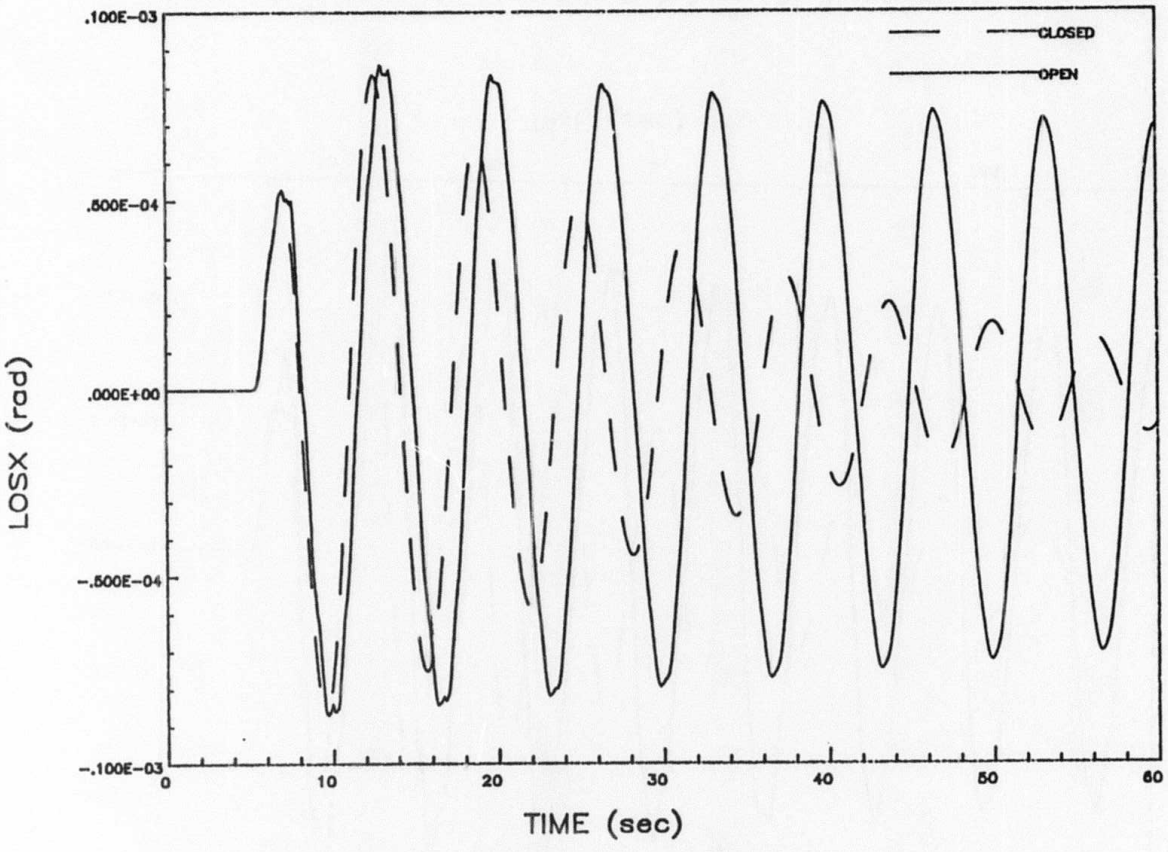

Figure 45. Open and Closed Loop X-Axis LOS Responses to Crew Motion Disturbance in Y (ASCOT-I).

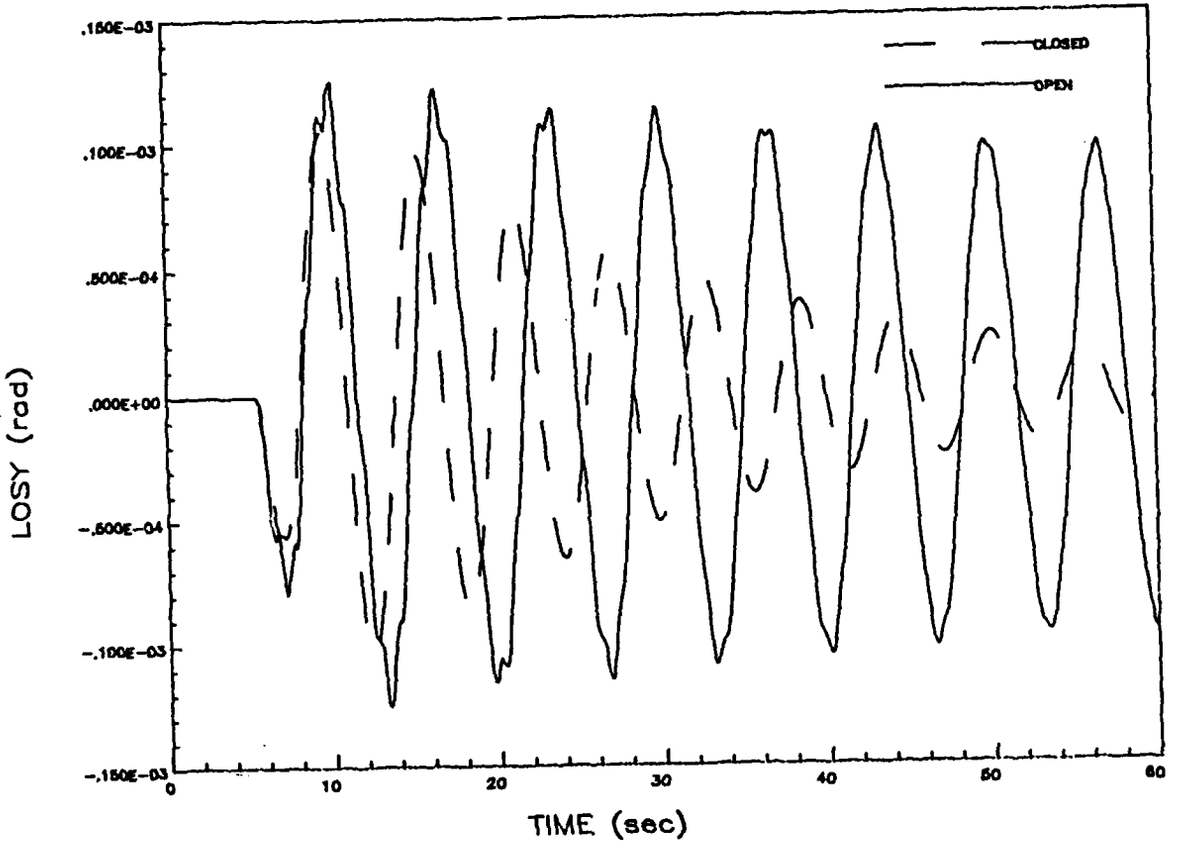

Figure 46. Open and Closed Loop Y-Axis LOS Responses to Crew Motion Disturbance in X (ASCOT-I).

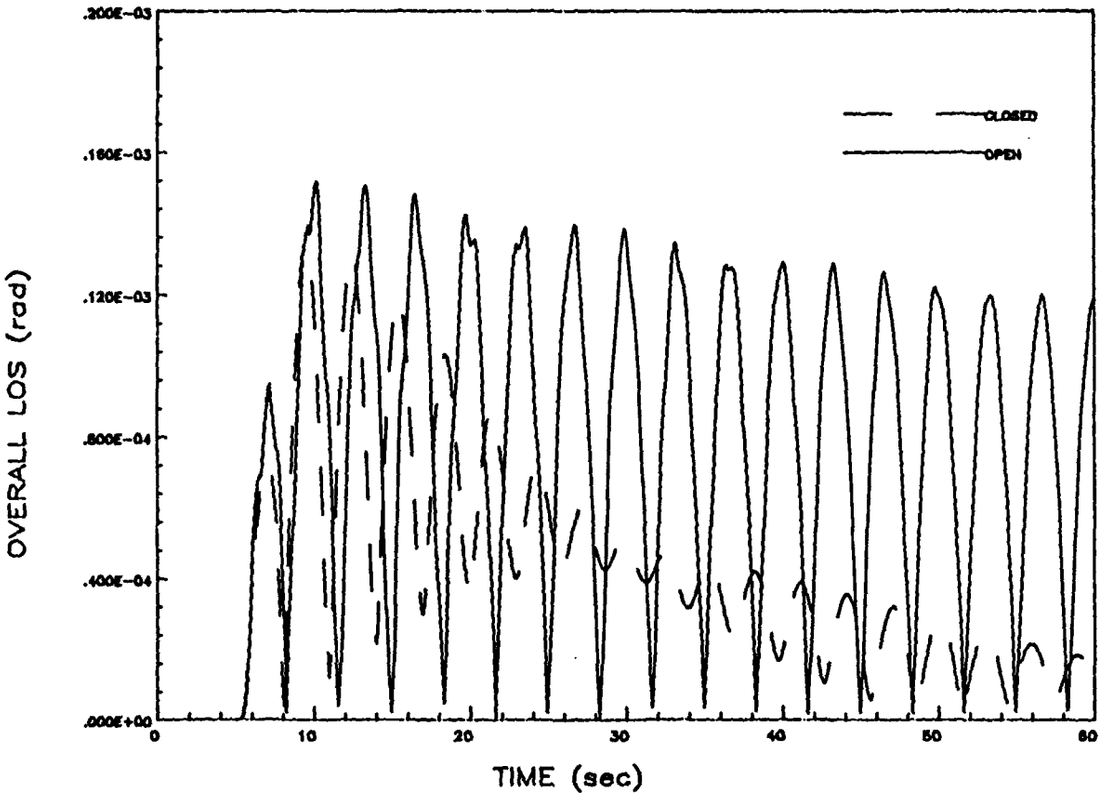

Figure 47. Open and Closed Loop Total Error Responses to Crew Motion Disturbance in Both X and Y (ASCOT-I).

The open loop LOS_x error response to the RCS thruster firing disturbance in the y-direction of Fig. 48 indicates that the RCS disturbance excites the bending of the structure considerably more than the crew motion disturbance. The lack of high frequency characteristics in the accompanying closed loop response indicates the excellent damping of the bending characteristics. This response is, again, dominated by the pendulum behavior. The LOS_y results of Fig. 49 show the damping of the bending modes even more dramatically than Fig. 48. Finally, the overall pointing error response of Fig. 50 due to the RCS disturbance includes no surprise in its performance improvement.

Conclusions. The ASCOT-I controller in conjunction with the ASCOT-I structural model has been shown to exhibit considerable improvement in disturbance rejection over the open loop structural behavior. The improvement in rejection of random disturbances was shown to be roughly a factor of 4 in each axis. The LOS responses to deterministic disturbances indicated the increased damping of both the bending behavior of the structure and the pendulum behavior.

2.1.7 Evaluation of which spacecraft parameters affect the controller performance

In order to analytically model complex spacecraft, a number of simplifying assumptions must be employed in the formulation of the equations of motion. Typically, some of these assumptions involve the characterization of the mass and stiffness properties of the structure, which in turn directly effect the spacecraft's natural frequencies and modeshapes. Additionally, the characteristics of any actuators and transducers must be modeled in some fashion such that their dynamics are properly accounted for in the system dynamical equations.

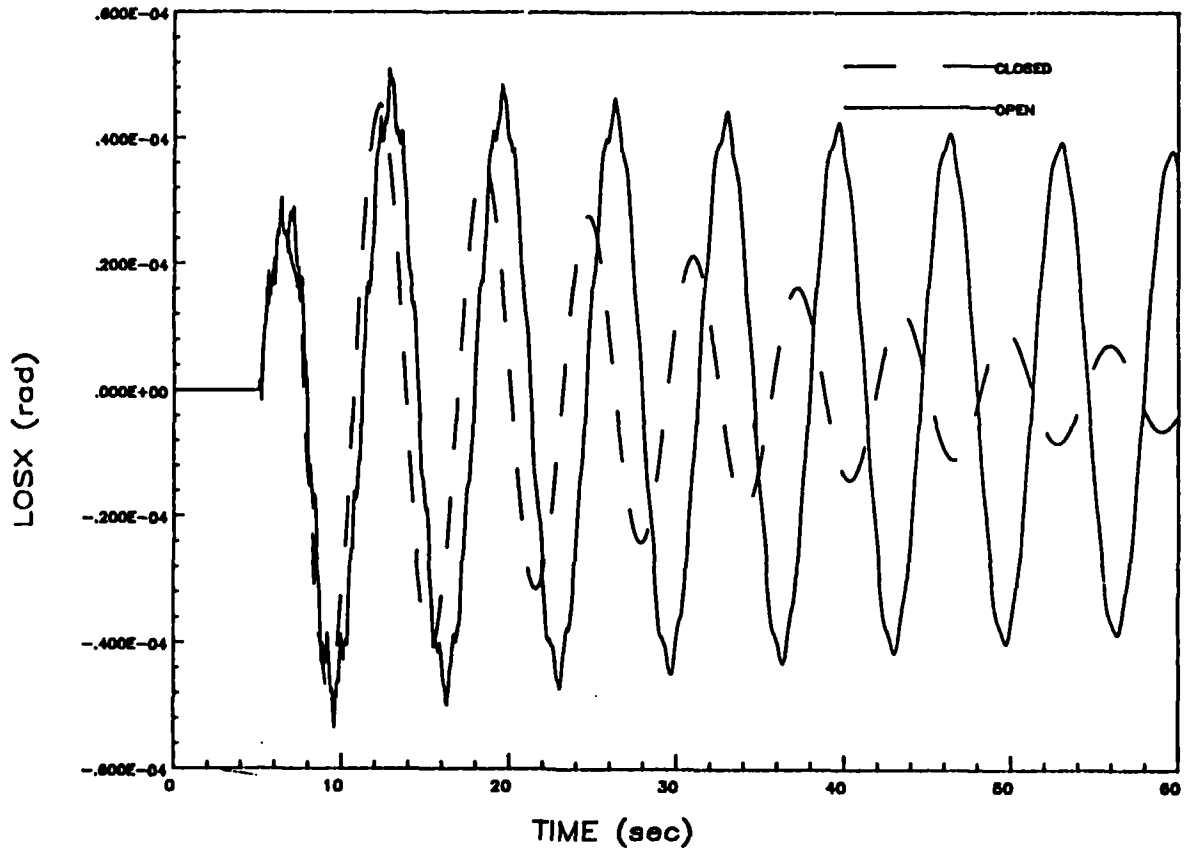

Figure 48. Open and Closed Loop X-Axis LOS Responses to RCS Disturbance in X (ASCOT-I).

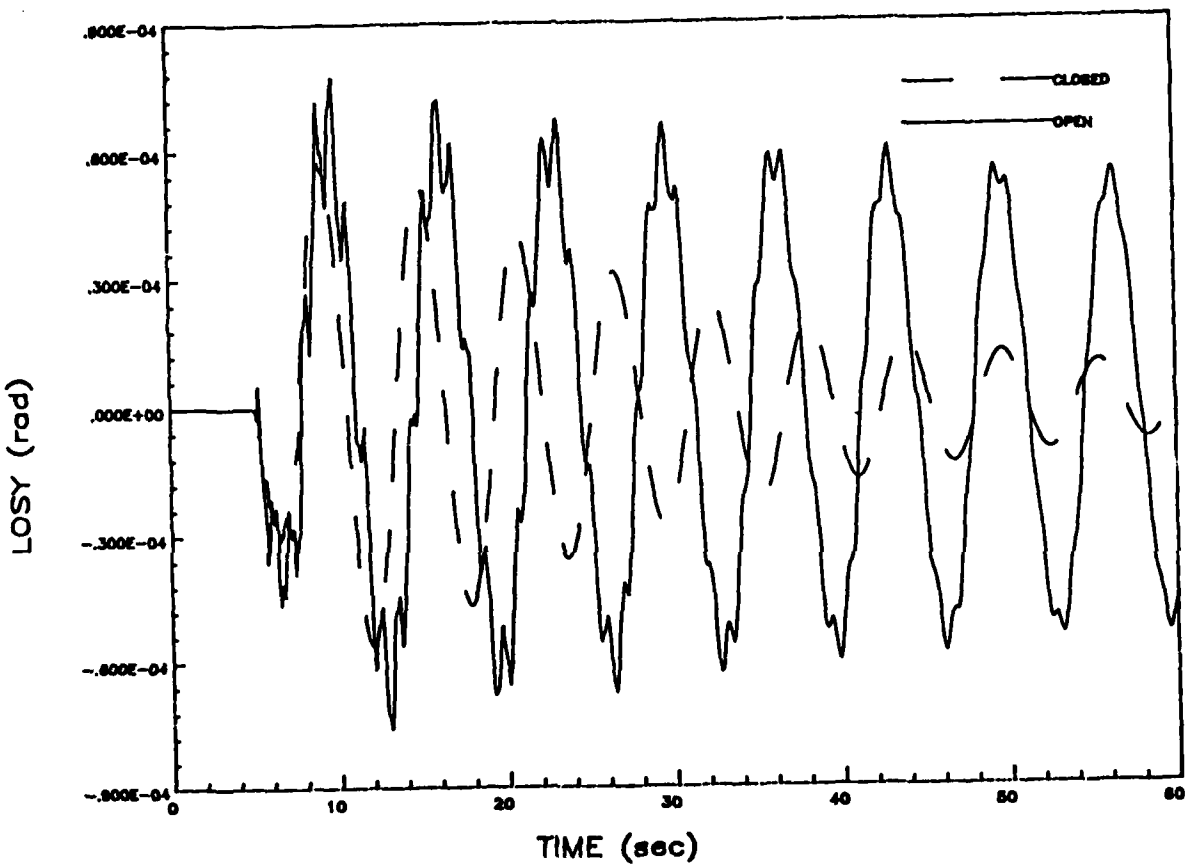

Figure 49. Open and Closed Loop Y-Axis LOS Responses to RCS Disturbance in X (ASCOT-I).

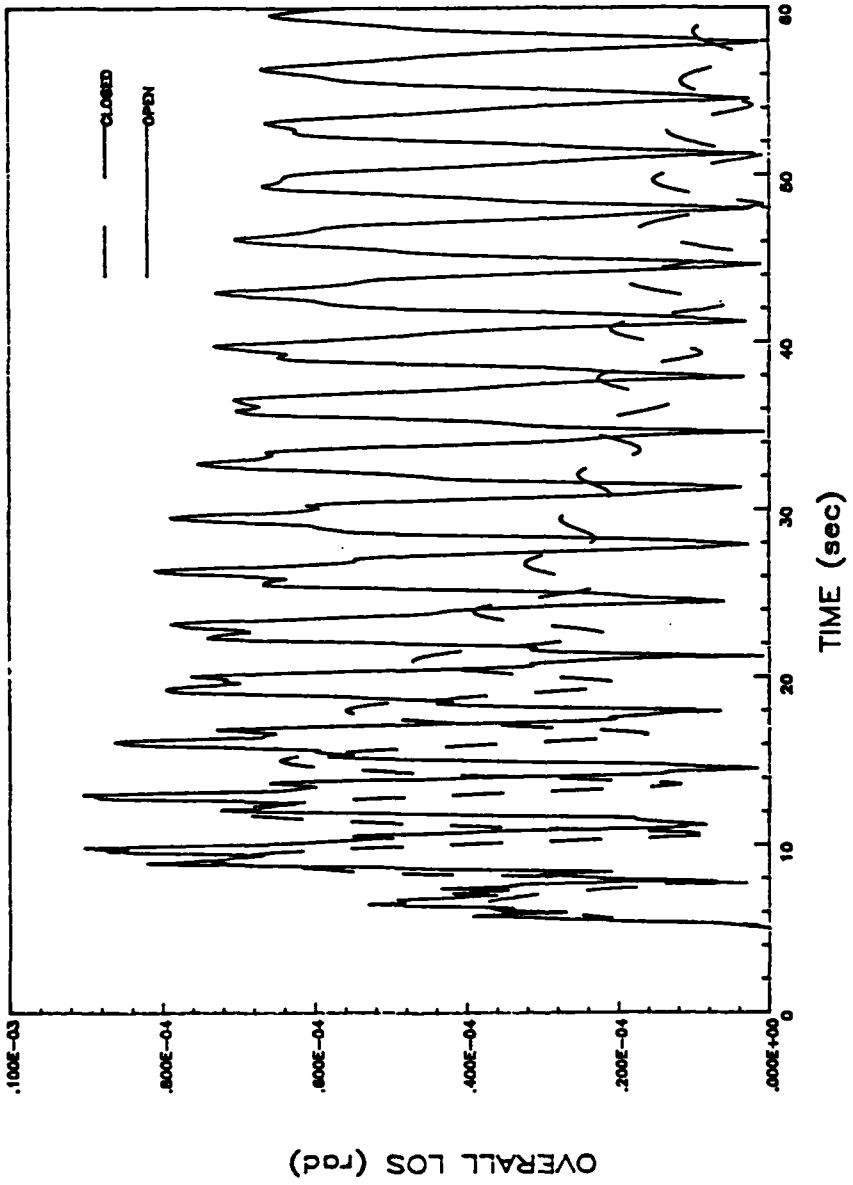

Figure 50. Open and Closed Loop Total Error Responses to RCS Disturbance in Both X and Y (ASCOT-I).

As far as the RTOP system (See Section 2.2.5) is concerned, the exact orientation of the tip instrument package is considered to be less well known than most other parameters. To study the effects of a change in orientation of the tip package, a model was prepared with the tip package skewed off the nominal position by a 30° angular displacement about an i + j + k vector.

This perturbed model was then used to conduct a robustness study on the rtop controller design described in Section 2.2.5. The robustness study is delineated in Section 2.1.8.

2.1.8 Investigation of System Robustness

The RTOP controller robustness study is very straightforward. The RTOP controller described in Section 2.2.5 is coupled with the perturbed model of Section 2.1.7 and the resulting closed loop system is studied.

The perturbed model does not exhibit significantly different in-axis behavior than that of the RTOP model. That is to say, the transfer characteristics upon which the compensation was designed do not change significantly, and as a reslut the system stability margins do not change.

However, the cross-axis characteristics do change significantly between the RTOP and perturbed models. Fig. 51 displays the open loop transfer characteristic from torque in y (T_y) to faceplate angular rate in x ($\dot{\Theta}_x^*$) for the RTOP model. The same quantity for the perturbed model is shown in Fig. 52. Clearly, the perturbed model exhibits greater cross-axis coupling, and the robustness studies show that the RTOP controller is robust to these changes. This is largely due to the fact that the controller is not coupled between axes and makes no attempt to control one axis with signals measured from another. ICAT allows the designer to easily impose such conditions on the control law at the outset of the design process.

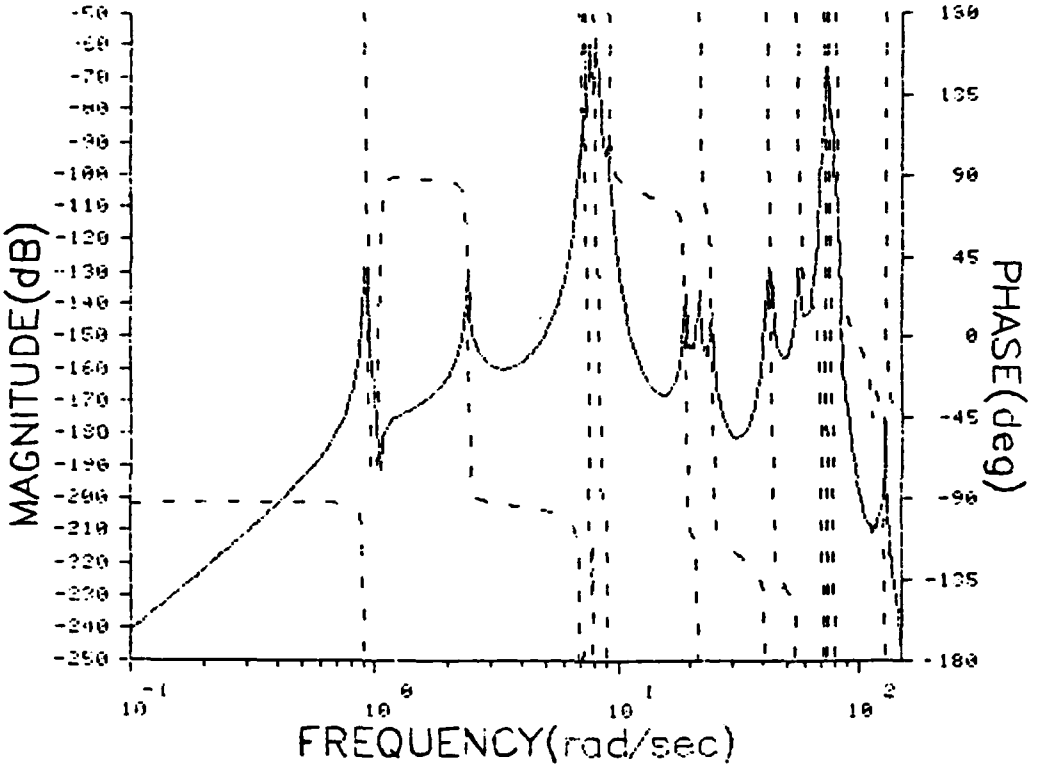

Figure 51. Cross Axis Frequency Response from Torque in Y to Faceplate Angle in X for the RTOP Model.

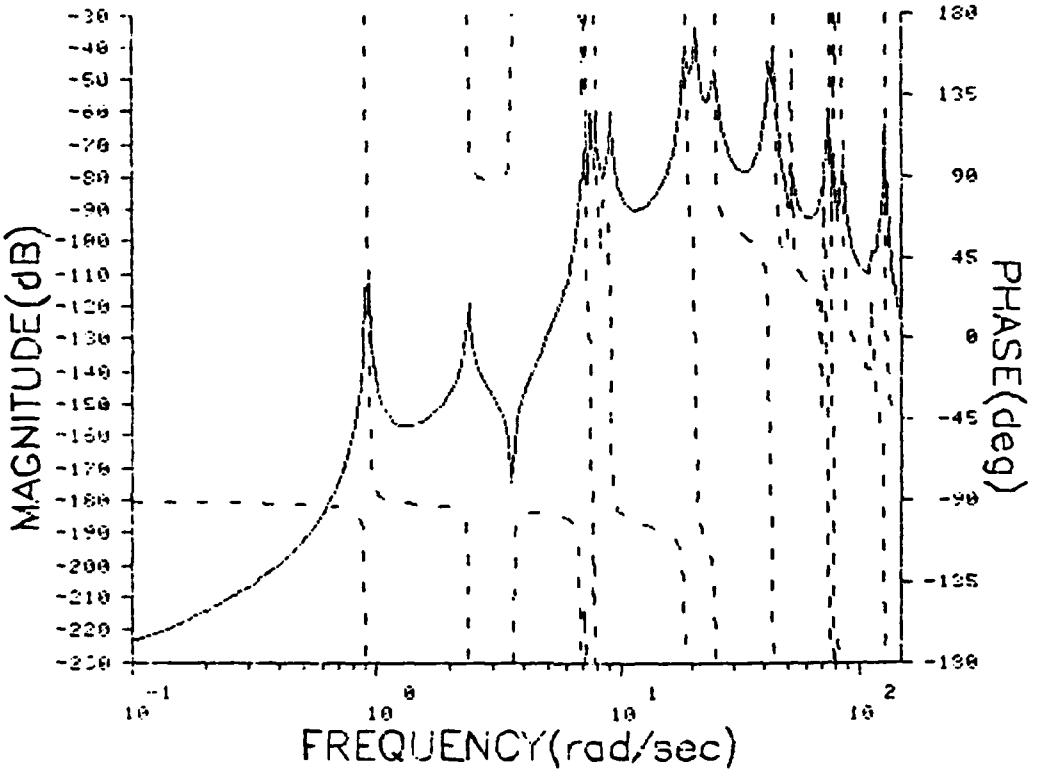

Figure 52. Cross Axis Frequency Response from Torque in Y to Faceplate Angle in X for the Robustness Model.

2.2 TASK 2 - TEST PLANNING AND COORDINATION, TEST SUPPORT AND CONTROL Technique Selection

2.2.1 Formulation of Technical/Management Program Development Plan

The Technical/Management Program Development Plan was delivered mid term of the contract period as a stand-alone document. It reviews the state of the ASCOT effort in its 6th month and delineates the remainder of the effort as described in this report.

2.2.2 Modification of Ascot-I to NASA Structural Test Article

This section provides a description of the ASCOT-I model, its origin, and the motivations behind using it as a test problem for S2D2.

Introduction. The ASCOT-I model is derived directly from the first test fixture installed in the LSS Ground Test Verification (LSS/GTV) facility at Marshall Space Flight Center (MSFC). This facility provides a test-bed for LSS type structures and related control hardware and software in both open and closed loop operations. This system and resulting structural model is thought to be a suitable test-bed for the S2D2 candidate, ICAT, because of the realism of the system. Unlike past efforts where control strategies were tested on LSS models derived from fictitious LSS, the ASCOT-I model, although much simpler, provides a model of an actual structure which has been verified with modal testing. Also, reasonable constraints on sensor and actuator performance and sample rate are imposed.

LSS/GTV Facility Description. The LSS/GTV facility and test fixture are described by the drawing of Fig. 53. The first test article will be the ASTROMAST beam as shown. The ASTROMAST is extremely lightweight (about 5

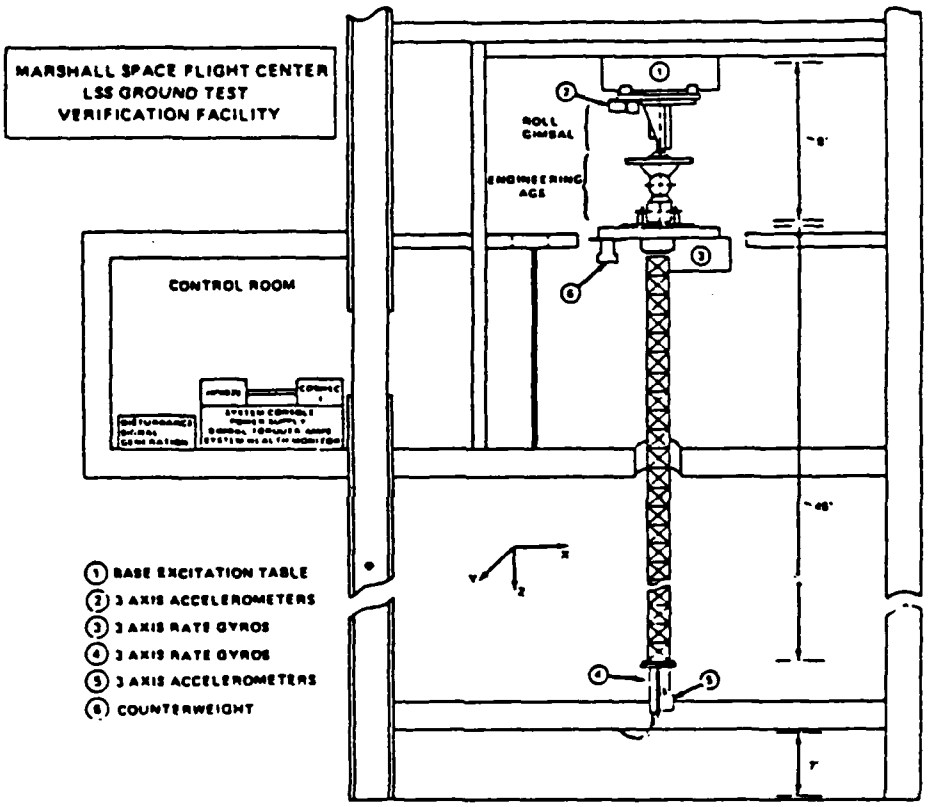

Figure 53. System Layout of MSFC LSS Ground Test Verification Facility.

pounds) and approximately 45 feet in length and is constructed almost entirely of S-GLASS.

The test article is mounted on the faceplate of the Advanced Gimbal System (AGS) engineering model which, along with an additional torque actuator in azimuth, provides the control inputs for the system. The azimuth gimbal also provides a means of rotating the entire experiment manually to produce different test scenarios.

The gimbal system and associated electronics exhibit similar dynamic behavior in each of three axes. The transfer characteristic from commanded torque to applied torque is given by a simple zero over second order system with a simple underdamped pole pair having a natural frequency of 100 Hz and a damping ratio of 0.5. The transfer function is

$$G_{act}(s) = \frac{\text{Actual Torque}}{\text{Commanded Torque}} = \frac{(2\pi\ 100)^2}{s^2 + (2)(.5)(2\pi\ 100)s + (2\pi\ 100)^2} \quad (2.2.2\text{-}1)$$

The frequency response of $G_{act}(s)$ is given in Fig. 54.

The AGS is supported by the Base Excitation Table (BET) of the beam containment structure which is free to translate in the horizontal plane and includes hydraulic actuators to provide translational disturbance inputs to the test fixture. These disturbances can represent Astronaut push-off, RCS (Reaction Control System), thruster firing, or a broadband random disturbance such as would be expected on free flyer type spacecraft.

Six separately packaged inertial measurement assemblies comprise the available control system sensors. Two of the packages, containing three-axis translational accelerometers, are identical. One is mounted on the mast tip, and the other on the AGS side of the BET. Three other packages contain ATM (Apollo Telescope Mount) rate gyros and are installed on the AGS faceplate.

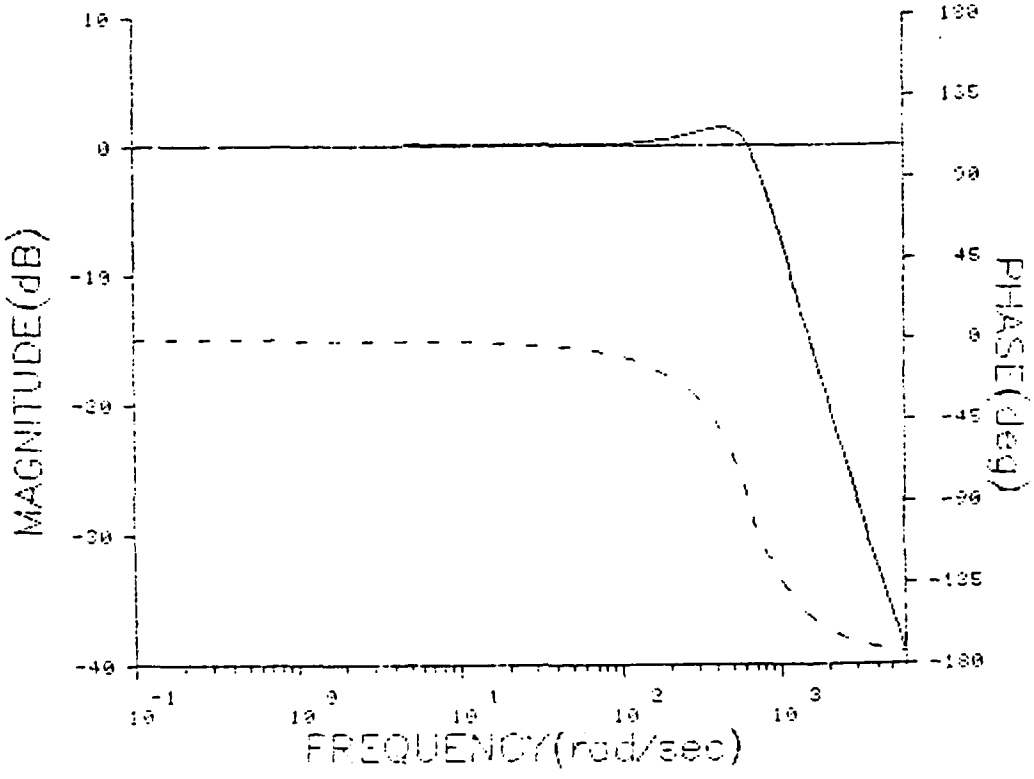

Figure 54. Actuator Frequency Response.

The sixth package, the Kearfott Attitude Reference System (KARS), is placed at the mast tip along with the accelerometer package.

Each of the sensors is assumed to have the dynamic characteristic of the ATM rate gyros, because this is considered to be a worst case. The transfer function of a simple axis of the ATM rate gyros is

$$G_{sen}(s) = \frac{\text{Measured Rate}}{\text{Actual Rate}} = \frac{(2\pi 40)^2}{s^2 + (2)(.7)(2\pi 40)s + (2\pi 40)^2} \qquad (2.2.2\text{-}2)$$

The frequency response of $G_{sen}(s)$ appears in Fig. 55. When this transfer function is used to represent the accelerometers, it represents Measured Acceleration / Actual Acceleration.

The signals from the inertial measurement instruments are read by the COSMEC-I data gathering and control system, and processed 50 times per second according to the control strategy under scrutiny. The control actuator signals are transmitted to the gimbal system as inputs to the dynamical system.

The COSMEC I is interfaced to a Hewlett Packard HP9845C desktop computer which stores data as it is collected during a test run, and then provides post experiment data reduction and display off line. The controller inputs and outputs (measurements and commands) are recorded at each sample period or at some multiple of sample periods.

ASCOT-I Structure Mathematical Model. The model of the ASCOT-I structure serves several purposes - each of which are key to the success of the analysis. The modeshapes and frequencies, which represent the dynamics of the open-loop system, are extracted from the model via the eigensolution of the system equations of motion. These modeshapes and frequencies are typically the necessary input needed to generate a closed-loop control system.

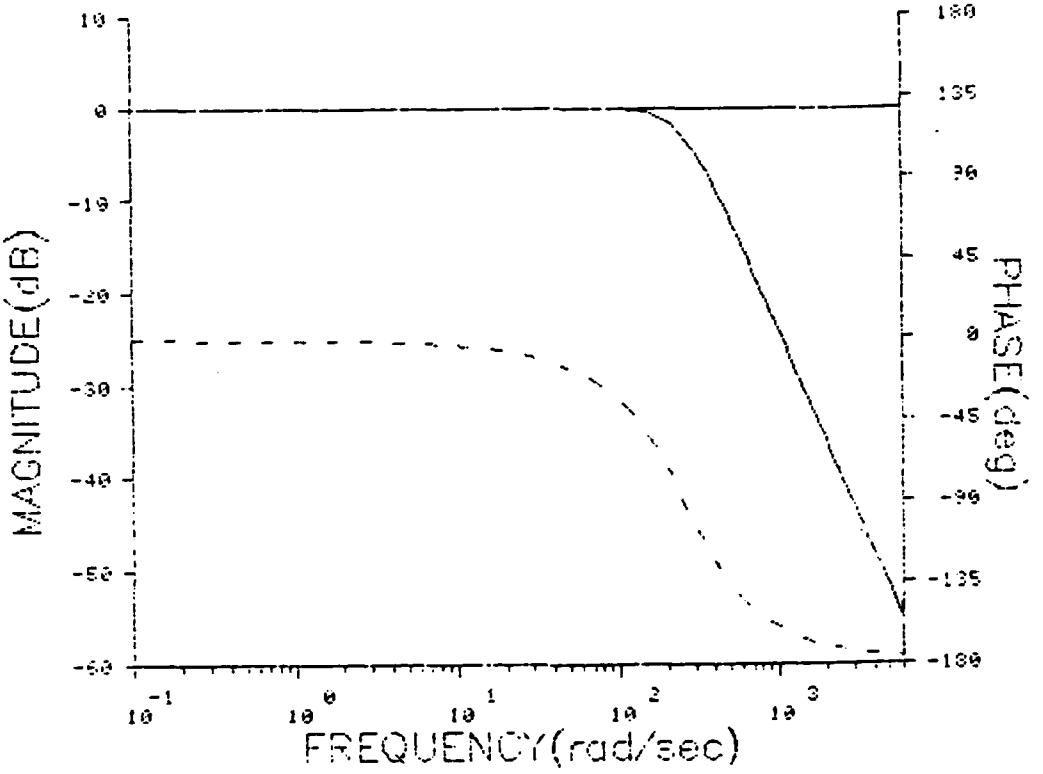

Figure 55. Sensor Frequency Response.

An additional function of the dynamic model is in the simulation of system response due to a prescribed forcing function. Clearly, the accuracy of the predicted response relies heavily on the accuracy of the mathematical model which represents the physical system.

Before the procedures used to actually model the ASCOT-I system are discussed, the system components considered the most critical, either structurally or inertially, will be identified. Referring to Fig. 53, it is seen that the ASCOT-I system is composed of six major components. The six components are identified as - 1. the Base Excitation Table (BET), 2. roll gimbal, 3. Advanced Gimbal System (AGS) gimbals, 4. AGS Faceplate, 5. ASTROMAST beam, and 6. the tip instrument package. Excluding the mass of the BET, the mass of the ASCOT-I system is approximately 310 kg. A discussion of how each of the components is modeled is presented in the following paragraphs.

Modeling Techniques. The main component of the ASCOT system is the ASTROMAST beam. For the purposes of describing the dominant dynamic characteristics of the system, the ASTROMAST beam alone is considered flexible. All other components of the system are modeled as rigid elements.

Over the last several years, several papers have concerned themselves with the analysis of lattice type beam structures [6, 7]. Although several promising analysis techniques have been developed, it appears that measured modal data is presently more accurate than the modal data obtained from the analytical model. Based on this premise, a finite element model of the ASTROMAST beam was assembled and "tuned" to match the measured modal frequencies obtained from a modal test performed at MSFC. A comparison between the natural frequencies presented by the finite element model and the measured frequencies is presented in TABLE 2. As can be seen in the table, the

TABLE 2. COMPARISON OF MEASURED VS. ANALYTICAL NATURAL FREQUENCIES FOR ASTROMAST

		Tuned Finite Element	
	MEASURED (Hz)	MODEL (Hz)	% DIFFERENCE
1st Bending (x-z)	0.555	0.543	-2.16
(y-z)	0.555	0.543	-2.16
2nd Bending (x-z)	3.43	3.41	-0.58
(y-z)	3.43	3.41	-0.58
3rd Bending (x-z)	8.83	9.65	9.29
(y-z)	8.83	9.65	9.29
1st Torsion	4.015	4.016	0.02
2nd Torsion	12.23	12.83	4.87

finite element model has been tuned quite closely to the measured natural frequencies. As expected, the difference between the predicted and measured frequencies tends to increase through the higher frequencies. This is because as the beam assumes more complicated displacement patterns the local non-linearities, which are not explicitly modeled, become more significant to the beam dynamics.

Since the ASCOT-I system must perform in a 1-g environment, the effect of Earth's gravitational field on the system dynamics must be evaluated. The gravity load on the ASCOT-I system manifests itself mainly by altering the frequency associated with the rigid body modes defined by the hinge action of the AGS gimbals. These particular modes, shown in Fig. 56, are essentially rigid pendulum modes, with a natural frequency of 0.15 Hz. The value of this pendulum frequency was obtained through the use of Lagrange's equations applied to a 1-g rigid-body representation of the ASCOT system.

The finite element model of the ASCOT system was used to produce the system modes and frequencies (except for the pendulum frequencies). The natural frequencies of the system are listed in TABLE 3, and some representative modeshapes are plotted in Fig. 56. Except for the pendulum modes, the "beam" portion of the ASCOT system deflects in each of the system modes much like a beam with pinned-pinned boundary conditions. This is clearly the result of the tip instrument mass, which tends to constrain the tip translations since it has a mass of more than 10 times the mass of the beam.

A model of a more complex structure which is currently installed in the LSS/GTV facility and was obtained from MSFC is delineated in Section 2.2.5. This model provides the basis for a second and more challenging application of the S2D2 candidate, ICAT.

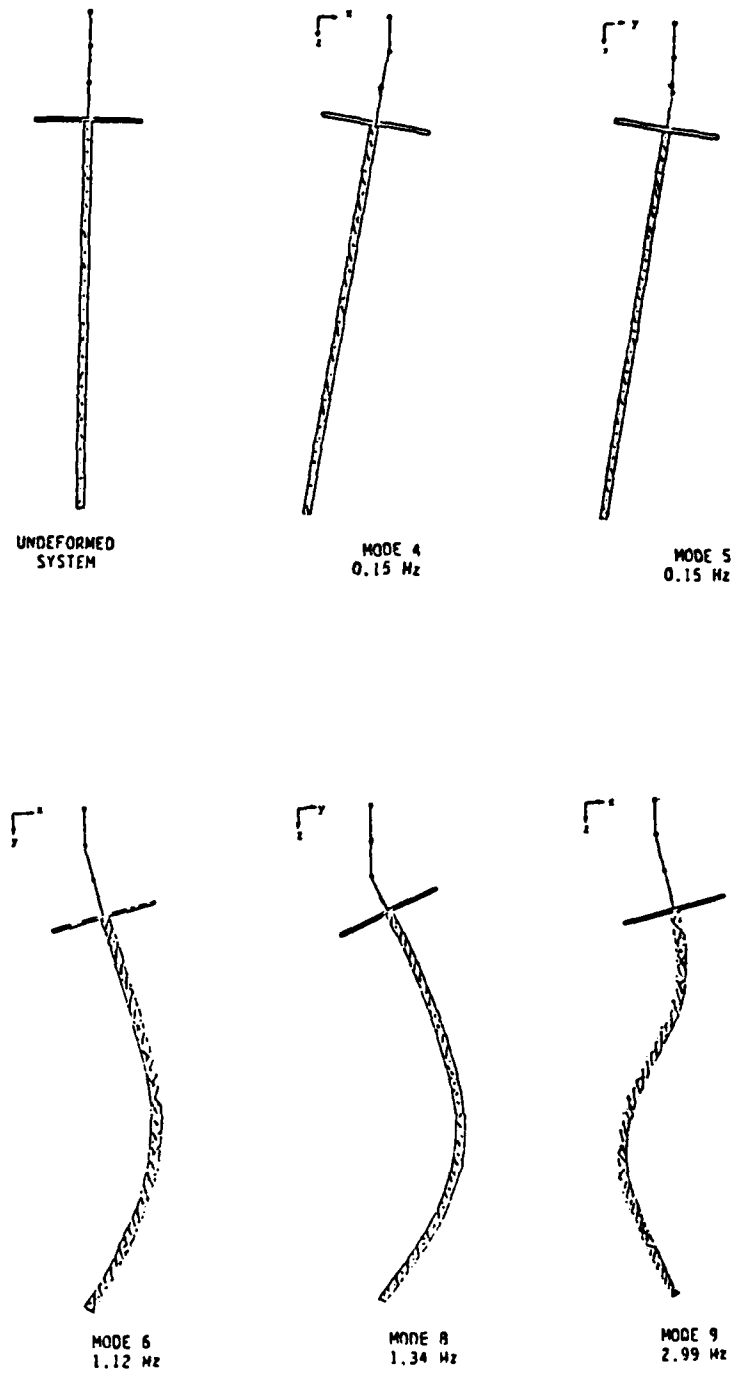

Figure 56. Representative Mode Shapes for the ASCOT-I Structure.

TABLE 3. NATURAL FREQUENCIES OF ASCOT-I SYSTEM

MODE #	FREQUENCY (Hz)	MODIFIED	DESCRIPTION	
1	0.00		RIGID BODY (X-TRANS.)	0
2	0.00		RIGID BODY (Y-TRANS.)	0
3	0.00		RIGID BODY (TORSION)	0
4	0.15		PENDULUM (X-PLANE)	.144
5	0.15		PENDULUM (Y-PLANE)	.149
6	1.12	1.10	1ST BENDING (X-PLANE)	1.18
7	1.19	1.18	1ST TORSION	1.27
8	1.34	1.34	1ST BENDING (Y-PLANE)	1.40
9	2.99	2.96	2ND BENDING (X-PLANE)	3.02
10	3.87	3.86	2ND BENDING (Y-PLANE)	3.91
11	6.70	6.69	3RD BENDING (X-PLANE)	6.69
12	7.02	7.02	3RD BENDING (Y-PLANE)	7.03
13	8.42	8.42	2ND TORSION	8.42

2.2.3 Derivation of Criteria for Evaluating Candidate Control Systems

Introduction

To satisfactorily ascertain control system performance in both a comparative and an absolute sense, a performance evaluation criterion is needed which,

1) uses the Line of Sight (LOS) concept, thus preserving the spirit of previous DARPA sponsored efforts in vibration suppression and pointing control,
2) is an indication of vibration suppression as well as pointing accuracy,
3) can be measured and evaluated during structural tests, and
4) can be applied equally as well to the ASCOT I and the RTOP (Research Technology Operating Plan) models as described in Sections 2.2.2 and 2.2.5 respectively.

The following paragraphs delineate a performance measure which meets the goals set forth above. This LOS criterion is used in the system performance evaluations of Sections 2.1.6 and 2.2.5.

Evaluation Criteria. The evaluation criteria measurements in the y-z plane for the ASCOT I structure are presented in Fig. 57. A light source is attached to the tip instrument mounting bracket such that it points in the z direction and strikes a light sensitive position measurement system. With reference to Fig. 1, the point at which the light beam strikes the sensor with the structure at rest (pre-test) is called "A". Deviation (denoted a_y in the y direction and a_x in the x direction) of the light beam from point A would serve as an acceptable performance evaluation criterion except that it would include as error the pure (rigid body) translation of the system induced

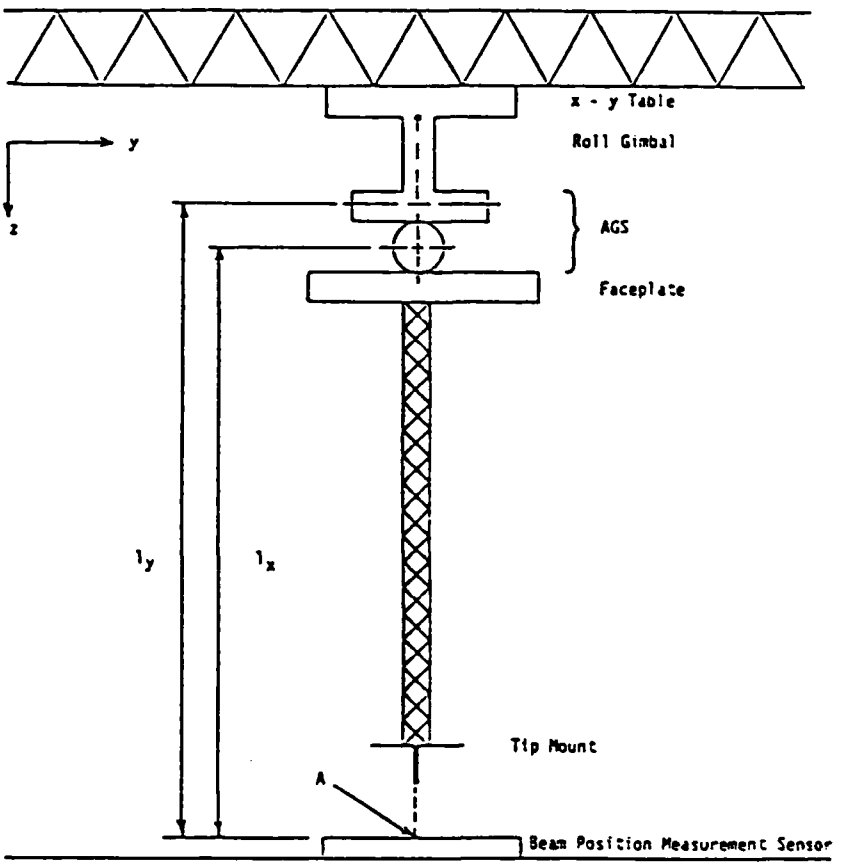

Figure 57. Evaluation Criteria Measurements.

by the x-y translation table. This is not desired because ASCOT is intended to study errors due to pointing and structural vibrations. To remove the components of a_x and a_y due to rigid body translations, the deviations (denoted t_x and t_y) of the x-y table from its at rest (pre-test) position are subtracted from a_x and a_y to yield measures of the pointing accuracy and vibration suppression performance of the system.

Using a small angle approximation, the pointing error quantities may be expressed as

$$\theta_x = \frac{a_y - t_y}{l_x} \qquad (2.2.3\text{-}1)$$

for pointing error about the x-axis and

$$\theta_y = \frac{a_x - t_x}{l_y} \qquad (2.2.3\text{-}2)$$

for pointing error about the y-axis. An overall pointing error quantity is then defined as

$$\theta_M = (\theta^2_x + \theta_y^2)^{1/2} \qquad (2.2.3\text{-}3)$$

Any or all of the above quantities (Equations (2.2.3-1), (2.2.3-2), (2.2.3-3)) may be examined in determining the system performance. These quantities may be studied in terms of their PSD's and RMS values when broadband random disturbances are applied to the system or, in the case of deterministic disturbances, their time functions may be studied.

Conclusion. The evaluation criteria delineated above satisfy the four goals set forth in the introduction. In particular, they use a line of sight concept which is an indication of vibration suppression and pointing accuracy but does not involve pure translation of the structure. The criteria can

easily be measured and evaluated during structural tests using relatively simple hardware which may be affixed to the structure without significantly changing the structural behavior. Finally, these criteria may be applied to the RTOP structure without modification, because the same essential structural elements compose both it and the ASCOT-I structure.

2.2.4 Selection of Candidate Control Systems

This section discusses briefly three well developed LSS control system design techniques which are considered candidates for application to structures such as the ASCOT-I and RTOP structural models.

Low Authority Control/High Authority Control (LAC/HAC). Lockheed Missile and Space Corporation's LAC/HAC approach to LSS control system design is characterized by a two pronged attack of the problem. Low Authority Control (LAC) is used to moderately modify the damping of the high frequency (i.e., less certain) modes. LAC appears to be readily implementable but the performance attributable to it seems limited.

High Authority Control (HAC) is coupled with LAC to provide heavy damping of the low frequency (typically better known) modes. HAC is implemented using a Linear Quadratic Gaussian (LQG) design which requires all states of the system to be measured or, at least estimated. This unfortunately leads to very high order digital controllers.

Positivity. Investigation of TRW's Positivity technique has shown that the design is a multistep process beginning with a predesign which modifies the plant characteristics so that it is positive real. Then performance specifications are satisfied by designing a feedback controller that is positive real. This procedure assures that the closed loop system will be

stable. However, because the design is based upon a truncated system model, the actual system (proof model) is not assured of stability.

Modal Error Sensitivity Suppression (MESS). General Dynamics' MESS is a third candidate for LSS control system designs. The MESS design procedure requires the separation of the modeled modes into two groups: (1) low frequency modes to be controlled and (2) High frequency modes to be suppressed. An LQG problem is then solved to produce the control law.

2.2.5 Comparison of Candidate Control Designs

This report section covers the effort performed under Task 4.1.2.5 as delineated in Section IV of the ASCOT Technical/Management Program Development Plan.

Introduction. Application of the S2D2 candidate, ICAT, to the RTOP (Research Technology Operating Plan) model of the LSS/GTV facility fixture is covered in this section. Discussion begins with a description of the structure and resulting structural model. Then the design model is produced, and the controller design description ensues. Once designed, the controller is coupled to plant model to evaluate the overall system performance with respect to bandwidth and disturbance rejection.

RTOP Structural Model. The RTOP structure, so named because it is being used in NASA/MSFC testing sponsored under a Research Technology Operating Plan (RTOP), is an augmentation of the ASCOT-I structure. As can be inferred from Figure 58 , the RTOP structure and resulting model contain all of the principle components of the ASCOT-I structure plus an additional aluminum cruciform connected to the tip instrument package. The effect of the cruciform is to add several lightly damped flexible modes to the structure. An indication of the system complexity is the spacing and number of the system

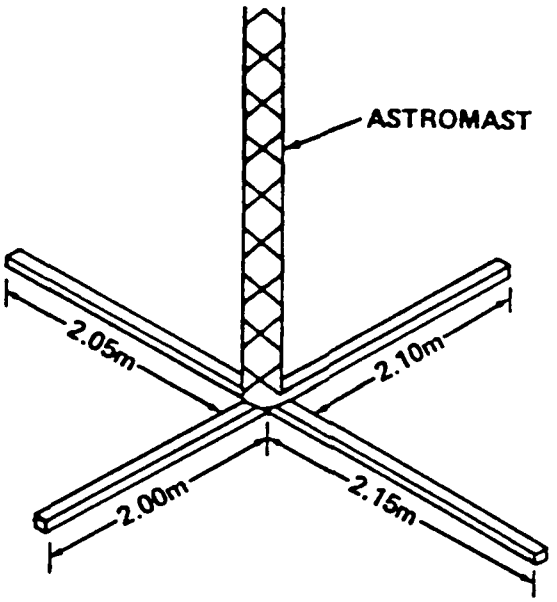

Figure 58. Cruciform Structure of RTOP Model.

natural frequencies, which are shown in TABLE 4. As in the ASCOT-I model, the effects of gravity upon the structure are included; thus, the pendulum behavior appears rather than typical zero frequency rigid body modes.

The RTOP model differs from the ASCOT-I model in that it exhibits light cross-axis coupling, thus posing a more apt application for S2D2.

RTOP Design Model. The RTOP design model along with the control system topology is shown in Figure 59. The blocks labeled I(z) represent the rectangular integration carried out in the strapdown algorithm and are modeled with the z-transform, $I(z) = Tz/(z-1)$. $G_{ho}(s)$ represents a zero order hold device and is modeled by the transfer function, $G_{ho}(s) = (1-e^{-Ts})/s$.

The design model incorporates the first 40 modes of the RTOP structural model. This set includes five modes with frequencies greater than the half sample rate of 157 rad/sec (50 Hz) and a largest model frequency of 390 rad/sec (62 Hz). The modes above the half sample rate are included so that their effects on the sampled data system stability analysis can be realized. The actuator and sensor models of Equations (2.2.2-1) and (2.2.2-2) respectively are included as shown in Fig. 59, and LOS_x and LOS_y are computed as described in Section 2.3.3.

The measurements used in the RTOP design include the three faceplate rotational rates ($\dot{\theta}_x$, $\dot{\theta}_y$, $\dot{\theta}_z$) used in the ASCOT-I design and in addition, the ASTROMAST tip translational accelerations in x and y ($\ddot{x}$, $\ddot{y}$). The faceplate measurements are used in the same manner as in the ASCOT-I design while the tip measurements are used to effect damping of the pendulum behavior. This is discussed in greater detail in the following section. The effector inputs are the same as in the ASCOT-I model: gimbal torque in each of the three axes (T_x, T_y, T_z).

TABLE 4. NATURAL FREQUENCIES OF RTOP SYSTEM

Mode #	Frequency (Hz)	Description
1	0.00	Rigid Body (x-trans)
2	0.00	Rigid Body (y-trans)
3	0.00	Rigid Body (torsion)
4	0.14	Pendulum (y-z)
5	0.15	Pendulum (x-z)
6	0.38	1st torsion
7	1.10	Tip reformation
8	1.15	Tip reformation
9	1.16	Tip reformation
10	1.21	Tip reformation
11	1.22	Tip reformation
12	1.27	Tip reformation
13	1.28	Tip reformation
14	1.32	2nd BNDG (x-z)
15	1.45	2nd BNDG (y-z)
16	3.02	2nd torsion
17	3.45	3rd BNDG (x-z)
18	3.90	3rd BNDG (y-z)
19	6.55	4th BNDG (x-z)
20	6.90	4th BNDG (y-z)

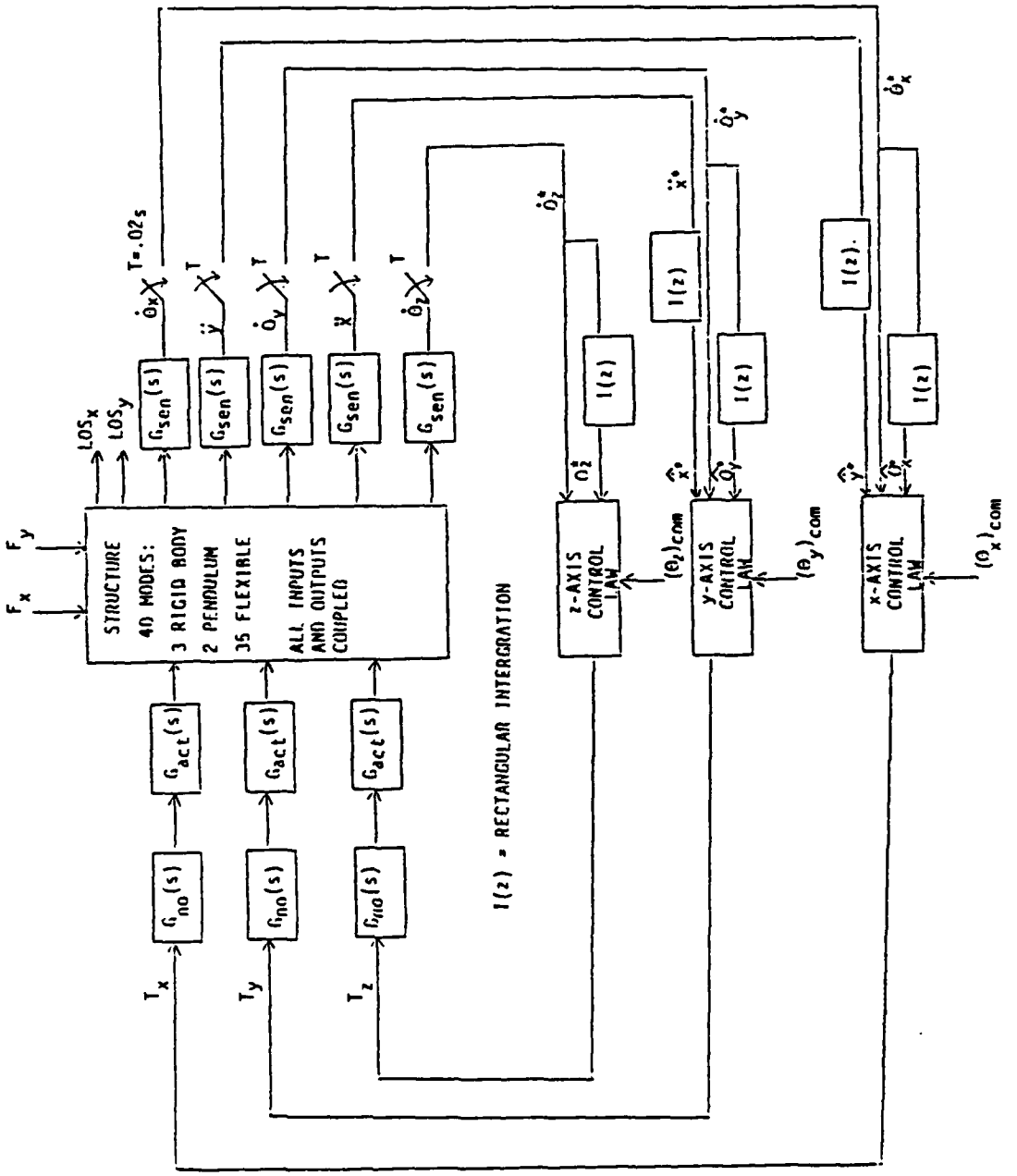

Figure 59. RTOP Design Model and Control System Block Diagram.

RTOP Controller Design. Examination of Figure 59 reveals that the chosen RTOP controller topology is decoupled between axes despite the coupled nature of the RTOP structural model. (Note that the tip translation in y represents gimbal rotation about x). The S2D2 candidate, 1CAT, can handle not only the cross axis coupling of the structure but also the design of cross-axis coupled control systems. However, examination of the cross-axis transfer characteristics of the RTOP structure (faceplate rotational rate about y due to torque in z for instance) reveals that closure of such paths in the controller would probably cause stability problems and/or fail to improve system performance.

The x-axis control law architecture is given in the block diagram of Fig. 60. This control strategy uses faceplate angular rate ($\dot{\theta}_x^*$) to damp the flexible modes, ASTROMAST tip rate ($\hat{\dot{y}}^*$) to damp the pendulum mode, and faceplate position ($\hat{\theta}_x^*$) to facilitate pointing. The blocks $D_y(z)$, $D_{\dot{\theta}_x}(z)$, and $E_{\theta_x}(z)$ are unspecified z-transforms, and T_x is the torque command output which is applied to the gimbal torquer characteristic as shown in Fig. 59. The y-axis control law is identical in form to that of the x-axis as seen from Fig. 61. The z-axis control law is similar but lacks the translational rate measurement as seen in Fig. 62.

Including all three axes, the RTOP controller involves eight feedback paths and, therefore, eight loops. Five of these, referred to as "rate loops", are used to augment the damping of the flexible and pendulum behavior of the structure while the remaining three, "position loops" are used to facilitate position control. Because the loops are to be closed one at a time but not independently, some choice of closure order must be made. Following the lead of experience, the widest bandwidth loops in each axis will

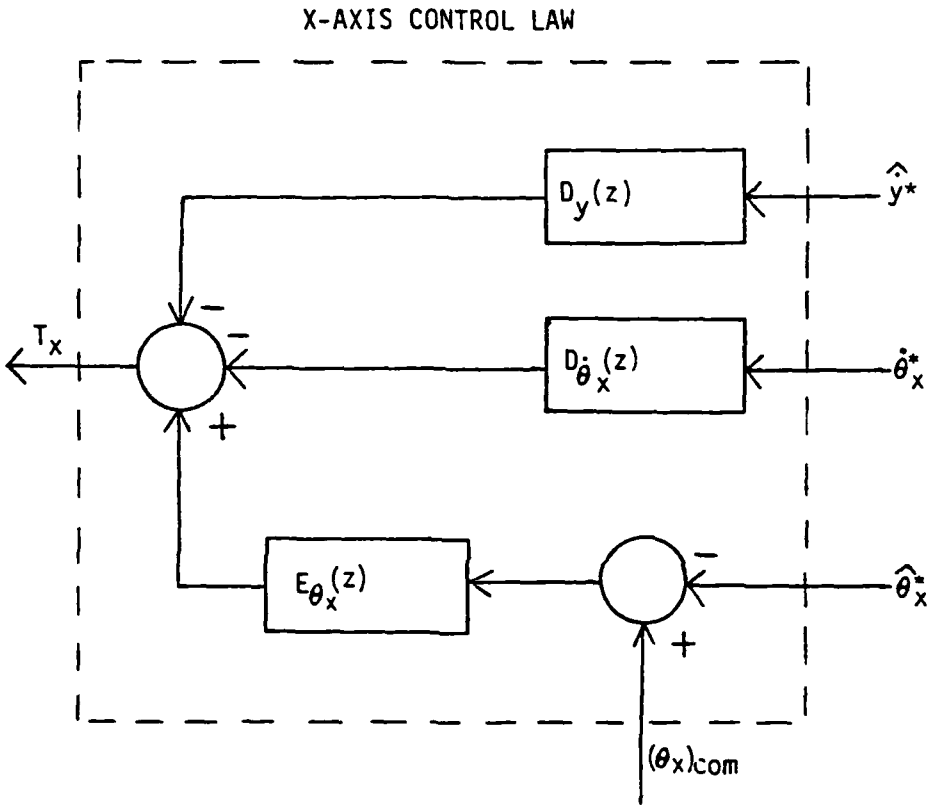

Figure 60. RTOP X-Axis Control Law Block Diagram.

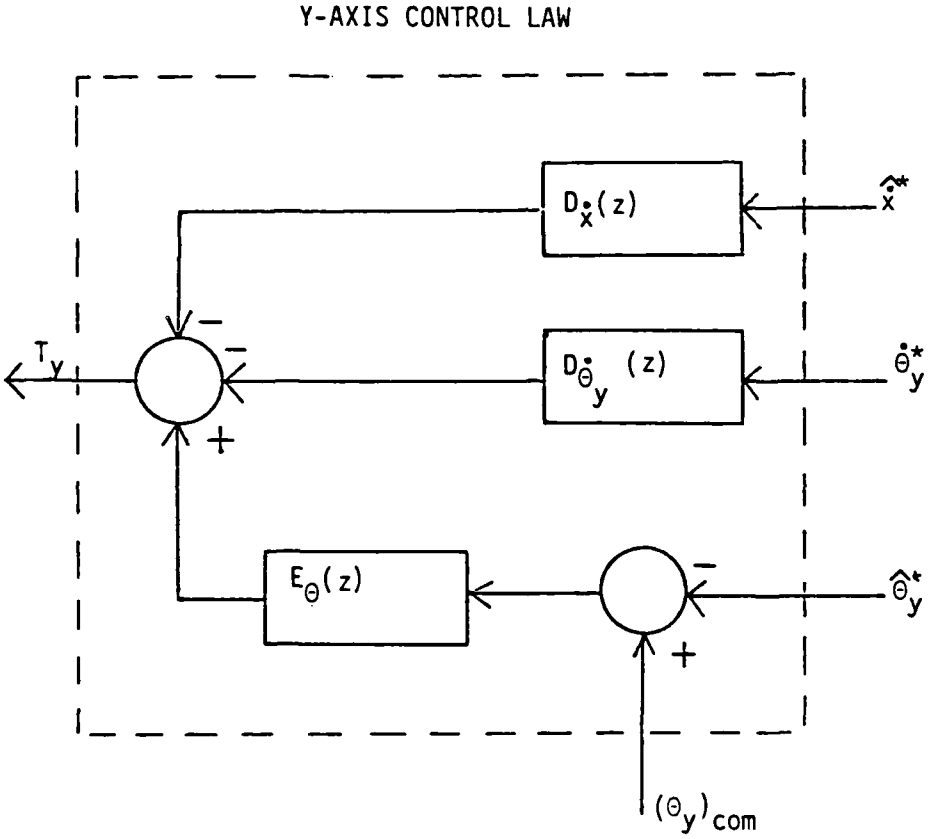

Figure 61. RTOP Y-Axis Control Law Block Diagram.

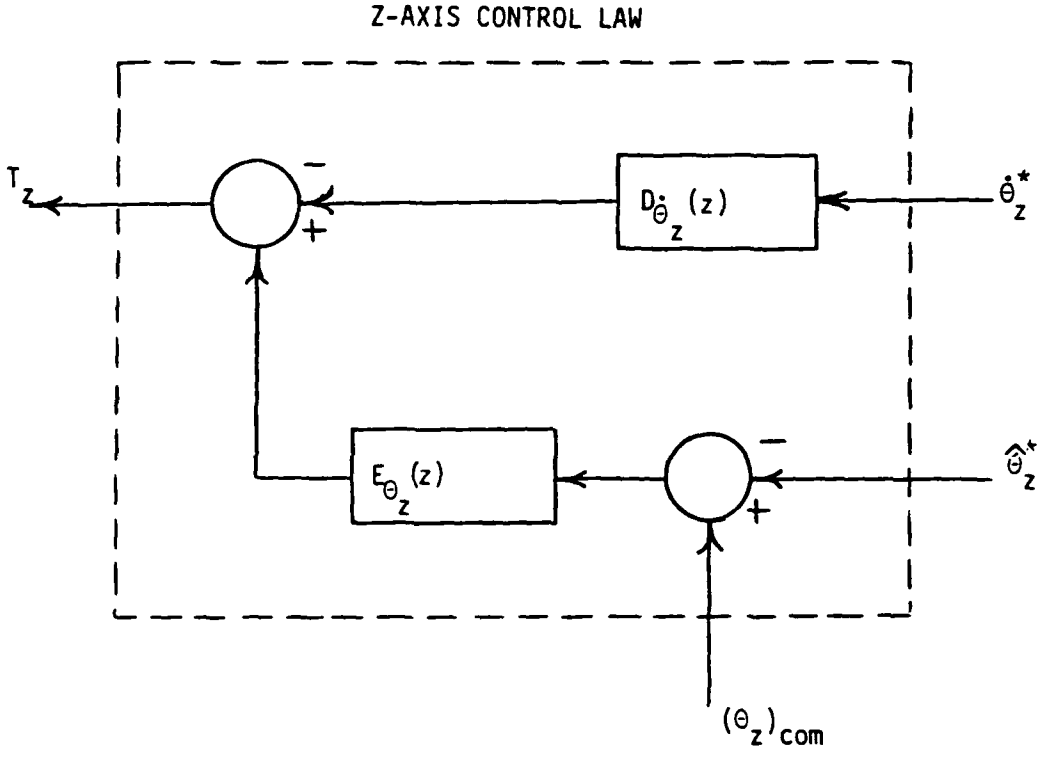

Figure 62. RTOP Z-Axis Control Law Block Diagram.

be closed first. The question of which axis to begin closures in is not important in the RTOP design because of the light coupling; however, in a system exhibiting heavy coupling, preference might be given to a particular axis.

TABLE 5 provides a summary of the eight loop closures required along with the compensation and resulting stability margins of each loop. The loops are closed in order of the loop number, and each time a loop is closed, it remains closed from that time on in the analysis. The following discussion examines the closure of loops 1, 4, and 6; thus following the progression of the x-axis controller. This is not to say that the x-axis controller is designed independently. Quite to the contrary, examination of TABLE 5 shows that the design is being executed in the three axes somewhat simultaneously.

The loop frequency response of the compensated x-axis faceplate rate loop (loop number one) appears in Fig. 63. Since the compensation is simply a gain of 31dB, the uncompensated response is the same as that of Fig.63 except shifted down in magnitude by 31dB. As in the ASCOT-I design, it is desired that the modal peaks of the compensated loop response extend beyond 0dB in order to produce damping of the modes, and this is accomplished for several of the flexible body modes. However, no damping is added to the pendulum mode. This is primarily because of the lag due to the sensor and actuator characteristics (60 degrees at the half sample rate) which were not modeled in the ASCOT-I design where damping of the pendulum mode was accomplished. Dynamic compensation is not helpful in allowing greater gain in this loop for two reasons: (1) lag due to the sensor and actuator dynamics, and (2) uncertainty of the modal frequencies of the higher frequency modes.

TABLE 5. SUMMARY OF RTOP COMPENSATION AND STABILITY MARGINS

LOOP NUMBER	MEASUREMENT	ACTUATION	COMPENSATION	GAIN MARGIN (DB)	PHASE MARGIN (DEG)
1	$\dot{\theta}^*_X$	T_X	$D_{\theta X}(z) = 31DB$	20	55
2	$\dot{\theta}^*_Y$	T_Y	$D_{\theta Y}(z) = 41DB$	20	70
3	$\dot{\theta}^*_Z$	T_Z	$D_{\theta Z}(z) = 30DB$	30	85
4	$\dot{Y}^*$	Tx	$D_Y(z) = 37DB\ \underline{/180°}$	10	90
5	$\dot{X}^*$	T_Y	$D_X(z) = 45DB$	10	87
6	θ^*_X	T_X	$E_{\theta X}(z) = 53DB \cdot I(z)$	6	75
7	θ^*_Y	T_Y	$E_{\theta Y}(z) = 60DB \cdot I(z)$	10	42
8	θ^*_Z	T_Z	$E_{\theta Z}(z) = 35DB$	37	64

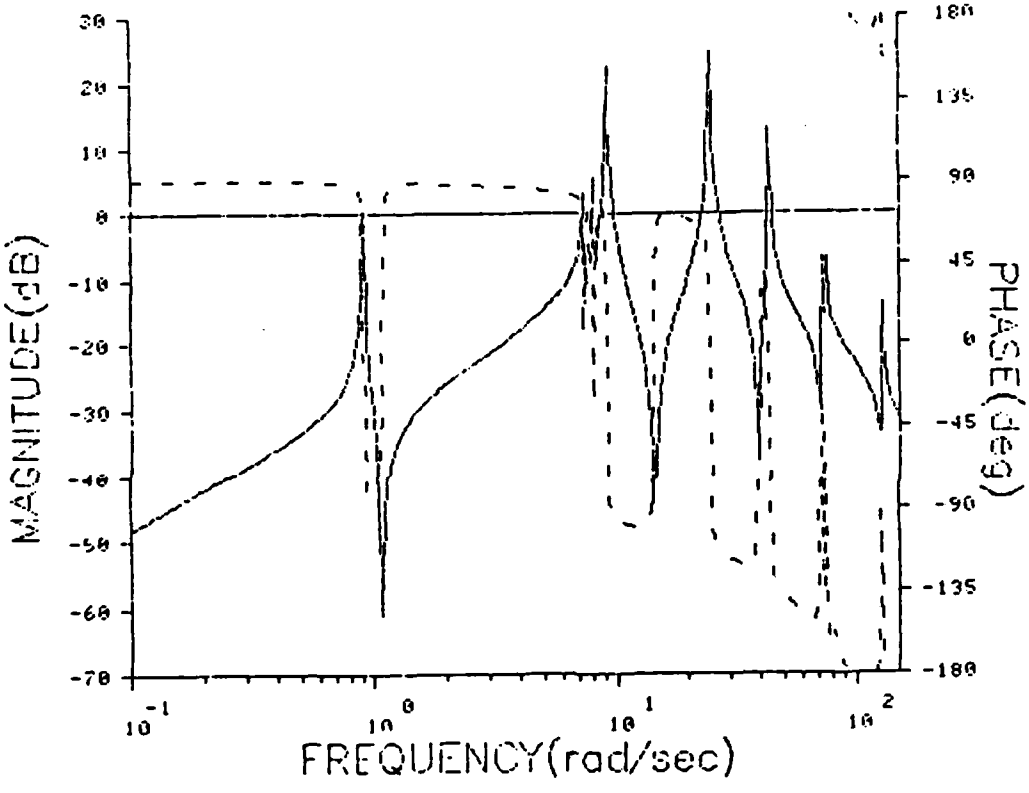

Figure 63. Compensated X-Axis Faceplate Rate Loop Frequency Response (Bode Plot).

The polar plot of Fig. 64 shows that the closed loop system with loop 1 closed is stable with stability margins of 10dB and 55 degrees.

Closure of loops two and three (faceplate rate loops in y and z) continues in similar fashion to that described above with the cumulative effects of the previous loop closures included in the design of each compensator. This brings the design to loop four and, once again, the x-axis. The next widest bandwidth loop in the x-axis is the tip translational rate loop. This loop is included for the express purpose of damping the pendulum behavior. One of the obvious problems with damping the pendulum mode using the faceplate rate measurement is that it is not sensed nearly as much (and does not peak nearly as high) as the flexible modes when sensed at the faceplate. However, for small angles the pendulum mode is revealed at the ASTROMAST tip as pure translation in the off-axis. With the bending modes damped by the closures of loops one through three, the pendulum mode peaks nicely as shown in the compensated x-axis tip translational rate loop frequency response of Fig. 65. The compensation is a gain of 37dB and negative in sign. The negative polarity is necessary because positive translation in y represents negative rotation about x and, therefore, the negative in the compensator must be included to provide the correct (odd) number of negative signs around the loop. The polar plot of Fig. 66 shows the stability of the closed loop system with a gain margin of 10dB and a phase margin of 90 degrees.

Closure of the y-axis tip translational rate loop is similar to the x-axis case except that the negative in the compensation is not needed because no negative occurs due to the coordinate system.

The final loop to be closed in the x-axis is loop 6, the x-axis position loop. The design begins with consideration of the open loop frequency

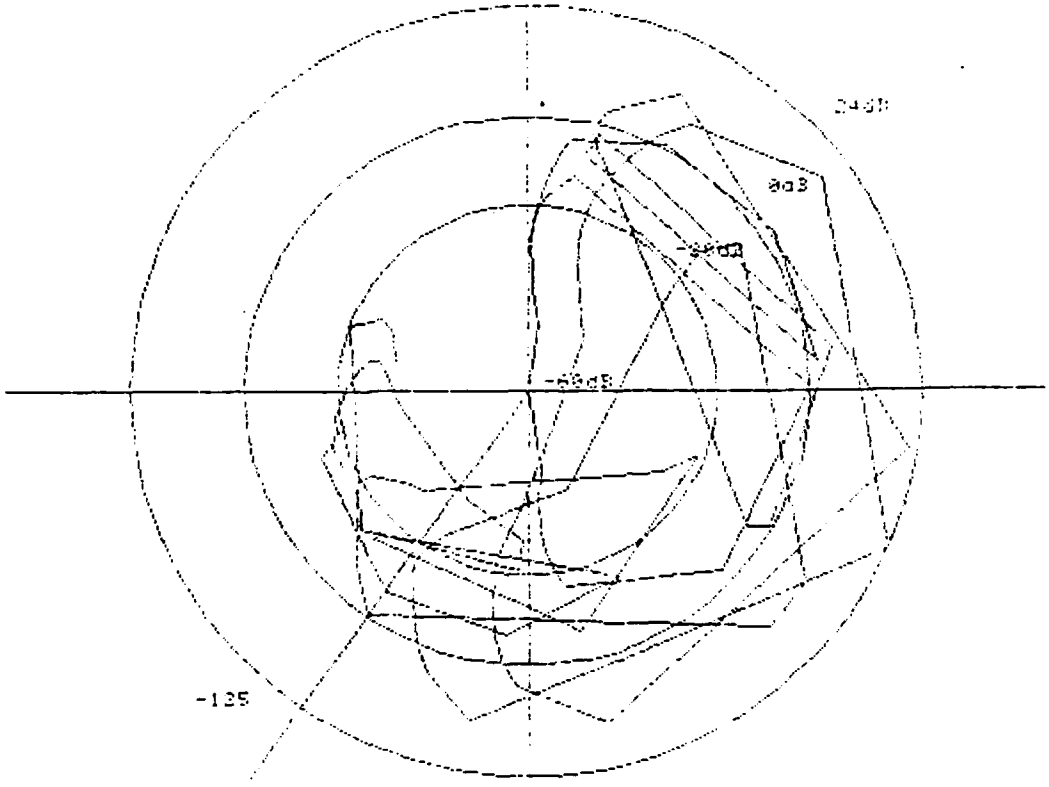

Figure 64. Compensated X-Axis Faceplate Rate Loop Frequency Response (Polar Plot).

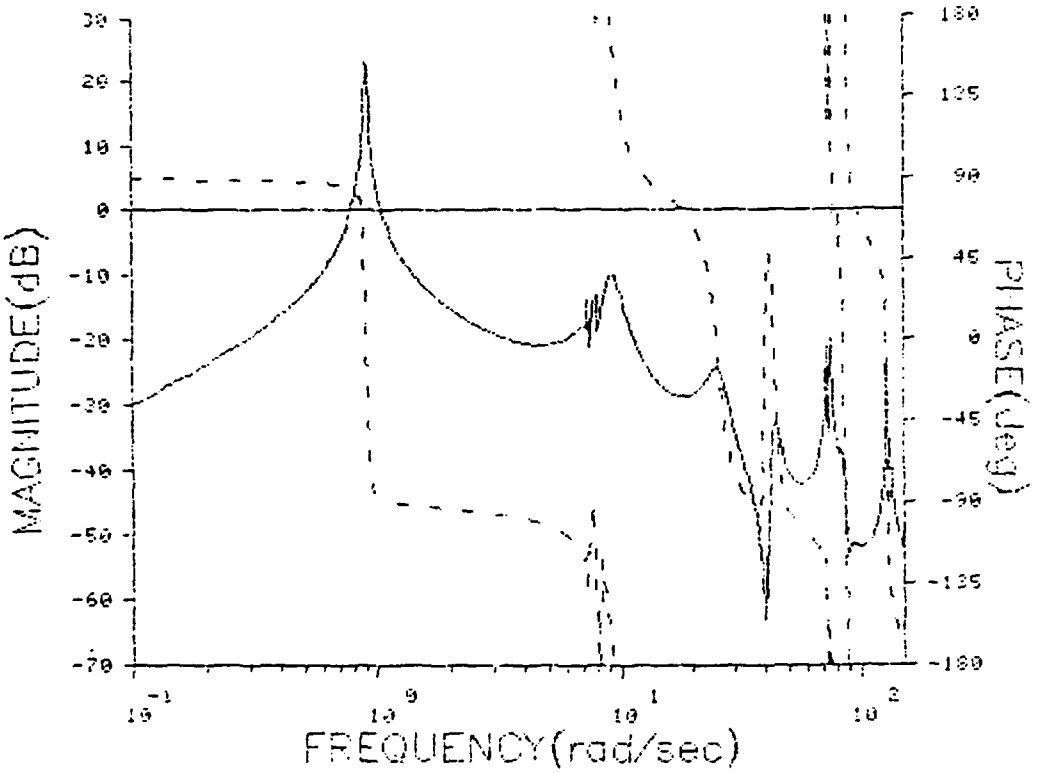

Figure 65. Compensated X-Axis Tip Rate Loop Frequency Response (Bode Plot).

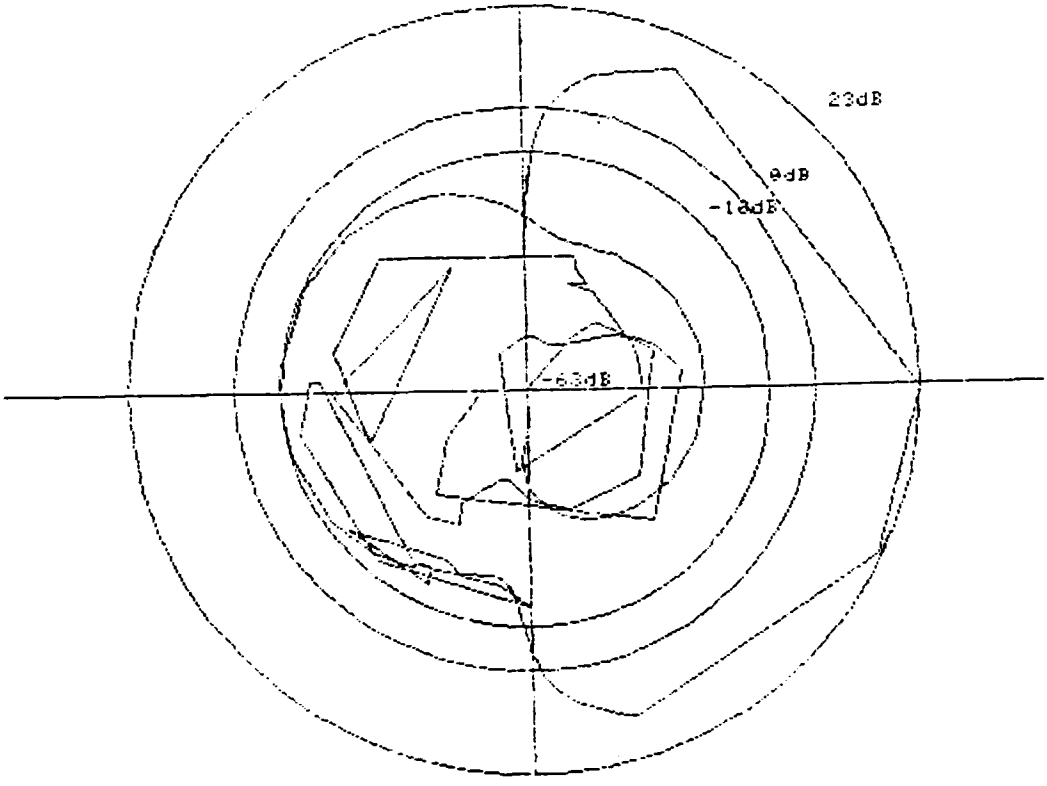

Figure 66. Compensated X-Axis Tip Rate Loop Frequency Response (Bode Plot).

response from T_x to $\hat{\theta}_x^*$ with the first five loops closed. (See Fig. 67.) In this response both the pendulum mode and the dominant bending modes exhibit considerable damping because of the closure of the first five loops. As in the ASCOT-I design, the magnitude frequency response does not come in at -20dB/decade because of the absense of the rigid body mode. As before, an integrator is specified as part of the compensation, and the response of Fig. 68 results after inclusion of a 53dB gain factor. The polar plot of Fig. 69 shows the stability margins of 6 dB and 75 degrees.

The design is completed with closure of the y and z-axis position loops in a similar manner to that described above. The resulting compensation and stability margins for these and all of the loops are given in TABLE 5.

RTOP System Performance. The RTOP system performance is evaluated in the same manner as the ASCOT-I system. (See Section 2.1.6.) All inputs, outputs, and criteria are the same, the difference between the two analyses being the structural model and controller.

The first point of consideration is the position loop bandwidth. Figs. 70, 71 and 72 display the closed position loop frequency responses for the x, y and z axes respectively. The system exhibits a closed position loop bandwidth of .9 rad/sec in both the x and y axes. The lack of improvement in bandwidth in the RTOP system over the ASCOT-I system, despite the more complicated eight loop control system, may come as a surprise to the reader. The case is that the improvement possible because of the additional control loops was offset by the inclusion of sensor and actuator dynamics which weren't present in the ASCOT-I system. The z-axis exhibits a bandwidth of 2 rad/sec and is considerably more behaved than the other axes because of the lack of multitudinous flexible body modes.

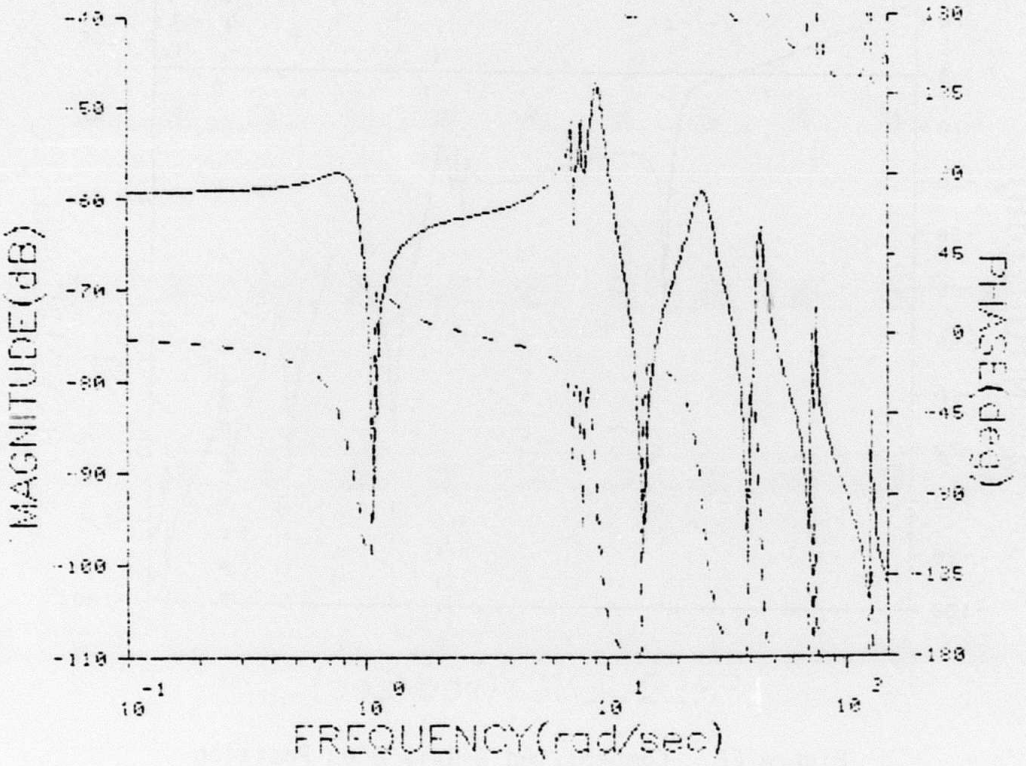

Figure 67. X-Axis Open Position Loop Frequency Response (Bode Plot).

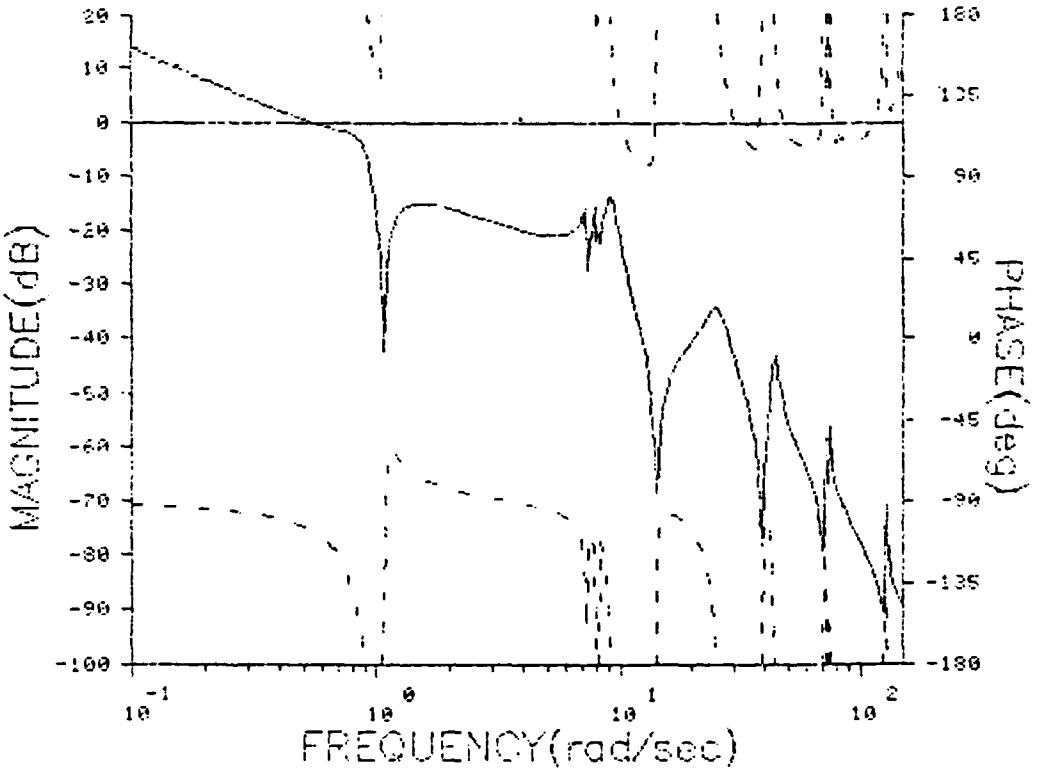

Figure 68. Compensated X-Axis Open Position Loop Frequency Response (Bode Plot).

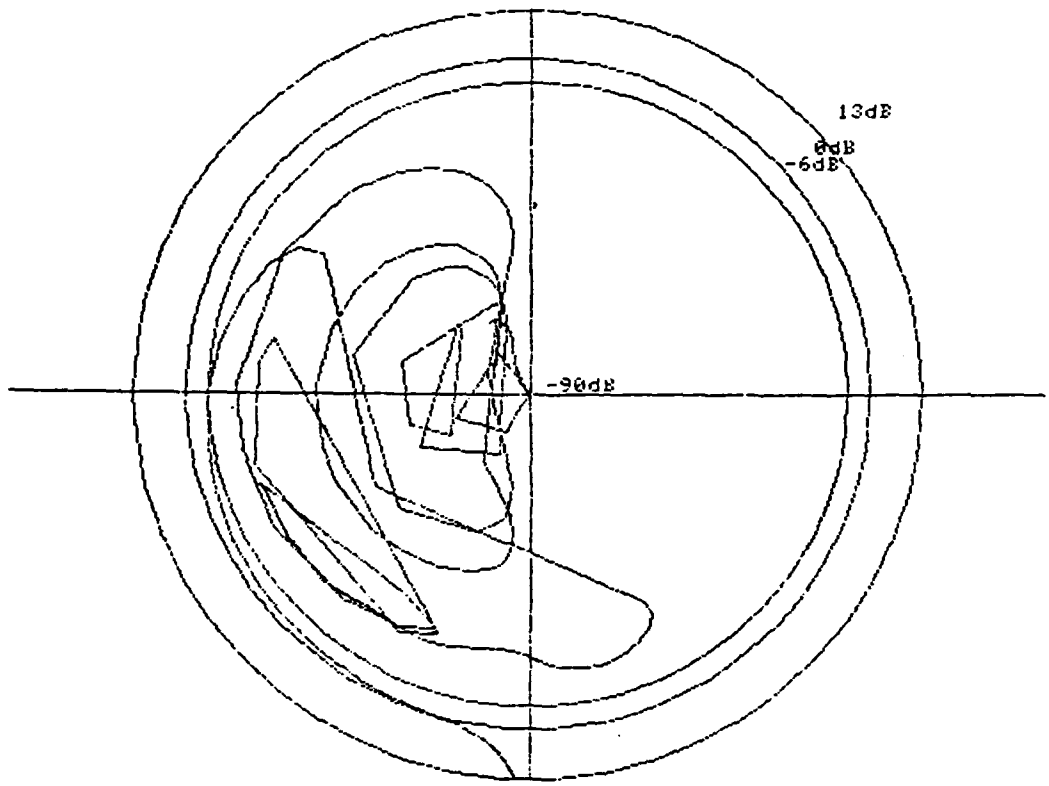

Figure 69. Compensated X-Axis Open Position Loop Frequency Response (Polar Plot).

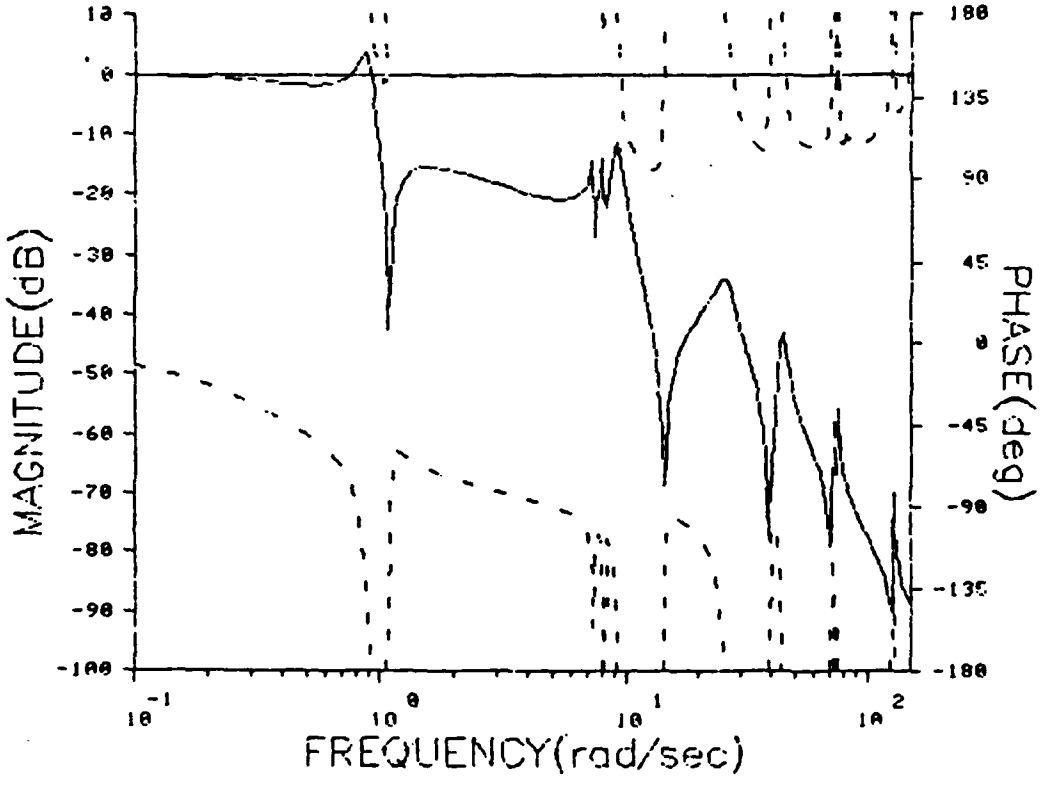

Figure 70. Closed X-Axis Position Loop Frequency Response (RTOP).

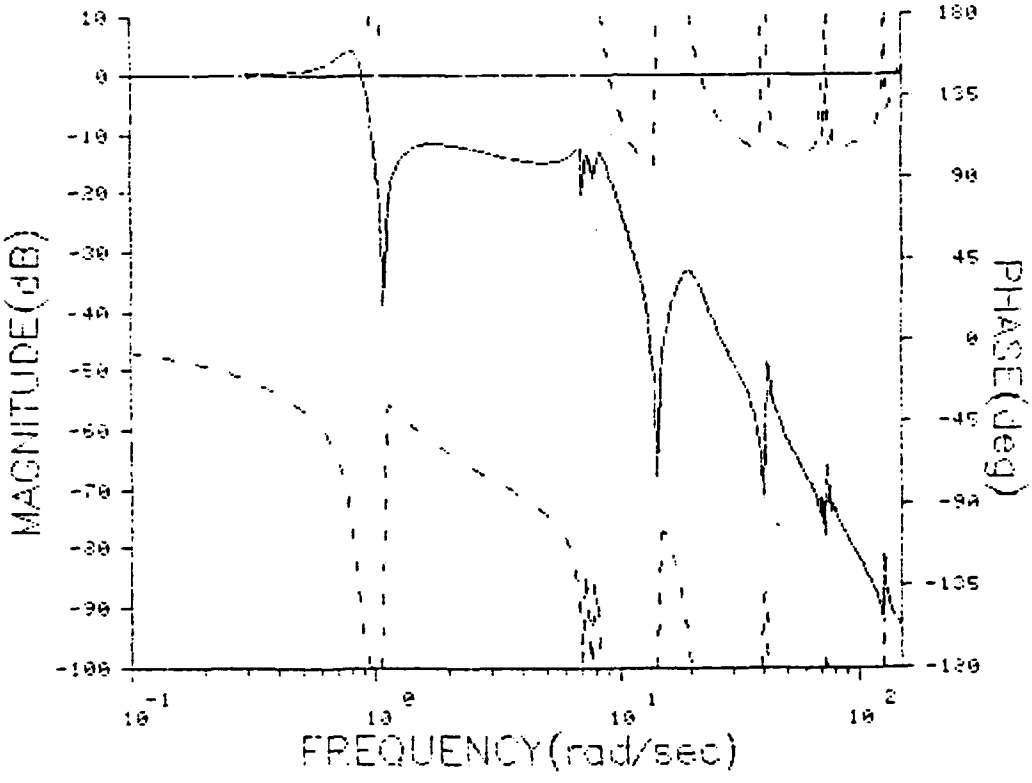

Figure 71. Closed Y-Axis Position Loop Frequency Response (RTOP).

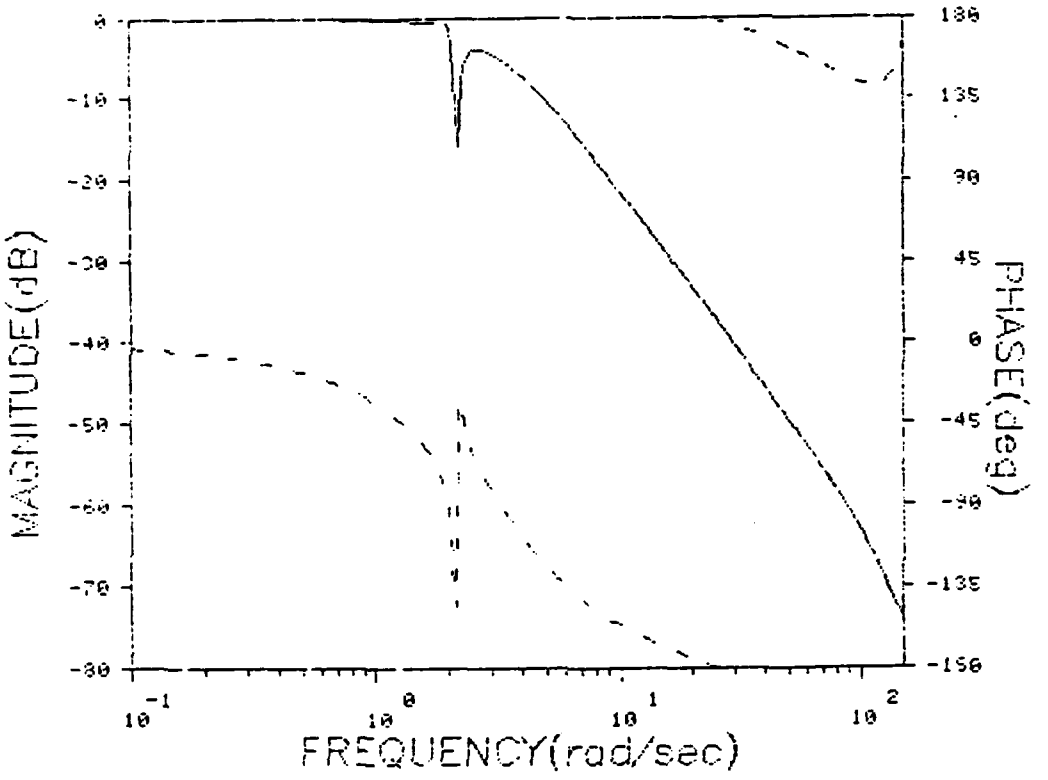

Figure 72. Closed Z-Axis Position Loop Frequency Response (RTOP).

In rejection of random disturbances, the RTOP system, again, exhibits only slight improvement over that of the ASCOT-I system. Fig. 73 presents the PSD of the LOS_x response to a broadband random disturbance in the y-direction with no control system (open loop), and Fig. 74 displays the same quantity with the control system included. Clearly, much of the peaking is reduced in the closed loop case, resulting in a reduction in RMS error from 1.6×10^{-4} rad. in the open loop case to 3.7×10^{-5} rad. in the closed loop case. Similar quantities appear for LOS_y evaluation in Figs. 75 and 76 which represent a reduction of RMS error from 2.0×10^{-4} rad. to 3.6×10^{-5} rad.

Disturbance rejection in response to deterministic disturbances is computed the same for the RTOP system as for the ASCOT-I system. The crew motion disturbance responses are considered first by examination of Figs. 77, 78, and 79 which display the LOS_x, LOS_y, and overall LOS responses, respectively, to the crew motion disturbance. In all cases the crew motion disturbance excites the bending modes very little. As in the ASCOT-I studies, the crew motion responses are dominated by the pendulum behavior. However, the RTOP model closed loop responses exhibit considerably more damping than their counterparts in the ASCOT-I studies. (See Figs. 45, 46, and 47.)

The RCS thrusters firing disturbance responses provide a better evaluation of the effects of the RTOP controller on the flexible behavior of the structure. The open loop LOS_x response of Fig. 80 shows that the bending modes of the structure are excited by the RCS disturbance. The corresponding closed loop response shows that the bending behavior is quickly damped out; however, both responses are still dominated by the pendulum action. Examination of Figs 81 and 82 reveal similar behavior in the LOS_y and overall LOS responses.

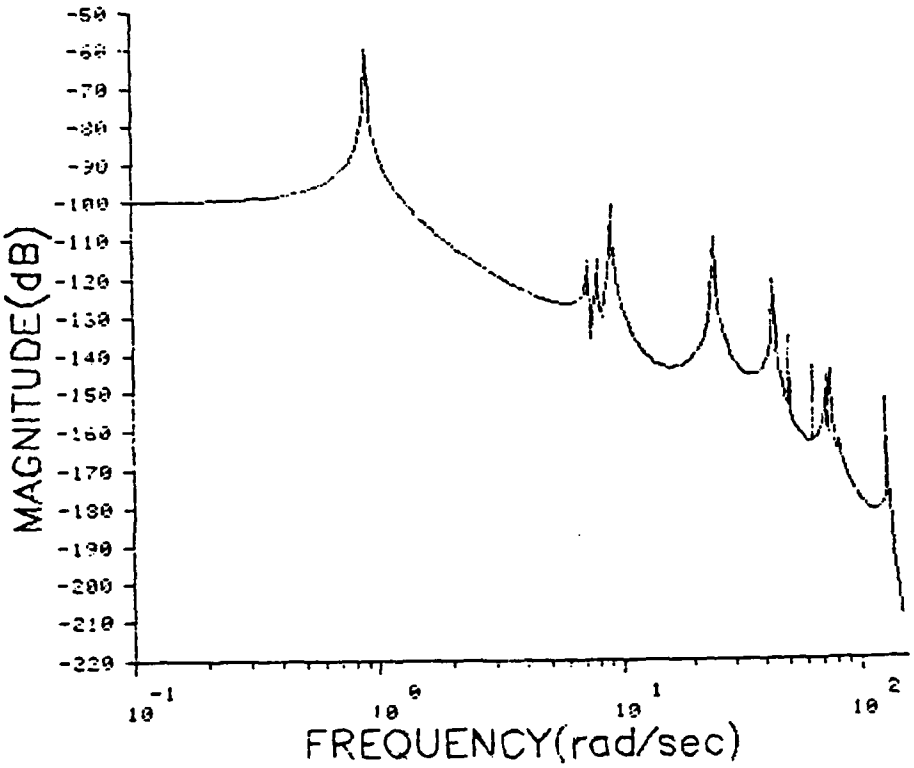

Figure 73. PSD of X-Axis LOS Open Loop Response to a Random Disturbance Y (RTOP).

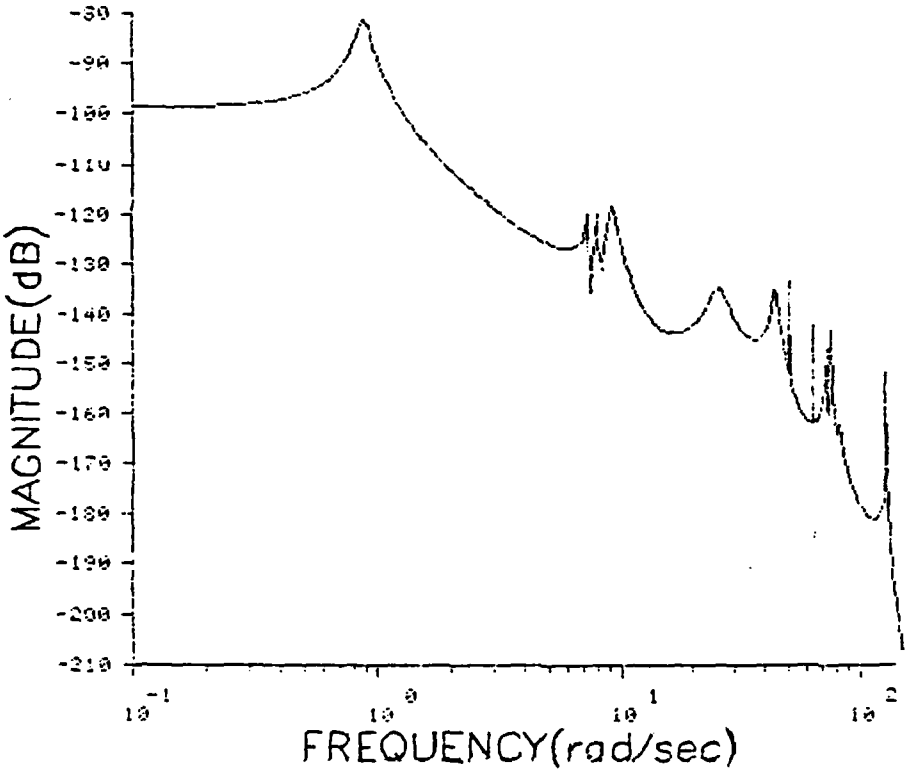

Figure 74. PSD of X-Axis LOS Closed Loop Response to a Random Disturbance in Y (RTOP).

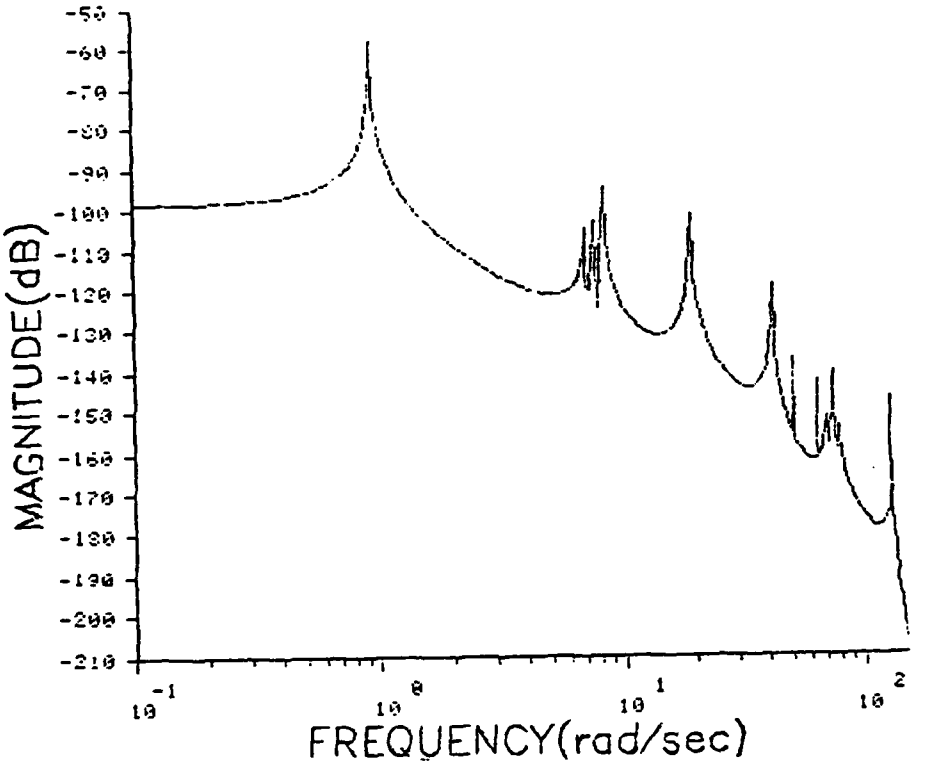

Figure 75. PSD of Y-Azis LOS Open Loop Response to a Random Disturbance in X (RTOP).

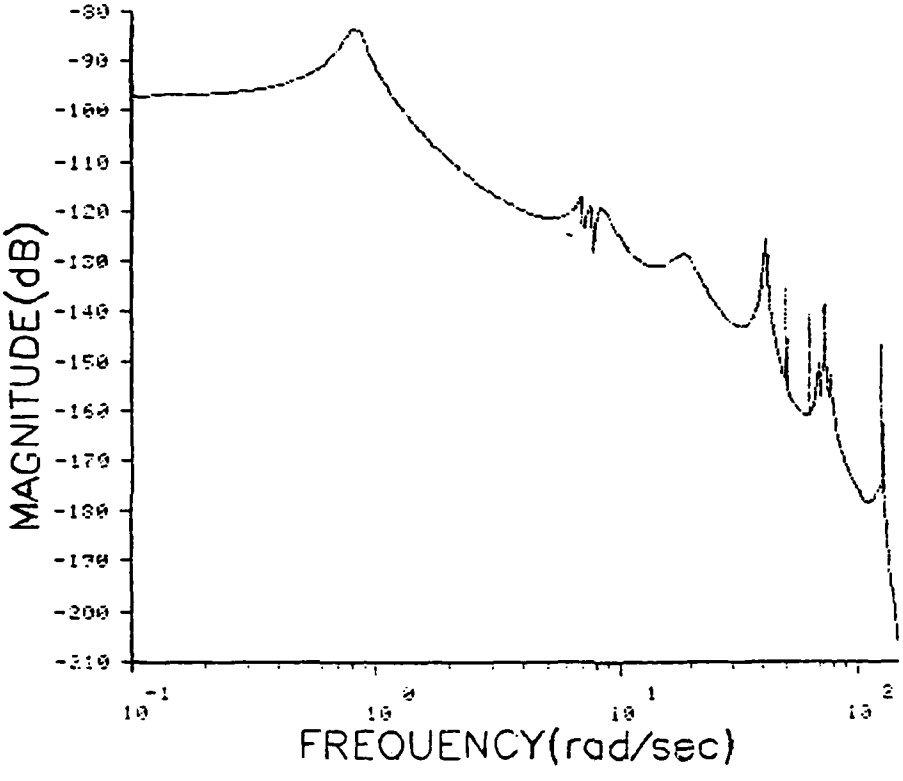

Figure 76. PSD of Y-Axis LOS Closed Loop Response to a Random Disturbance in Y (RTOP).

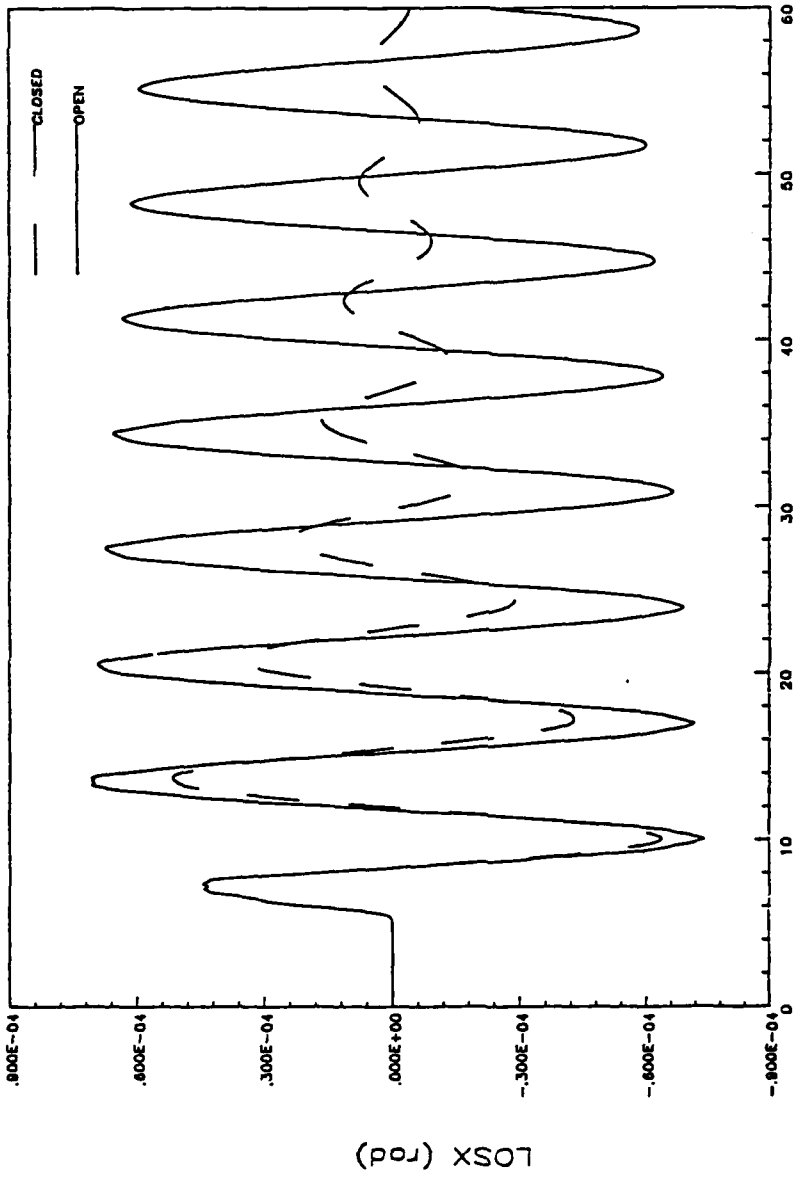

Figure 77. Open and Closed Loop X-Axis LOS Responses to Crew Motion Disturbance in Y (RTOP).

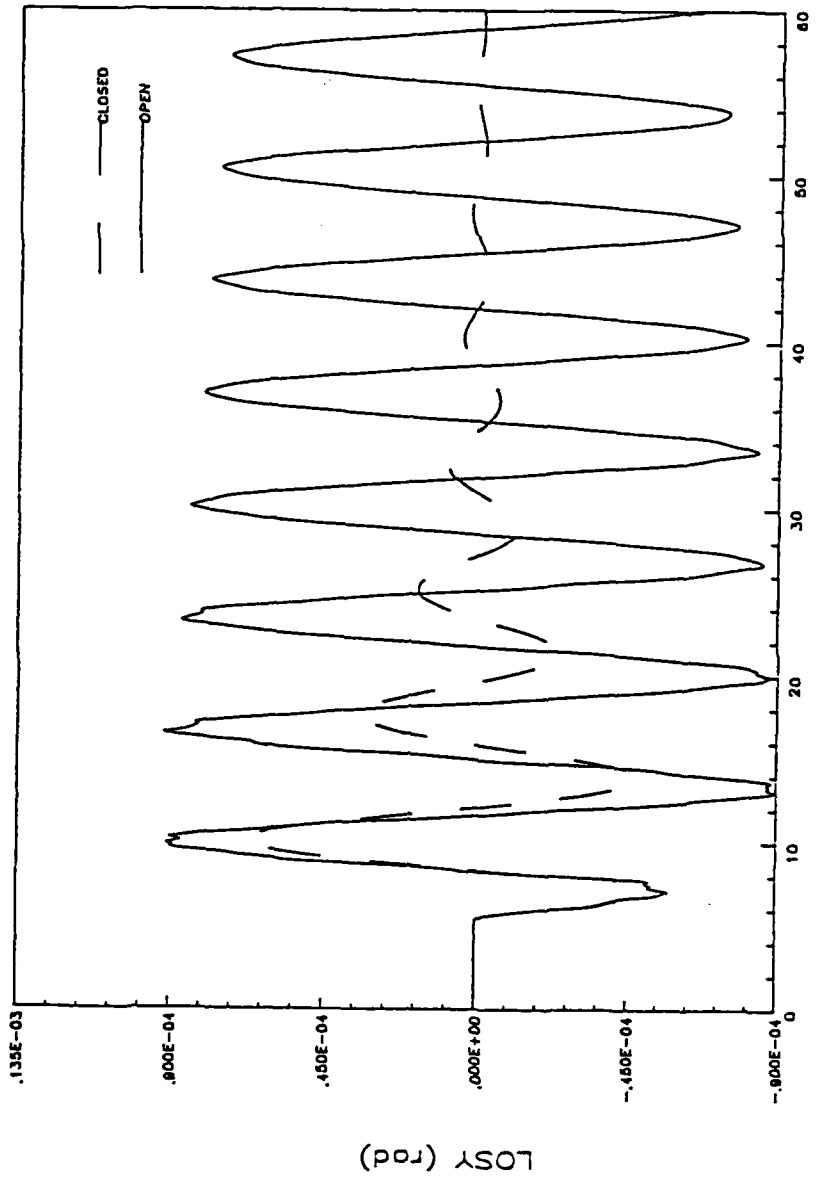

Figure 78. Open and Closed Loop Y-Axis LOS Responses to Crew Motion Disturbance in X (RTOP).

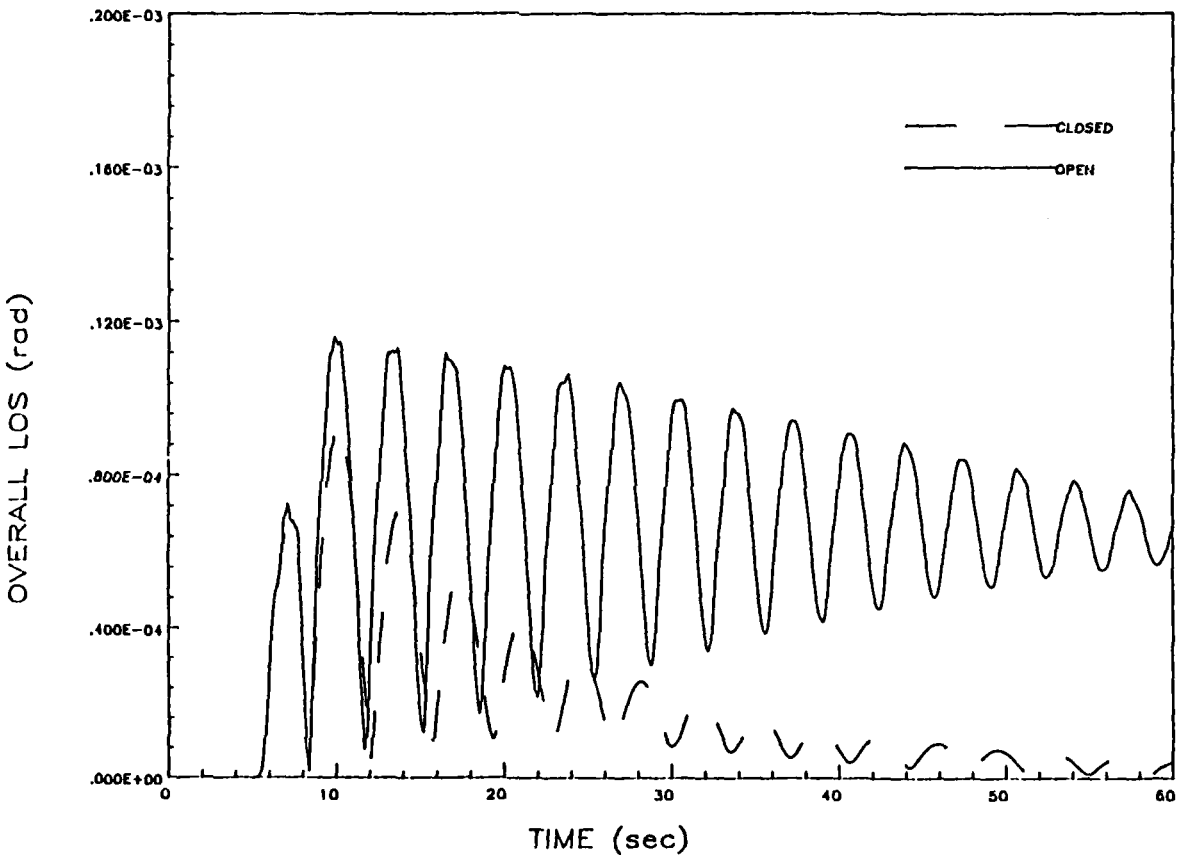

Figure 79. Open and Closed Loop Total Error Responses to Crew Motion Disturbance in Both X and Y (RTOP).

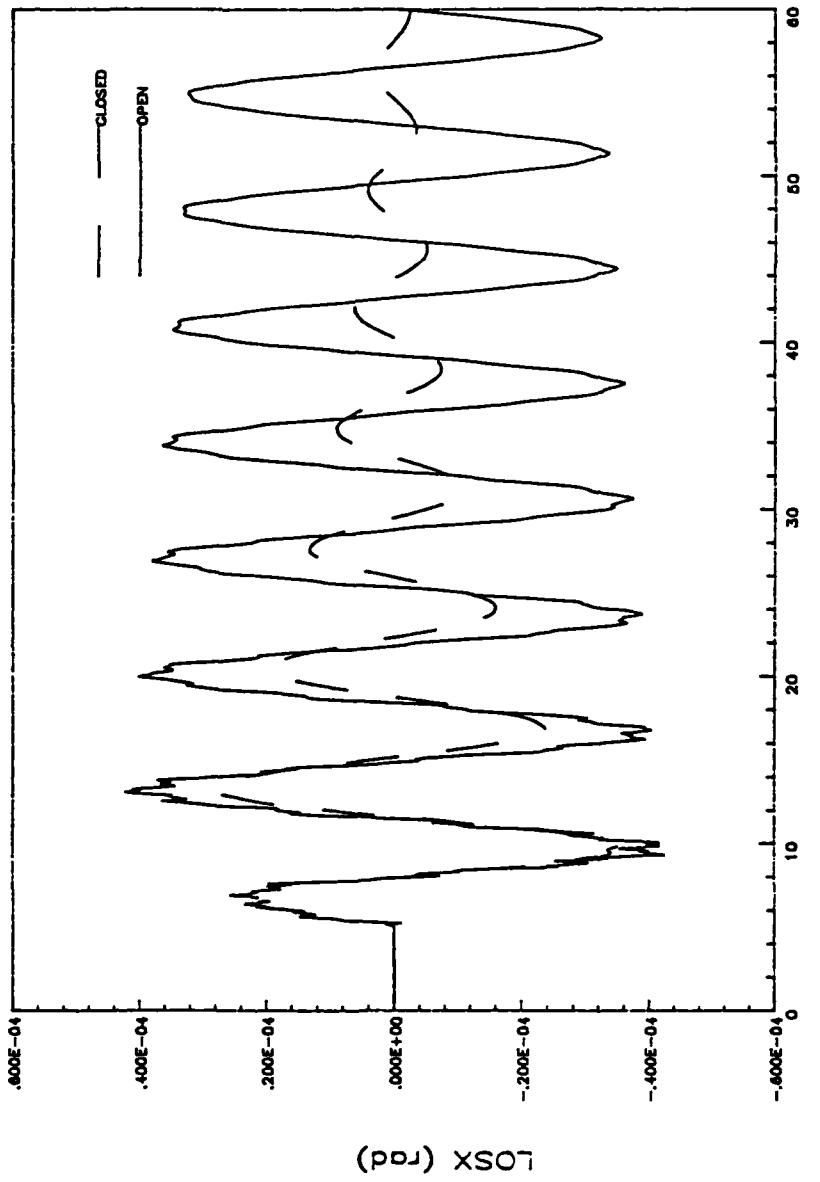

Figure 80. Open and Closed Loop X-Axis LOS Responses to RCS Disturbance in Y (RTOP).

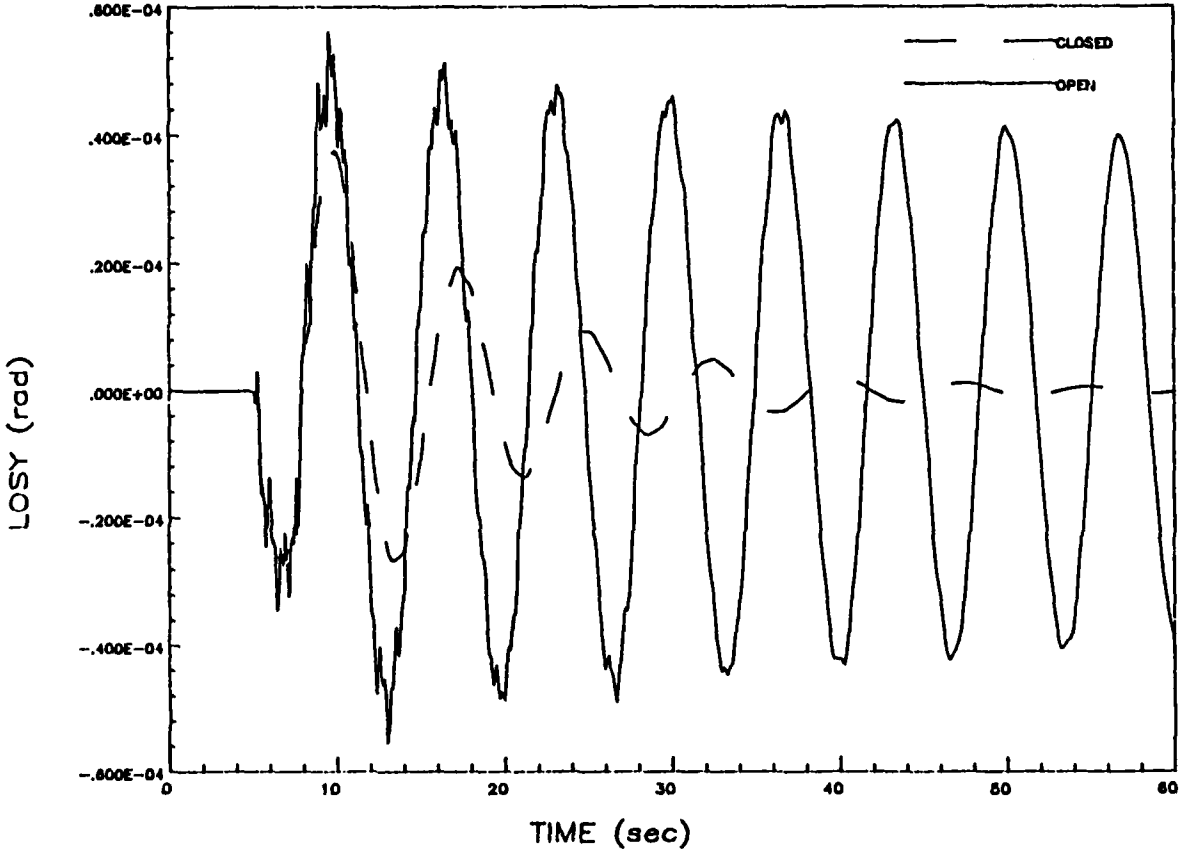

Figure 81. Open and Closed Loop Y-Axis LOS Responses to RCS Disturbance in X (RTOP).

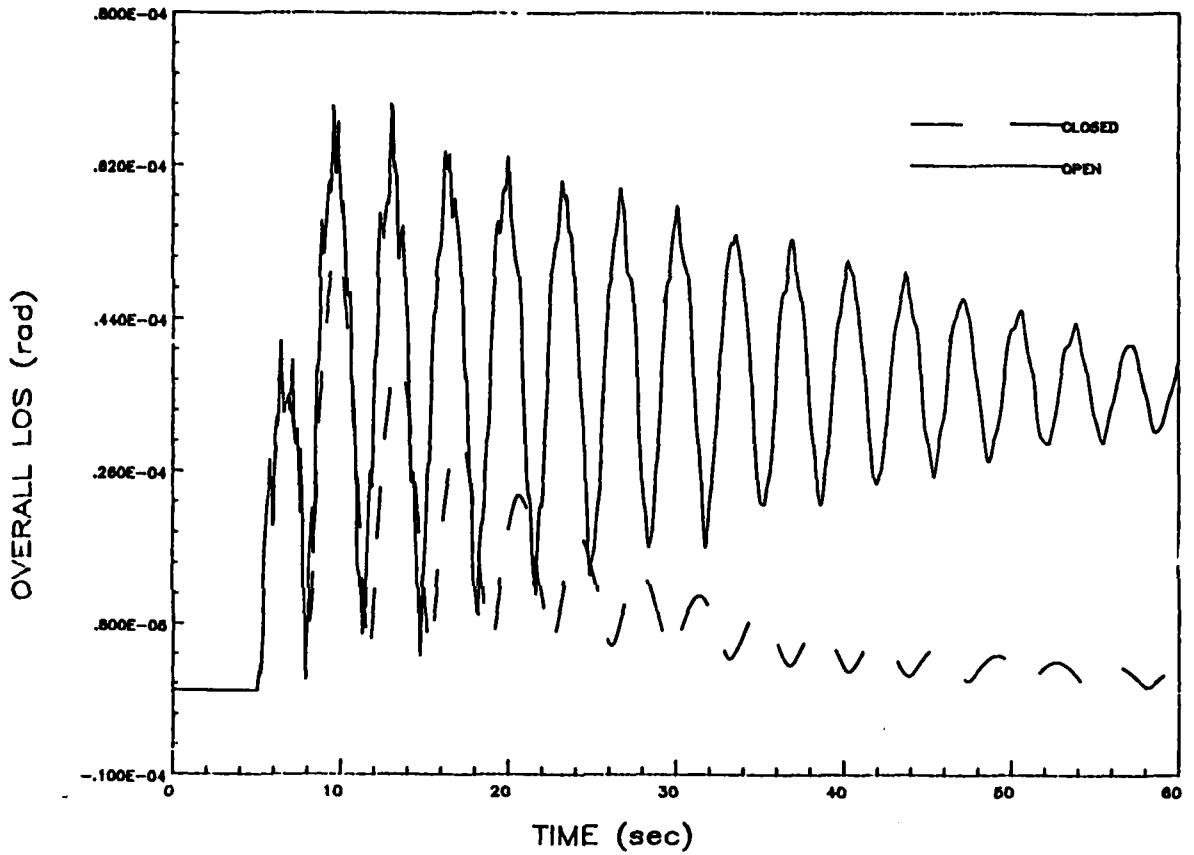

Figure 82. Open and Closed Loop Total Error Responses to RCS Disturbance in Both X and Y (RTOP).

RTOP System Conclusions. The S2D2 candidate, 1CAT, has been demonstrated through application to a coupled 3-axis system having 40 modes, 3 inputs, 5 measurements, and an 8 path control law. The system model also includes realistic sensor and actuator dynamics and the effects of sampling upon system stability.

The results are promising. The closed loop system was shown to be stable and provide some amount of disturbance rejection. Greater bandwidth and, hence, disturbance rejection than in the ASCOT-I system studies was not achievable, despite the greater complexity of the control system, because of the deleterious effects of the sensor and actuator dynamics. The system did, however, produce greater damping of the pendulum behavior than the ASCOT-I controller.

3. CONCLUSIONS

The Simplified Systematic Digital Design (S2D2) candidate, 1CAT (One Controller At a Time), has been shown to be a viable candidate for design of control systems for LSS. The design process has been demonstrated on a decoupled three-axis LSS pointing system model (ASCOT-I) and on a more complicated coupled three-axis system (RTOP) of a similar design having 40 modes in the design model. Reasonable sensor, actuator, and sample rate constraints were included, and the technique is equally useable with these constraints. 1CAT also meets the intrinsic quality requirements for S2D2 delineated in Section 2.1.1. In particular, the analysis and design are conducted in the digital domain and relative stability of the closed loop system can be ensured.

With respect to the non-uniform sampling rate prefilter studies, it is clear that more theoretical background must be developed in this area before implementable filtering techniques are possible. The fast uniform rate prefilter concept is, on the other hand, straightforward and presently implementable. The only outstanding drawback being the possibly limited number of applications where such a prefilter would be both functional and cost effective.

Two areas of suggested future effort stand out. First is the use of an automated, multi-variable, frequency domain tuning algorithm to optimize 1CAT controller designs to certain specifications, such as bandwidth and stability margins, in an iterative manner. Such an algorithm would allow more precise "tuning" of stable designs produced using 1CAT.

Additional effort should be placed in the non-uniform sampling rate filter area, also. This includes investigation of other schemes for choosing

the sampling rate at each sample period and the possibility of digital compensation design using the non-uniform sampling rate so that no prefilter would be necessary.

REFERENCES

[1] Mitchell, J. R., Worley, H. E., and Seltzer, S. M., "Digital Control System Design for a Precision Pointing System," American Astronautical Society Annual Rocky Mountain Guidance and Control Conference, Keystone, Colorado, February 5-9, 1983.

[2] Seltzer, S. M., et al, ACOSS SEVENTEEN (Active Control of Space Structures) Final Technical Report, RADC-TR-84-186, September, 1984.

[3] Kuo, Benjamin C., Digital Control Systems, Holt, Rinehart, and Winston, 1980.

[4] Brown, R. G., Introduction to Random Signal Analysis and Kalman Filtering, Wiley, 1983.

[5] Leneman, O. A. Z., "Random Sampling of Random Processes: Impulse Processes," Information and Control 9, 347-363, 1966.

[6] Renton, J. D., "The Beam-Like Behavior of Space Trusses," AIAA Journal, Vol 22, No. 2, February, 1984, pp. 273-280.

[7] Soucy, Y. and Vigneron, F. R., "Identification of Structural Properties of a Continuous Longeron Space Mast," Paper No. 84-0930, AIAA/ASME/ASCE/AHS 25th SDM Conference, Palm Springs, May, 1984, pp. 130-139.

DISTRIBUTION LIST

addresses	number of copies
Richard W. Carman RADC/OCSP	5
RADC/TSTD GRIFFISS AFB NY 13441	2
RADC/DAP GRIFFISS AFB NY 13441	2
ADMINISTRATOR DEF TECH INF CTR ATTN: DTIC-DDA CAMERON STA BG 5 ALEXANDRIA VA 22304-6145	12
Control Dynamics Company 555 Sparkman Drive, Suite 1414 Huntsville, Alabama 35805	5
Charles Stark Draper Lab Attn: Dr. Keto Soosaar 555 Technology Square M.S. -95 Cambridge, MA 02139	1
NASA Headquarters ATTN: Mr. J. B. Dahlgren Code RTH-6 Washington, DC 20546	1
Charles Stark Draper Lab Attn: Mr. R. Strunce 555 Technology Square M.S. -60 Cambridge, MA 02139	1

Charles Stark Draper Lab 1
Attn: Dr. Daniel R. Hegg
555 Technology Square
M.S. -60
Cambridge, MA 02139

ARPA/STO 1
Attn: Lt Col A. Herzberg
1400 Wilson Blvd
Arlington, VA 22209

ARPA/STO 1
Attn: Maj E. Dietz
1400 Wilson Blvd
Arlington, VA 22209

Riverside Research Institute 2
Attn. Mr. A. DeVilliers
1701 N. Ft. Myer Drive, Suite 711
Arlington, VA 22209

Riverside Research 1
Attn: HALO Library, Mr. Bob Passut
1701 N.Ft. Myer Drive
Arlington, VA 22209

Itek Corp 1
Optical Systems Division
10 Maguire Rd.
Lexington, MA 02173

Perkin Elmer Corp 1
Attn: Mr. H. Levenstein
Electro Optical Division
Main Avenue
Norwalk, CT 06856

Hughes Aircraft Company 1
Attn: Mr. George Speak
M.S. B_156
Culver City, CA 09230

Hughes Aircraft Company
Attn: Mr. Ken Beale
Centinela Teale Sts
Culver City, CA 90230 — 1

Air Force Flight Dynamics Lab
Attn: Dr. Lynn Rogers
Wright Patterson AFB, OH 45433 — 1

AFWL/FIBG
Attn: Mr. Jerome Pearson
Wright Patterson AFB, OH 45433 — 1

Air Force Wright Aero Lab. FIGC
Attn. Siva S. Banda
Wright Patterson AFB, OH 45433 — 1

Air Force Institute of Technology
Attn: Prof. R. Calico/ENY
Wright Patterson AFB, OH 45433 — 1

Aerospace Corp.
Attn: Dr. G.T. Tseng
2350 E. El Segundo Blvd
El Segundo, CA 90245 — 2

Aerospace Corp.
Attn: Mr. J. Mosich
2350 E. El Segundo Blvd
El Segundo, CA 90245 — 1

Aerospace Corp/Bldg 125/1054
Attn: Mr. Steve Burrin
Advanced Systems Tech Div.
2400 E El Segundo Blvd
El Segundo, CA 90245 — 1

SD/SD/YLVS 1
Attn: Mr. Lawrence Weeks
P.O. Box 92960
Worldway Postal Center
Los Angeles CA 90009

SD/YCD 1
Attn: YCPT/Capt Gajewski
P.O. Box 92960
Worldway Postal Center
Los Angelel, CA 90009

Grumman Aerospace Corp 1
Attn: Dr. A. Mendelson
South Oyster Bay Road
Bethpage, NY 11714

OUSDR&E/DS 1
Attn. Mr. A. Bertapelli
Room 3D136
Pentagon, Washington, DC 20301

Jet Propulsion Laboratory 2
Dr. S. Szermay
4800 Oak Grove Drive
Pasadena, CA 91103

MIT/Lincoln Laboratory 1
Attn: S. Wright
P.O. Box 73
Lexington, MA 02173

MIT/Lincoln Laboratory 1
Attn: Dr. D. Hyland
P.O. Box 73
Lexington, MA 02173

MIT/Lincoln Laboratory 1
Attn: Dr. N. Smith
P.O. Box 73
Lexington, MA 02173

Control Dynamics Co. 1
Attn: Dr. Sherman Seltzer
Suite 1414 Executive Plaza
555 Sparkman Drive
Huntsville, AL 35805

Lockheed Space Missile Corp. 5
Attn: A. A. Woods, Jr., 0/62-E6
P.O. Box 504
Sunnyvale, California 94088-3504

Lockheed Missiles Space Co. 1
Attn: Mr. Paul Williamson
3251 Hanover St.
Palo Alto, CA 94304

General Dynamics 1
Attn: Ray Halstenberg
Convair Division
5001 Keary Villa Rd
San Diego, CA 92123

STI 1
Attn: Mr. R.C. Stroud
20065 Stevens Creek Blvd.
Cupertiono, CA 95014

NASA Langley Research Ctr 2
Attn: Dr. Earle K. Huckins III
Dr. M. F. Card
Langley Station, Bldg 1293B, MS 230
Hampton, VA 23665

NASA Johnson Space Center 1
Attn: Robert Piland
Ms. EA
Houston, TX 77058

McDonald Douglas Corp 1
Attn: Mr. Read Johnson
Douglas Missile Space Systems Div
5301 Bulsa Ave
Huntington Beach, CA 92607

Integrated Systems Inc. 2
Attn: Dr. N. K. Gupta and M. G. Lyons
151 University Avenue, Suite 400
Palo Alto, California 94301

Boeing Aerospace Company 1
Attn: Mr. Leo Cline
P. O. Box 3999
Seattle, WA 98124
MS 8 W-23

TRW Defense Space Sys Group Inc. 1
Attn: Ralph Iwens
Bldg 82/2054
One Space Park
Redondo Beach, CA 90278

TRW 1
Attn: Mr. Len Pincus
Bldg R-5, Room 2031
Redondo Beach, CA 90278

Department of the NAVY 1
Attn: Dr. K. T. Alfriend
Naval Research Laboratory
Code 7920
Washington, DC 20375

Airesearch Manuf. Co. of Calif. 1
Attn: Mr. Oscar Buchmann
2525 West 190th St.
Torrance, CA 90509

Analytic Decisions, Inc. 1
Attn: Mr. Gary Glaser
1401 Wilson Blv.
Arlington, VA 22209

Ford Aerospace & Communications Corp. 1
Drs. I. P. Leliakov and P. Barba, MS/G80
3939 Fabian way
Palo Alto, California 94304

Center for Analysis 1
Mr. James Justice
[illegible] Corporate Plaza
Newport Beach, CA 92660

W. J. Schafer Associates 1
Dr. R. Kappesser
Suite 800
1901 Fort Meyer Drive
Arlington, VA 22209

General Research Corp 1
Attn: Mr. Thomas Zakrzewski
7655 Old Springhouse Road
McLean, VA 22101

Air Force Weapons Laboratory 2
Attn: Lt Col D. Washburn
ARAA
Kirtland AFB, NM 87117

Karman Sciences Corp. 1
Attn: Dr. Walter E. Ware
1500 Garden of the Gods Road
P.O. Box 7463
Colorado Springs, CO 80933

MRJ, Inc. 1
10400 Eaton Place
Suite 300
Fairfax, VA 22030

Photon Research Associates 1
Attn: mr. Jim Myer
P.O. Box 1318
La Jolla, CA 92038

Rockwell International 1
Attn: Russell Loftman (Space Systems Group)
(Mail Code - SL56)
12214 Lakewood Blvd.
Downey, CA 90241

Science Applications, Inc. 1
Attn: Mr. Richard Ryan
3 Preston Court
Bedford, MA 01730

U.S. Army Missile Command 1
Attn: DRSMI-RAS/Mr Fred Haak
Redstone Arsenal, AL

Naval Electronic Systems Command 1
Attn: Mr. Charles Good
PME_106-4
National Center I
Washington, DC 20360

Lockheed Palo Alto Research Laboratory 2
Attn: Dr. J. N. Aubrun, 0/52-56
3251 Hanover Street
Palo Alto, California 94304-1187

U S Army/DARCOM 1
Attn: Mr. Bernie Chasnov
AMC Bldg
5001 Eisenhower Ave
Alexandria, VA 22333

Defense Documentation Center 1
Cameron Station
Alexandria, VA 22314

Honeywell Inc. 2
Attn: Dr. Thomas B. Cunningham
Attn: Dr. Michael F. Barrett
2600 Ridgway Parkway MN 17-2375
Minneapolis, MN 55413

NASA Marshal Space Flight Center 2
Attn. Dr. J. C. Blair, ED01
Henry B. Waites
Marshal Space Flight Center, AL 35812
1

TRW 1
Attn: Robert Benhabib
Bldg 82/2024
One Space Park
Redondo Beach, CA 90278

NASA Langley Research Center 1
Attn: Dr. L. Pinson
MS - 230
Hampton, VA 23665

H. R. Textron
Attn. Mr. Richard Quartararo
2485 McCabe Way
Irvine, CA 92714 1

Naval Research Lab
Attn: W. Bennett
Mail Code: 7926
Washington, DC 20375 1

TOTAL COPIES REQUIRED 102

Engineer/LCN Signature Richard M. Carreau (Jul 85

MISSION
of
Rome Air Development Center

RADC plans and executes research, development, test and selected acquisition programs in support of Command, Control Communications and Intelligence (C^3I) activities. Technical and engineering support within areas of technical competence is provided to ESD Program Offices (POs) and other ESD elements. The principal technical mission areas are communications, electromagnetic guidance and control, surveillance of ground and aerospace objects, intelligence data collection and handling, information system technology, ionospheric propagation, solid state sciences, microwave physics and electronic reliability, maintainability and compatibility.